Thermal and residual stress modeling of functionally graded deposits using the PTAAM

by

Geoffrey Bonias

A thesis submitted in partial fulfillment of the requirements for the degree of

Master of Science

in

Materials Engineering

Department of Chemical and Materials Engineering
University of Alberta

Abstract

High maintenance costs due to significant abrasive wear of components is experienced in the

energy and mining sectors despite the current use of tough and hard coatings. During the coating

process significant detrimental residual stresses may build up and result in premature failure of a

component. These stresses can be reduced by adopting functionally graded structures of the

composite. The main goal of the present study is to design an ideal additively manufactured path

and print functionally graded geometries using plasma transferred arc (PTA) with WC-Ni alloy

composite. To develop a comprehensive analysis of the functionally graded deposit, the thermal

history of the WC and Ni alloy powders must first be simulated as they travel through the plasma

and deposit on the substrate. Predictions of particle trajectories in the plasma are compared to

experimentally tracked powder particles to validate the model. The power transferred from the

arc to the anode is divided into an electronic, a convective and a radiative contribution and is

then estimated. The dependency of the thermal history of the WC and Ni powder particles and of

the heat input from the arc to the anode on the PTA operating parameters is discussed

quantitatively. Inferences from this preliminary work are then used as input data to simulate the

additive manufacturing of functionally graded materials at the macro scale level. The thermal

history followed by the thermal stress history of the process is predicted, and finally the residual

stress distribution is obtained for a wall-shaped printed part. Simulations are performed on

Abaqus for different material gradients under the same operating conditions. The residual stress

profiles of each material gradient are compared to each other and to a wall without gradient.

Conclusions are drawn as to the material gradation that is most susceptible to enhance the

coating wear resistance from a residual stress perspective. Future work could focus on validating

the thermal and residual stress model and establishing the wear characteristics of the graded deposits. Using the model, strategies could be established to optimize the temperature history of the graded coating during its printing to further reduce tensile residual stresses and reduce WC settling in the liquid bead to improve homogeneity.

Preface

This thesis is an original work by Geoffrey Bonias and is the result of a co-supervision collaboration between the University of Alberta and Mines Nancy in France.

No part of this thesis has been previously published, but a version of Chapter 2, a version of Chapter 3 and a version of Chapter 4 respectively are intended to be submitted for publication. The models and simulations presented in these three chapters were all designed by myself, as well as the criterion chosen to complete the general objective of this thesis (design of an ideal material gradient in a Ni-WC wear resistant coating additively manufactured with the PTA). I was responsible for the data collection and analysis and manuscript composition. Dr. Hani Henein provided the objective, supervised the project, contributed to the manuscript edits and structure, and Dr. Tonya B. Wolfe co-supervised the project.

Acknowledgements

Table of Contents

List of Tables

List of Figures

List of Symbols

Greek letters

- α: Thermal diffusivity (m^2/s)
- γ: Specific heat ratio
- ε: Net Emission Coefficient (NEC) ($W.m^{-3}.sr^{-1}$)
- η: Cinematic viscosity ($m^2.s^{-1}$)
- θ: Angle coordinate or solid angle (° or sr)
- μ_0: Magnetic Permeability of Void ($T.m.A^{-1}$)
- μ: Dynamic viscosity (Pa.s)
- ν: Mean molecular speed ($m.s^{-1}$)
- ρ: Density ($kg.m^{-3}$)
- σ: Electrical conductivity ($S.m^{-1}$)
- ϕ: Electron thermal diffusion coefficient
- Φ: Work function (eV)

Latin letters

- a: thermal accommodation factor
- A: Richardson constant ($A.cm^{-2}.K^{-2}$)
- B: Magnetic Field
- c_p: Specific heat capacity at constant pressure ($J.K^{-1}.kg^{-1}$)
- d: Size (diameter) (mm)
- e: Electron charge (eV)
- g: Gravity ($m.s^{-2}$)
- h: Enthalpy ($J.kg^{-1}$) (always with subscript)
- h: Heat transfer coefficient ($W.m^{-2}.K^{-1}$) (no subscript)
- I: Current (A)
- j: Current density ($A.m^{-2}$)
- J: Current density ($A.m^{-2}$)
- k: Conductivity

- k_B: Boltzmann constant (eV.K^{-1})
- L: Latent heat (J.kg^{-1})
- m: Mass (kg)
- M: Molecular mass (kg.mol^{-1})
- $\dot{m}$: Mass flow rate (kg.s^{-1})
- n: Layer number
- p: Pressure (Pa)
- P: Pressure (Pa)
- q: Heat flux (W.m^{-2})
- Q: Heating power (W)
- r: Radius (mm) (always with subscript)
- r: Radius coordinate (mm) (no subscript)
- R: Constant of perfect gases (J.K^{-1}.mol^{-1})
- S: Area (m^2)
- T: Time (s)
- T: Temperature (K)
- v: Velocity (m.s^{-1})
- V: Flowing Speed (of plasma gas) (m.s^{-1})
- $\dot{V}$: Volume flow rate (of plasma gas) (m^3.s^{-1})
- z: Height coordinate (mm)

Two Latin letters

- Bi: Biot number
- Cd: Drag coefficient
- Kn: Knusselt number
- Nu: Nusselt number
- Pr: Prandtl number
- Re: Reynolds number

Vectors

- $\vec{B}$:   Magnetic Field (generated by $\vec{j}$)

- $\overline{div}$:   Divergence

- $\vec{e}$:   Unit vector

- $\overline{f_{vol}}$:   Volume forces

- $\vec{j}$:   Current density vector in the plasma (LTE zone)

- $\overline{v}$:   Plasma velocity

- $\overline{\nabla}$:   Gradient

- $\bar{\bar{\sigma}}$:   Constraint tensor

Subscripts

- θ: in tangential direction (cylindrical coordinates)

- a: relative to the plasma arc (LTE zone, free flow region)

- av: plasma property taken at boundary layer integrally averaged temperature

- c: relative to the plasma arc just below the cathode tip

- cv: convective contribution

- d: relative to viscous drag from plasma

- e: electronic contribution or relative to the electron

- eff: effective value

- ev: evaporation effect

- g: plasma property taken at plasma gas temperature

- Kn: Knusselt effect

- m: plasma property taken at boundary layer median temperature

- p: relative to the powder particle

- r: in radial direction (cylindrical coordinates)

- R: radiative contribution

- s: plasma property taken at particle or wall/substrate surface temperature

- T: property taken at temperature T

- vp: varying properties effect

- z: in axial direction (cylindrical coordinates)

- 0: at room temperature

Glossary of Terms

- AM: Additive Manufacturing
- CTE: Coefficient of Thermal Expansion
- FGM: Functionally Graded Material(s)
- GTAW: Gas Tungsten Arc Welding
- HAZ: Heat Affected Zone
- HI: Heat Input
- MMC: Metal Matrix Composite
- NEC: Net Emission Coefficient
- PTA: Plasma Transferred Arc
- PTA-AM: Plasma Transferred Arc Additive Manufacturing
- WC: Tungsten Carbide

Chapter 1 : Introduction

1.1 Background and Context

Oil sands mining operations in Alberta generate high maintenance costs due to wear and abrasion. For example, the teeth in shovel buckets (Figure 1-1) or crusher rolls are critical components in mining processing whose premature failure would require unplanned maintenance, thus interrupting production and diminishing the daily productivity. The costs associated can go up to $3M-$6M a day when a regular 100 000-barrel oil sands train is interrupted (Wolfe, 2010).
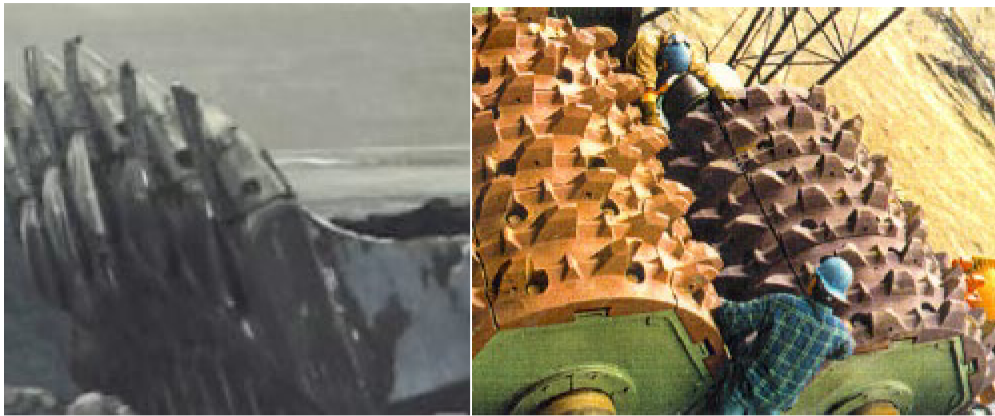
Figure 1-1: left - Shovel bucket for oil sands and right - Crusher rolls (Credit: (Wolfe, 2010))

In order to enhance the life of critical equipment that experience a high degree of wear, wear resistant materials in the form of coatings or overlays can be applied to the surface of the bulk component. In the case of the most critical applications, a WC reinforced NiCrBSi or NiBSi metal matrix composite (MMC) is deposited onto the surface using the plasma transferred arc (PTA) welding process. The high hardness of the tungsten carbide particles combined with the high toughness of the nickel alloy matrix significantly helps to reduce abrasion rate. An optical image of the microstructure of the composite with the WC in the nickel-based matrix is shown in Figure 1-2 (Credit: (Wolfe, 2010)).

Optimization of the coating composition and the deposition process resulted in a significant enhancement of the in-service lifespan of critical mining components (Wolfe, 2010).
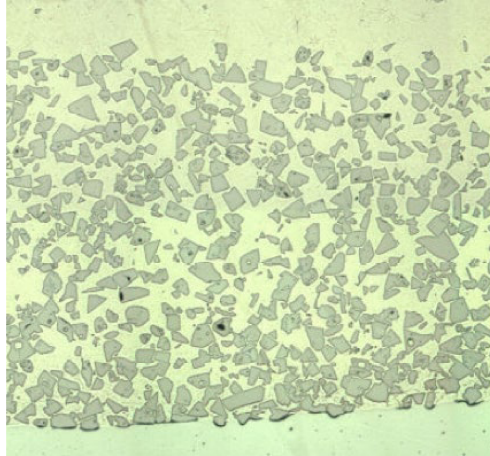
Figure 1-2: Optical image showing a distribution of WC particles in the NiCrBSi matrix

Homogeneity of the WC distribution in the matrix was found to be a critical factor for the final coating's wear resistance. In particular, the WC settling that occurs before the nickel-based matrix solidifies can result in the settling of WC resulting in a top surface void of WC (see Figure 1-2 (Wolfe, 2010)) which is detrimental to its wear resistance. Developing an ideal operating window with PTA allowed for good distribution of the carbides as well as ensuring a metallurgical bond with the substrate was obtained (Wolfe, 2010).

Nevertheless, the high residual stresses generated during this deposition remains an important issue. In particular, high tensile stresses may develop at the coating surface and decrease its ability to withstand loads and wear notably because the WC can be pulled out more easily of the scratched matrix (Xu & Todd, 2015) (Lu, et al., 2003).

The smooth transition in the thermomechanical properties also theoretically decreases the residual stresses at the interface between the coating and the substrate, thus reducing the risk of delamination (Bao & Cai, 1997). Residual stresses significantly affect the part's mechanical and wear resistance and can lead to premature failure, which is why they must be mitigated.

Understanding the thermal processing that yields the formation of residual stresses is critical when considering additive manufacturing of functionally graded materials (FGM). Indeed, the gradient selection will directly impact the residual stress distribution in the coating and therefore its mechanical resistance when subjected to wear. In this process, the composition of the build is gradually changing as the build progresses between two distinct chemistries. The selection of the chemistries, as well as the degree of gradation will lead to an optimized wear resistance

thanks to residual stress mitigation (Xu & Todd, 2015) (Bao & Cai, 1997) (Bouchafa, et al., 2010) (Ravichandran, 1995) (M.H. Yu, 2010).

1.2 Problem Statement

The purpose of this research is to find a gradation of the coating material's composition from base alloy composition to the wear material composition that will maximize wear resistance and minimize thermal stresses. The composition of the surface in contact with the substrate (base alloy) is that of the nickel alloy alone while the deposited wear material is composed of the nickel alloy with 60wt% WC. Adding such a material gradation from substrate to wear surface should help enhance the wear resistance of critical components in oil sands mining operations, when manufactured using PTA-AM. To ensure an improved performance of the coating, the residual stresses need to be minimized.

Plasma Transferred Arc Additive Manufacturing (PTA-AM) is a process by which the component is manufactured by the deposition of powders layer by layer using the plasma transferred arc welding process. To create a functional gradient, each layer can be assigned a specific composition intermediate between the bulk material and the wear material, and the deposition parameters adapted for each layer. Figure 1-3 presents a schematic of a gradation profile in an FGM. The thickness and profile of the functionally graded zone is specific for each application.
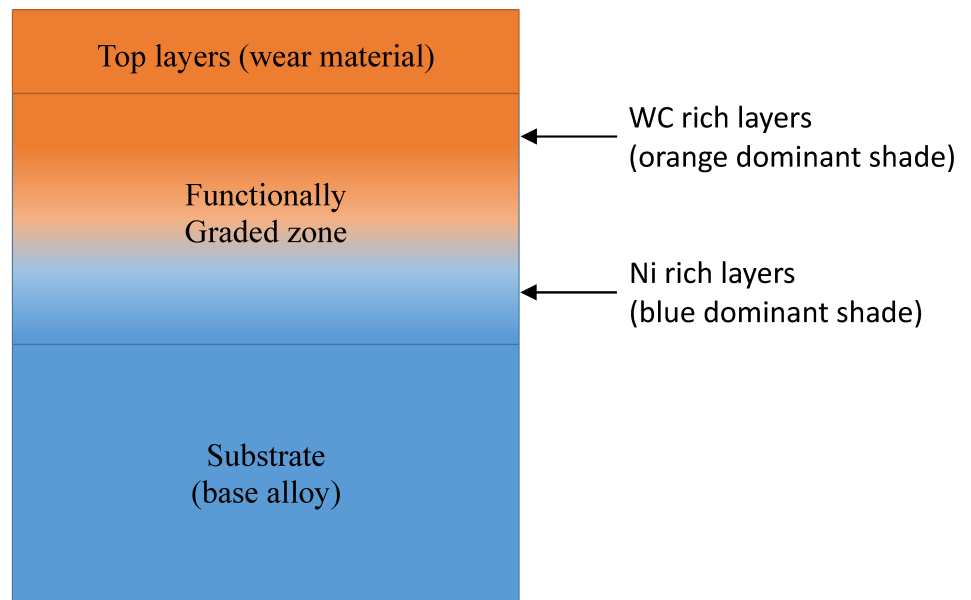
Figure 1-3: Representation of a graded material profile

1.3 Literature review

This section discusses the characteristics of Plasma Transferred Arc Welding (PTAW), challenges that may be encountered when using this process as an Additive Manufacturing tool, the notions of Functionally Graded Materials and how residual stresses can be predicted and alleviated using this concept, and how the reduction of residual stresses are expected to improve the Ni-WC graded coating wear resistance. An insight is given about previous works that characterized the plasma arc and its interactions with the injected powder particles during the PTA-AM deposition process.

1.3.1   Plasma Transferred Arc Welding

Plasma Transferred Arc Welding (PTAW) is a welding process in which a plasma arc (main arc) is transferred between the workpiece and the electrode. In order to establish the main arc, a non-transferred arc (pilot arc) must first be initiated between the electrode and the copper nozzle (Wolfe, 2010) (Zhang, et al., 2016). The plasma gas flowing along the electrode (Figure 1-4) is ionized and provides a path for the electrons to travel (Deuis, et al., 1998).

This welding process is similar to Gas Tungsten Arc Welding (GTAW) in that the tungsten electrode is non-consumable and usually operated with negative polarity (cathode) but may also be operated in negative or variable polarity (Aithal, et al., 1988). The tip of the electrode, however, remains inside a water/glycol-cooled copper nozzle which constricts the arc to increase the arc energy density (Wolfe, 2010) (Rojas, et al., 2018) (Tabernero, et al., 2018) (Figure 1-4). Without the nozzle's action at the bottom of the electrode tip, the arc shape would be closer to a bell shape like in GTAW. The consumable is a powder conveyed through the torch by means of a carrier gas and injected inside the plasma arc (Deuis, et al., 1998) (Figure 1-4). The nozzle also transports a shielding gas around the arc to avoid oxidation and cools the weld (Wolfe, 2010) (Deuis, et al., 1998).

 The operating parameters involved in PTAW are arc current and voltage, powder flow rate, torch travel speed, plasma gas flow rate, shielding gas flow rate and carrier gas flow rate. The voltage is dependent on the distance between the nozzle and the substrate (Wolfe, 2010) (Li, et al., 2013).
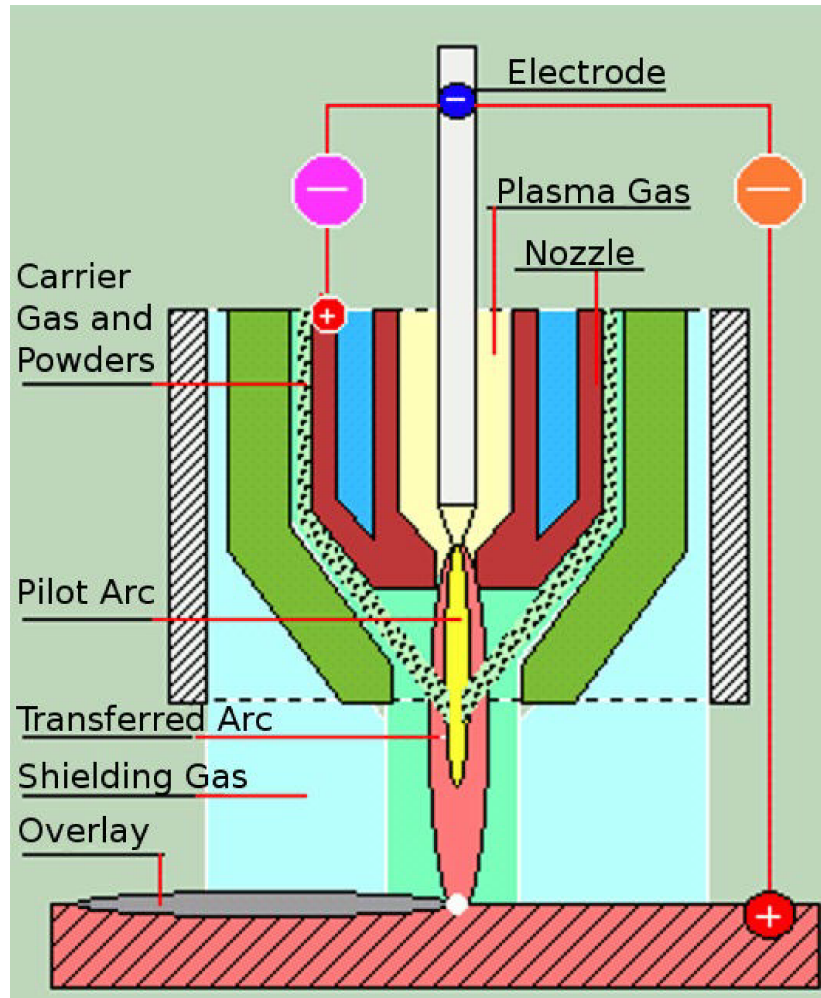
Figure 1-4: Schematic of Plasma Transferred Arc Welding (Wolfe, 2010)

In PTA-AM, a table and/or torch move to deposit the powder layer by layer thereby generating a 3D print of the desire part (Rojas, et al., 2018). Similar to PTA, the heat input will be controlled by the torch welding speed, voltage and current (Li, et al., 2013) (Zhang, et al., 2016), however when thicker parts are printed requiring the juxtaposition of powders inside the same layer the notion of energy density must be used instead of heat input (Sames, et al., 2016). The "energy per length" in heat input is replaced by an "energy per volume" or energy density (Oliveira, et al., 2020):

$$ED = \frac{Q}{vh\Delta z} \tag{1-1}$$

where Q is the power absorbed, v the travel speed, h the hatch spacing and Δz the layer height.

The hatch spacing is the lateral distance between the axis of each pass (Figure 1-5).
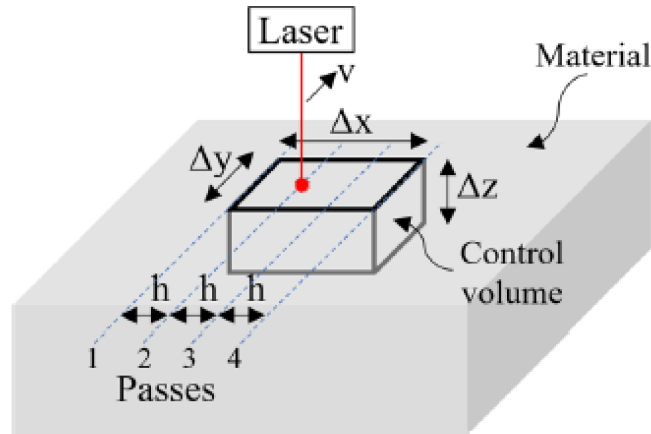
Figure 1-5: Schematic of the hatch spacing (h) and the control volume for defining energy density in laser or arc AM (Oliveira, et al., 2020)

In PTA-AM, the powder is transported through ports in a coaxial nozzle using a carrier gas before being melted in the arc (Rojas, et al., 2018). The carrier gas flow can be adapted for generating the desired powder flow (Delluc, et al., 2005). An increase in plasma gas flow will impact the heat input and plasma arc radius (Zhang, et al., 2016). An increase in shielding gas flow increases the cooling rate of the weld pool while providing better protection against oxidation (Wolfe, 2010) (Moghazi, et al., 2020).

1.3.2 PTA operating parameters impact on the alloy wear resistance

The material selected for this work is a mixture of WC and NiBSi powders, also known as a Metal Matrix Composite (MMC). The tungsten carbide plays the main role for the abrasion resistance because of their high hardness and the Ni-based matrix provides toughness to the MMC coating as WC is brittle. A higher content of WC increases the abrasion resistance (Badisch & Kirchgaßner, 2008). The WC content used in this work is 60wt%.

The operating parameters of the PTA also have a critical impact on the coating's wear resistance. For wear resistance improvement, the hardness of the nickel matrix can also be enhanced through control of the heat input due to changes in the microstructure and microchemistry (Sudha, et al., 2008) (F.Fernandes, et al., 2011). However, the harder WC play the essential role in providing the coating's high resistance to abrasion. Therefore, in order to preserve the WC, an excessive heat input leading to carbide dissolution and degradation must be avoided (Badisch &

6

Kirchgaßner, 2008) (Katsich & Badisch, 2011). Furthermore, the carbide dissolution can lead to the precipitation of brittle secondary phases that are detrimental to wear resistance (Liyanage, et al., 2012). However, secondary phases formed at the interface between the WC and the matrix may increase their bonding with the matrix (P. Wu, 2003) and increase the MMC micro-hardness (Badisch & Kirchgaßner, 2008) (Gowtham, et al., 2020). Their impact on fracture toughness must also be considered (Wolfe, 2010).

Of particular importance is the homogeneity of the distribution of the WC inside the Ni-based matrix (Wolfe, 2010) (Badisch & Kirchgaßner, 2008). Due to the density difference of the two particles, the denser particles will settle at the bottom of the deposit during solidification, leaving a deficit of WC at the surface. The lack of WC will result in a higher degree of wear (Wolfe, 2010) (Badisch & Kirchgaßner, 2008) (P. Wu, 2003). Reducing the heat input will shorten the solidification time of the deposit so that the carbide will have a lower residence time exposed to the liquid matrix. This lower time will result in less settling time before the matrix fully solidifies, but will also reduce kinetics of reaction between the carbide and liquid matrix (Wolfe, 2010) (P. Wu, 2003) (Gowtham, et al., 2020).

To avoid reactions with air, argon is used for the plasma, carrier and shielding gases when welding the MMC (Wolfe, 2010). A mix of 95%Ar/5%H2 is typically used when welding stainless steel in AM (Moghazi, et al., 2020). Indeed, when the torch is welding on top of a previously deposited bead, the hydrogen reduces the oxides layers formed on the latter after torch had passed (since the shielding gas was not protecting the bead anymore).

Two transitions can be considered in this work: from the base material (stainless steel) to the MMC, or from the nickel matrix alone (without WC) to the MMC with an increasing WC content layer by layer. The base material used in this work is the 17-4PH (Precipitation Hardened) martensitic stainless steel (also referred to as Grade 630), which is commonly used in the oil sands industry is a highly weldable steel with excellent corrosion resistance and good strength (Moghazi, et al., 2020). The copper content (4 wt%) precipitates during a heat treatment to increase the hardness, while the chromium (17 wt%) delivers the corrosion resistance (Moghazi, et al., 2020). In this work, we will first consider the transition between NiBSi to NiBSi-WC.

1.3.3 Sources of defects in welding and AM

In this section, sources of defects in welding and additive manufacturing and the forces acting on the weld pool before its solidification will be presented. Insight is given on how to control these forces and defects. The operating parameters selected for each layer in the PTA-AM of FGM process are critical to achieve a successful build because of the reasons cited in the previous and present section.

The heat input (HI) is a major factor of quality as it controls the maximum temperature reached and cooling rate in the weld pool and the heat affected zone (HAZ), and therefore the final microstructure. High cooling rates generate finer microstructure and usually improve the strength of metallic alloys, while slow cooling rates result in coarse grains. During printing, overheating (high HI) will provoke slower cooling rates, but insufficient HI will result in lack of fusion and defects (Moghazi, et al., 2020). HI management is also critical to control defect formation (Moghazi, et al., 2020). During the printing of a NiBSi matrix reinforced with 60%wt WC, it was observed that porosity increased in the last layers (Rojas, et al., 2018). This observation was attributed to heat build-up.

The weld pool flow impacts heat transfer, geometry of the beads, and may also be a source of defects. The driving forces for the weld pool flow are:

- buoyancy force, as the density is a function of temperature which is not homogeneous within the weld pool,
- Lorentz force, which is due to the electric current interacting with its induced magnetic field,
- the arc shear force, as the arc flows outwards and induces friction, and
- Marangoni convection, which occurs due to surface tension gradients occurring in the pool due to the presence of temperature gradients.

Among these forces, Marangoni convection is often dominant in welding and AM (Song, et al., 2020) (Leung, et al., 2019). As a consequence, the shape of the weld pool and that of the resulting solidified bead is mostly controlled by the Marangoni convection. The mechanism of this convection and its influence on the weld pool shape is described in the next paragraph. The

shape of the weld pool impacts the solidification time as a shallower shape cools down faster by conduction (higher area crossed by a high heat flux over volume ratio).

The temperature of the weld pool is lower at the edges which is in contact with the cooling gas. A temperature gradient in the weld pool induces a surface tension gradient as the local surface tension varies with temperature. Whether an increase in the temperature induces an increase or a decrease in the surface tension depends on the weld pool chemical composition. According to the surface tension temperature gradient sign (positive if surface tension increases with temperature), an inward or outward convection will be created, with more or less shallow pools. Therefore, it will strongly impact the final shape of the beads. Fe-Ni alloys have a negative temperature gradient of surface tension (Leung, et al., 2019), therefore higher surface tensions around the cooler edges, which lead to a convection towards the edges (centrifugal) and consequently a shallower bead.

Surface tension in the melt pool may also result in the "balling" phenomena: the weld separates into small discrete spheres. This occurs when the length of the melt pool (in welding direction) is greater than twice its diameter thus forming a sphere to reduce the surface free energy (surface tension is again the driving force) (Sames, et al., 2016). Melt pools with this shape appear with high travel (scanning) speeds and powers (Sames, et al., 2016).

In an FGM, the chemical composition of each layer changes with each subsequent layer deposited. As such, varying bead geometries can be expected in terms of height and width.

The difference in each layer's surface tension (and viscosity) variation with temperature also impacts the solidification time of their respective melt pool. Indeed, the amount of convection inside the melt pool depending on the Marangoni forces and the liquid's viscosity changes how fast the heat is conducted from inside the melt pool to outside the melt pool and therefore has a repercussion on the solidification time (Song, et al., 2020).

The formation of defects such as pores, oxides, and cracks is another important issue as they are greatly detrimental to mechanical properties. In AM, lack of fusion, micro-cracks or porosity will significantly decrease the fatigue resistance of the built part. Pores may form due to the lack of fusion (Moghazi, et al., 2020) (Rojas, et al., 2018) (Sames, et al., 2016) and therefore insufficient heat input, but they can also be due to an initial porosity in the commercial powders used

(Moghazi, et al., 2020) (Rojas, et al., 2018). Pores can be a nucleation point for microcracks due to local stress concentration (Sames, et al., 2016).

Oxides can be generated at the surface of stainless-steel welds. Although the formation of an oxide layer is good for corrosion resistance, they are detrimental when formed between the layers as they lead to anisotropic properties and poor adhesion (Moghazi, et al., 2020) (Sames, et al., 2016). The oxygen content may alter the sign of the surface tension temperature gradient and reverse the Marangoni convection in the weld pool (centripetal), trapping the gas under the weld pool surface and ultimately leading to gas pores (Leung, et al., 2019). Oxides can also be a nucleation site for pores, and lead to more spatter (Leung, et al., 2019). Hydrogen added to argon (95%Ar5%H2) can be used to tackle this problem since hydrogen is a reducing agent. As the torch passes over the last layer to print a new one on top of it, the hydrogen in the plasma & shielding gas will eliminate the oxide layer from forming (Moghazi, et al., 2020).

In the case of PTA-AM of FGM with 17-4PH and Ni-based MMC, the desirable centrifugal Marangoni convection is expected since Fe-Ni alloys have a negative temperature gradient of surface tension (the flow is from regions with lower surface tension to regions with higher surface tensions, so here towards colder temperatures at the edges). However, if gas pores are formed, the possibility that the melt pool convection is in fact centripetal due to a positive temperature gradient of surface tension should be considered, as this gradient is highly dependent on the exact alloy composition.

Finally, microscopic cracks occur when the local Ultimate Tensile Stress (UTS) of the material is exceeded (due to thermal stresses). Several types of microscopic cracks are distinguished. Hot cracking is due to the liquefaction of a low temperature eutectic near grain boundaries. Hot cracking can be observed in Ni-based superalloys and austenitic stainless steels and can be controlled through Heat Input (HI) selection (usually HI diminution) (Oliveira, et al., 2020). Cold cracking happens after full solidification due to residual stresses, when hard and brittle phases like martensite form due to high cooling rates. If hydrogen has diffused in the weld/HAZ it creates an additional stress and cold cracking is more likely to occur. High HIs tend to increase

residual stresses due to higher thermal gradients, which in turn increase cracking susceptibility (Sames, et al., 2016).

Macroscopic cracks can be induced by the residual stresses of the printing process and can be particularly high near the substrate-deposit interface (Sames, et al., 2016) to the point that debonding of the coating can occur (or layer delamination) (Oliveira, et al., 2020). Delamination also depends on the substrate/coating bonding (or layer/layer), therefore incomplete melting can also lead to delamination (Oliveira, et al., 2020).

1.3.4   Approaches to FGM design

FGMs are designed by choosing an optimum compositional gradient in the 3d printed component. A criterion must then be selected to define a comparative success between different gradations. Finally, the space of gradient profiles considered must be defined.

The power-law functions are the most recurrent set of gradation profiles considered in the literature. They are defined by $f_b(z) = (\frac{z}{h})^p$ where $f_b(z)$ is the fraction of material b (in an a/b gradation) at height z for a total gradation size of h. The gradation is unidirectional and the exponent p is the parameter to optimize. Choosing p is equivalent to choosing a gradation profile: considering power-law functions is therefore very convenient for optimization. This problem is equivalent to finding the maximum (or minimum) of a function with only one variable, the function being a measure of success of the coating's material gradation profile. Nevertheless, a few studies chose to consider more complex sets of gradation profiles. The number of design variables increases (instead of only one variable, called p for power law functions) and optimizing this set of variables is then harder as it is equivalent with finding the minimum of a function with several variables. In this case, a nature inspired optimization method (particle swarm) was proposed (Kou, et al., 2012). This type of algorithm uses randomness when exploring the variables to optimize and is more computationally efficient than exact algorithm for multi-dimensional (several variables) problem solving.

In the present application, the criterion of success must be based on how well the profile resists to abrasion wear. Studies on a alumina/stainless steel FG material profile concluded that after hardness, compressive residual stresses near the surface of the graded coating (where the alumina is) significantly help to improve wear resistance as they lowered the rates of surface cracking and

grain pull-out (Dancer, et al., 2014) (Xu & Todd, 2015). The abrasive wear mechanism observed for WC reinforced NiCrBSi was similar with a scratching of the matrix followed by the pull-out of the WC particles (Lu, et al., 2003) (P. Wu, 2003). The tensile residual stresses detrimental effect on the abrasive wear resistance of the FGM therefore seems more crucial near the worn surface. A criterion of success could therefore be the lower amount of tensile residual stresses near the graded coating surface.

In FGM applications where mechanical performance is involved, it is common to design the material gradation profile and the graded coating dimension based on the resulting residual stresses (M.H. Yu, 2010) (Liu, et al., 2009). However, the validity of this approach should be confirmed by directly comparing the wear resistances of some FGMs with different gradation profiles and note if the results are coherent with the residual stresses criterion chosen for FGM appraisal (Shi, et al., 2017).

Finally, another aspect independent from the residual stresses that should be considered in the design is the possibility that certain compositions should be avoided to prevent the formation of detrimental secondary phases (Li, et al., 2017). Ideally, these should be avoided through a precise control of process parameters (Oliveira, et al., 2020), but if even the ideal operating parameters do not prevent their formation, then they would become an additional aspect to consider for the FGM design.

1.3.5 Modeling residual stresses in AM of FGMs

Because of the high temperature gradients during the printing process and the different expansion and shrinkage rates of the materials involved, high residual stresses can develop. This section will address how residual stresses may be computed. The typical modeling approach rely on the use of Finite Element Models (FEMs) where stresses increments are computed in a finite volume for a given time step.

In FEM, when in the time domain the time step must be defined, as well as the mesh size. Usually the "birth and death element" technique is used, which means that the unprinted elementary volumes of the desired component are defined before the simulation and "activated" once they are printed. Then, at every time step strain increments are computed (under an assumption of small deformation).

The total strain tensor is:

$$\epsilon = \varepsilon_t + \varepsilon_e + \varepsilon_p + \varepsilon_T \qquad (1\text{-}2)$$

with ε_t being the thermal strain; ε_e the elastic strain; ε_p the plastic strain; and ε_T is the strain due to solid state phase transformations. The latter (solid state phase transformation induced strain) is often negligible compared to the others (Liu, et al., 2014) and is often neglected. The thermal stress increment is computed based on the temperature increment of the finite volume, according to:

$$d\varepsilon_t = \alpha * dT \qquad (1\text{-}3)$$

where α is the coefficient of thermal expansion (CTE).

The mechanical analysis does not impact temperature prediction so the thermal and mechanical analysis can be computed sequentially (Deng, et al., 2007). After the thermal strain is computed, the total strain will be known from the model constraints. Then the sum of the plastic and elastic strains is deduced considering Equation (1-2). The amount of plastic strain is captured with the von Mises yield criterion. Stress is deduced from the elastic strain using Hooke's Law. The material is almost always assumed to be isotropic, but the correctness of this approximation is usually not verified. Due to the successive tensile and compressive stresses experienced in additive manufacturing due to subsequent reheating cycles after each new layer deposition, an elastic-plastic model must be selected, unless the stresses always remain below yield stress. An elastic-perfectly-plastic model may be used for simplicity or because of a lack of information on the material. The Ramberg-Osgood relationship usually describes the tensile reloading behaviour well for metals and can be used for 17-4PH (Mulkey, 1971). Otherwise, kinematic strain hardening (with Bauschinger effect) or isotropic strain hardening (or a mix of the two) may be implemented with a more or less precise empirical formula for the plastic zone stress-strain curve (Mirkoohi, et al., 2020). When the material reaches its annealing temperature after being re-heated by the next weld, it loses its hardening memory (Dean Deng, 2008).

To summarize, the following flow chart (Figure 1-6) represents the FEM method of computation for residual stress predictions at each time step, assuming that the temperature history is known:
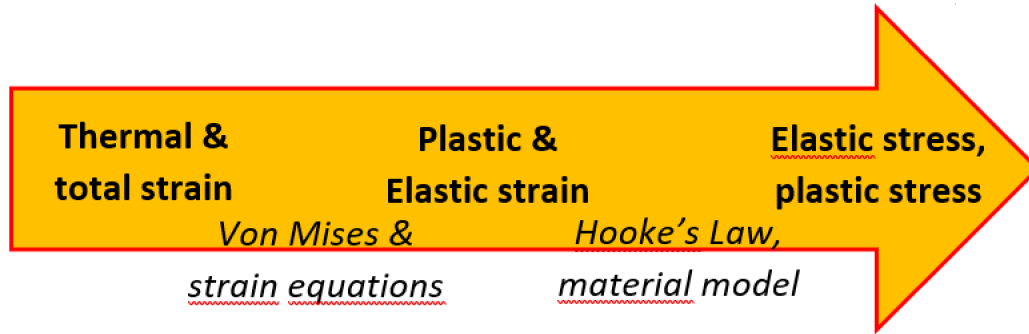
Figure 1-6: FEM residual stress prediction calculation sequence

Additionally, it was reported that peening stress must also be considered for processes with high velocity of incoming particles (Valarezo, et al., 2010) but it is not the case for PTAW. To conclude, it is worth noting that if the tensile stress exceeds the tensile yield stress during cooling, microcracks may also form for brittle layers and result in stress relaxation (Mirkoohi, et al., 2020). Other potential stress relaxation processes include edge relaxation or interfacial sliding (Kuroda & Clyne, 1991).

1.3.6   Modeling the transferred plasma arc and its interaction with the powder particles

The computation of residual stresses first requires the prediction of the temperature history of the printed part during the PTA-AM process, as was described in the previous sub-section. This implies an assessment of the amount of heat transferred from the arc to the weld pool at any given time, and the initial temperature of the deposited weld pool that will inevitably be influenced by the powder particles interaction with the plasma arc. The characteristics of the transferred plasma arc, which must first be evaluated depending on the operating parameters, are an active topic of research that usually involves numerical simulations of the arc, solving magneto-hydrodynamic sets of differential equations (Li, et al., 2020) (Trelles, et al., 2009) (Fudolig, et al., 1997) (Aithal, et al., 1998) (Schnick, et al., 2010). Considering to difficulty to experimentally measure these characteristics, especially the temperature (Gleizes, et al., 2009) (Wolfe, 2010), these numerical models are valuable. These predicted characteristics can then be used to predict the arc heat input on the anode, but also on the powder particles (Wolfe, 2010) (Xibao & Hua, 1998). Alternatively, the arc heat transfer to the anode can also be experimentally measured (Choi & Gauvin, 1982).

1.4 Thesis outline

This thesis aims at predicting the effect of applying different material gradations to the MMC coating on the subsequent residual stresses that develop in it after its deposition through PTA-AM.

The first step towards that goal is to predict the temperature history of the process. The method used to reach that goal is summarized in Figure 1-7. A large-scale thermal simulation of the progressive deposition was run with a finite element software which required the knowledge of two main input variables: the initial layer temperature and the heat received from the arc. The heat received from the arc to the anode will be calculated directly. The initial layer temperature is the temperature first prescribed to the layer finite elements when they are activated to simulate the weld pool deposition. In this work, it is physically interpreted as the temperature reached by the powder particles when they reach the melt pool and mix. It follows that this value depends on both the nature of the powder being injected (proportion of NiBSi vs WC particles, particle size, etc) and the arc characteristics. Therefore, the temperature reached by the NiBSi and WC particles respectively must first be calculated separately to deduce the initial layer temperature.
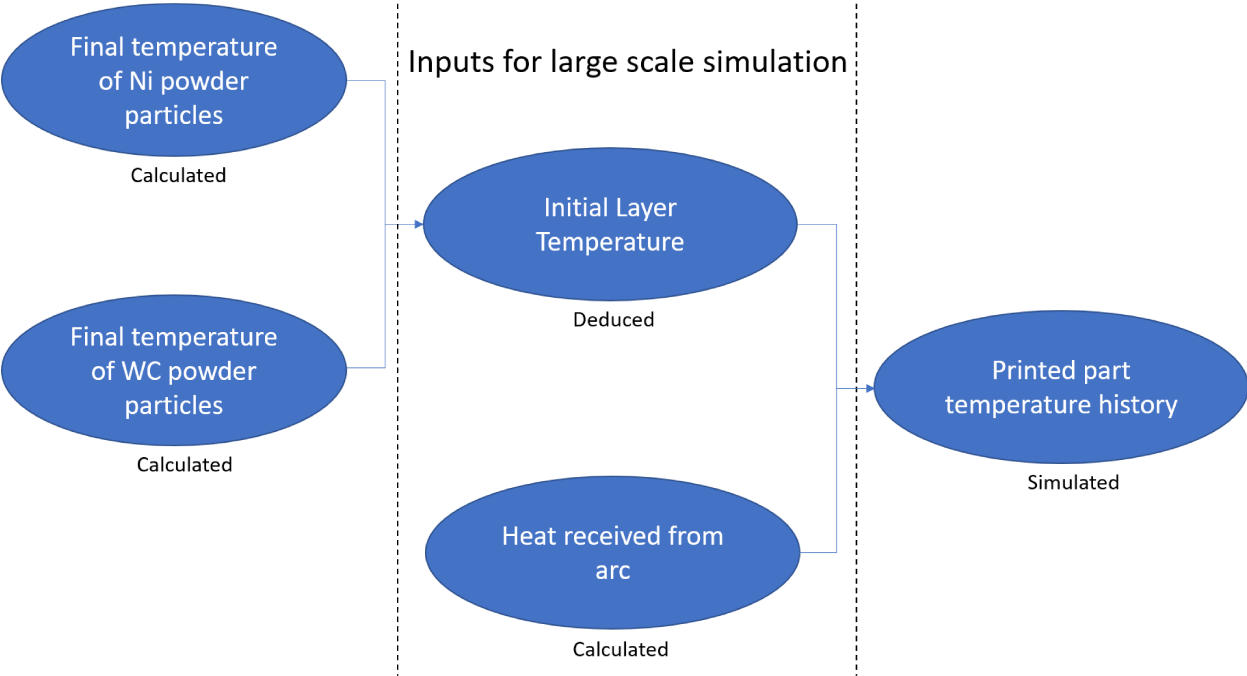
Figure 1-7: Predicting the temperature history of the PTA-AM process

Since the proportion of tungsten carbide powder particles being injected is increasing layer after layer in the context of the AM of a coating graded in WC, it is expected that each layer should have a different initial temperature if the arc characteristics do not change.

Once the temperature history of the AM process is simulated with success on a macro-scale, the thermal strains and stresses that arise from the high temperature gradients and reheating cycles during the deposition can be simulated as well on a finite element software. Eventually, the stresses that remain in the printed part after its cooling to room temperature are predicted (residual stresses). The choice of variation in the material mechanical properties observed for each graded layer, especially the coefficient of thermal expansion, is expected to have a major influence on the profile of these residual stresses.

In Chapter 2, a simplified model is built in order to predict the final temperature reached by both nickel and tungsten carbide particles for a given set of PTA operating parameters, depending on several factors such as particle size, initial injection velocity and injection angle. The model includes a prediction of the particle velocity and temperature history inside the plasma arc, and is compared to experimentally tracked powder particles for validation. The temperatures reached on average by these particles are then given and the initial layer temperature is deduced depending of the WC content. Finally, the heat transfer between the arc and the anode weld plate is also modeled and an estimation is given.

In Chapter 3, the results obtained in Chapter 2 are extended to wider range of PTA-AM operating parameters. In particular, the impact of varying the arc current and of adding hydrogen to the plasma gas is studied quantitatively. The results sensitivity on the parameters they depend on is also evaluated.

In Chapter 4, the results from Chapter 2 and Chapter 3 are used as input data to simulate the thermal history of the PTA-AM of a graded wall on a substrate, using the finite element software Abaqus. Subsequently, the thermal stress history is also simulated for different material gradients. The residual stress profiles eventually obtained for each gradient are compared to each other and conclusions are drawn.

Finally, Chapter 5 summarizes the findings in this thesis and discusses areas where the study of the functionally graded Ni-WC MMC could be deepened.

Chapter 2 : Modeling of the Plasma Transferred Arc Heat Input to Injected Powder Particles and to the Plate

2.1 Introduction

Coatings made of WC-Ni Metal Matrix Composites (MMC) can be used on a mechanical part in oil sands mining in order to enhance its wear and abrasion resistance. Plasma Transferred Arc (PTA) is a welding technique that is adapted to the deposition of such coatings. A schematic of the PTA torch is shown in Figure 2-1 (credit: (Gajbhiye, 2022))
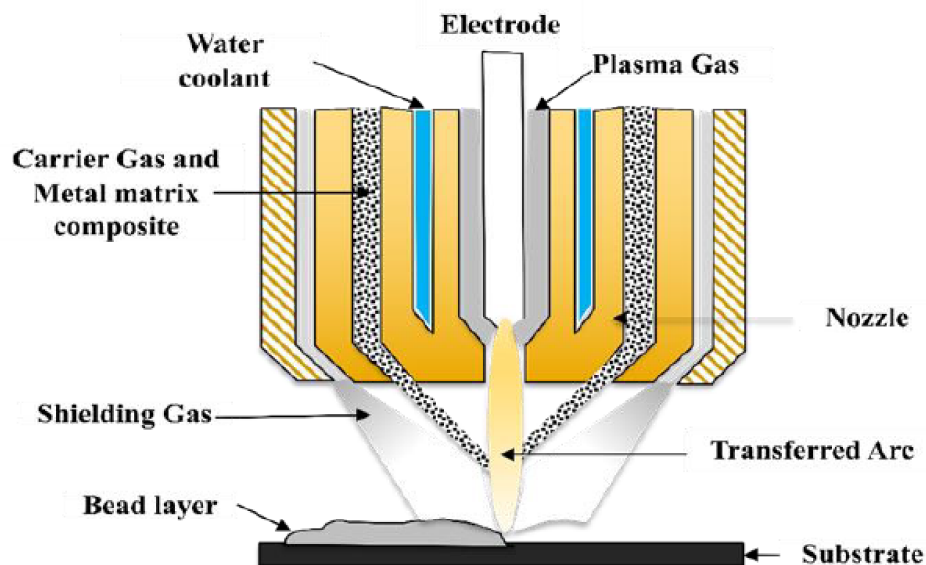
Figure 2-1: Schematic of the Transferred Plasma Arc Welding process (Gajbhiye, 2022)

In PTA welding, the electrode is typically the cathode while the target (substrate) is the anode, thus increasing the power absorbed by the target (Wolfe, 2010). The plasma gas flows through the center of the torch and around the electrode (cathode), before being ionized under the cathode tip. The plasma gas then exits the torch while being constricted by the nozzle. This results in a more concentrated arc with a more collimated shape compared to Gas Tungsten Arc Welding (GTAW). A carrier gas is used to carry a powdered feedstock material, and inject this powder into the arc where the metallic components are melted. Finally, a shielding gas is also fed around

the arc to protect the weld from oxidization. A water-cooling system is used to prevent the torch from overheating.

It is possible to automate the PTA and use it for Additive Manufacturing (AM) if the appropriate operating parameters are selected. To perform a macro-scale simulation of the temperature history of the PTA-AM process by discretizing the problem with a Finite Element software such as Abaqus, it is then necessary to conduct some micro-modeling beforehand in order to estimate the Heat Input (HI) from the plasma arc to the weld pool and to the flowing powder respectively. Indeed, the HI from the arc results from complex physics and can be influenced by many different operating parameters.

The operating parameters that can be selected in PTA-AM and that will affect the thermal history of the process are the following: Plasma Gas Flow Rate, Carrier Gas Flow Rate, Shielding Gas Flow Rate, Powder Flow Rate, Powder Composition, Powder Size Distribution, Powder Injection Angle and Initial Velocity Distribution, Nozzle to Substrate Standoff-Distance (or Voltage), Current, Gas Composition, Torch Travel Speed, Electrode Composition and Tip Angle. These parameters will determine the average temperature reached by the powder particles when entering the weld pool (and therefore the initial temperature of the deposited bead), and the heat transferred directly from the plasma arc to the weld pool.

The present Chapter attempts to account for as many variables as possible in order to predict the temperature history and trajectory of the powder particles in the transferred plasma arc, and deduce the initial temperature of each PTA-AM weld under the studied conditions. The Heat Input from the torch to the substrate is also estimated and generalized as the Heat Input received by each PTA-AM subsequent weld.

2.2 Estimation of the Average Temperature and Velocity of the Transferred Plasma Arc

The purpose of this section is to give an estimate of the average plasma arc temperature and of the axial velocity radial profile. All the other properties of the arc (density, etc) can then be deduced from the plasma temperature since, as will be verified, the pressure is close to atmospheric pressure everywhere.

In order to give these estimates, a simplified model of the plasma arc is built. The plasma arc is schematized in Figure 2-2 and the model assumptions are given below. Focus is made on the Local Thermodynamic Equilibrium (LTE) zone of the plasma, where the powder particles are heated as they are dragged to the anode (Cf. Figure 2-2).
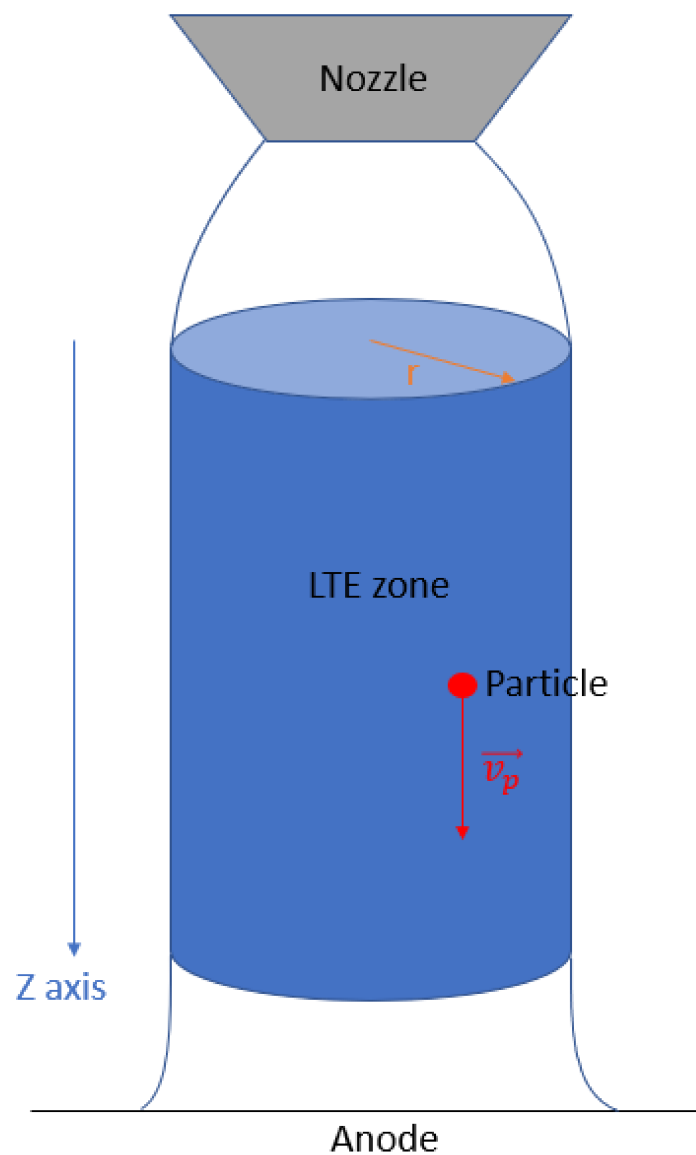
Figure 2-2: Schematic of the Plasma Arc with a Powder Particle

The assumptions are the following:

- The plasma arc is stationary
- Outside of the immediate vicinity of the cathode and anode, the plasma is in LTE (Local Thermodynamic Equilibrium), meaning that the electrons and heavy particles (atoms and ions) in this region of the plasma have the same temperature.
- The arc is axially symmetric and can be a cylinder shape with the same inner radius as the constricting nozzle (2mm). Cylindrical coordinates will be used.
- The current density is uniform and purely axial.
- There is a negligible amount of metallic vapor emanating from the powder and weld pool, therefore it does not affect the plasma temperature nor generate a thermal screening effect around the powder particles.
- The flow is laminar. This will be verified by evaluating the Reynolds number.
- The plasma is optically thick, meaning that some radiations are re-absorbed within the plasma.
- The plasma can be modeled as a perfect fluid (negligible viscosity) everywhere except at the boundary with the powder particles or the electrodes.
- The LTE zone of the plasma can be approximated as isothermal. Given the constricted and condensed nature of the transferred plasma arc, this assumption is more reasonable than it would be for GTAW for example.
- The carrier gas flow and shielding gas flow have no effect on the plasma temperature and velocity.
- The powder has a negligible influence on the plasma temperature and velocity. This is verified with calculations, considering the powder flow rate and size in use.

2.2.1 Plasma Temperature

The goal of this sub-section is to evaluate the average plasma temperature without resorting to running a complete numerical simulation of the arc. The collimated transferred plasma arc is then approximated as isothermal.

2.2.1.1 Calculation Method

The first thing to consider is that in the range from 10 000 to 20 000K, the conduction in the plasma and the heat loss through the sides of the arc are not significant compared to radiation losses, while axial heat transfer is dominated by convection rather than conduction (Dowden & Kapadia, 1994). However, axial convective heat transfer – especially, convection from the hotter part of the plasma under the cathode moving down to the central point – may not be negligible compared to radiation losses. The region of interest in this study is the bottom half of the plasma arc as this is the region where the powder particles enter and travel through the plasma due to their injection angle so the temperature in this region is representative of the temperature seen by the heated powder. In the bottom, or anode side, of the plasma arc, the axial convective heat transfer is less significant than on the cathode side. It is assumed that the plasma gas flow rate used in this work (1.5 lpm) is low enough for the anode zone of the plasma to not be significantly heated by the upstream gas, which is hotter on average.

Considering the above assumptions, the local heat balance equation in the central axis of the bottom region of the arc may be reduced to a simple form where the Joule heating is balanced by the net radiation losses (Equation (2-1)):

$$\frac{j^2}{\sigma} - 4\pi\varepsilon_T = 0 \qquad (2\text{-}1)$$

In this equation, j is the current density (considered uniform) and σ is the temperature dependent plasma electrical conductivity. The temperature dependent properties of the argon plasma can be found in (Boulos, et al., 1994). The Net Emission Coefficient (NEC) ε_T indicates, for a homogeneous and isothermal plasma sphere in LTE, the net radiation (emission minus absorption) emitted from the sphere center to outside of the sphere, per unit volume and solid angle. The NEC is then a function of two variables: a temperature and a radius. Assuming an optically thin plasma is equivalent to saying that the plasma NEC at any radius is equal to its

NEC at a radius of 0 (no absorption of the emitted radiations). The alternative assumption, that is made in this work, is that of an optically thick plasma. Even though a spherical geometry is assumed when calculating the NEC, the values may also be applied to a cylindrical geometry. Detailed calculations show that the net emission coefficient in the central axis of an infinite isothermal plasma cylinder is very close to that of the center of a plasma sphere of same radius and temperature (Cressault, 2008). Furthermore, despite the restrictive assumptions of the plasma being homogeneous and isothermal, this coefficient may be used in models of a real plasma arc because the net emission of a point belonging to the hottest regions of the plasma is mainly a function of the composition and temperature at this point, provided that the dimensions of the plasma are greater than (or of the order of) about 1mm (Cressault, 2008). The effect of the plasma arc temperature decreasing to some extent near the edges is therefore minimal for the arc considered by this work which has a radius of 2mm. However, the effective absorption radius describing best the net radiation losses in the central axis might be slightly different from 2mm. The idealisation of the plasma arc temperature for the application of Equation (2-1) with the net emission losses is shown in Figure 2-3.
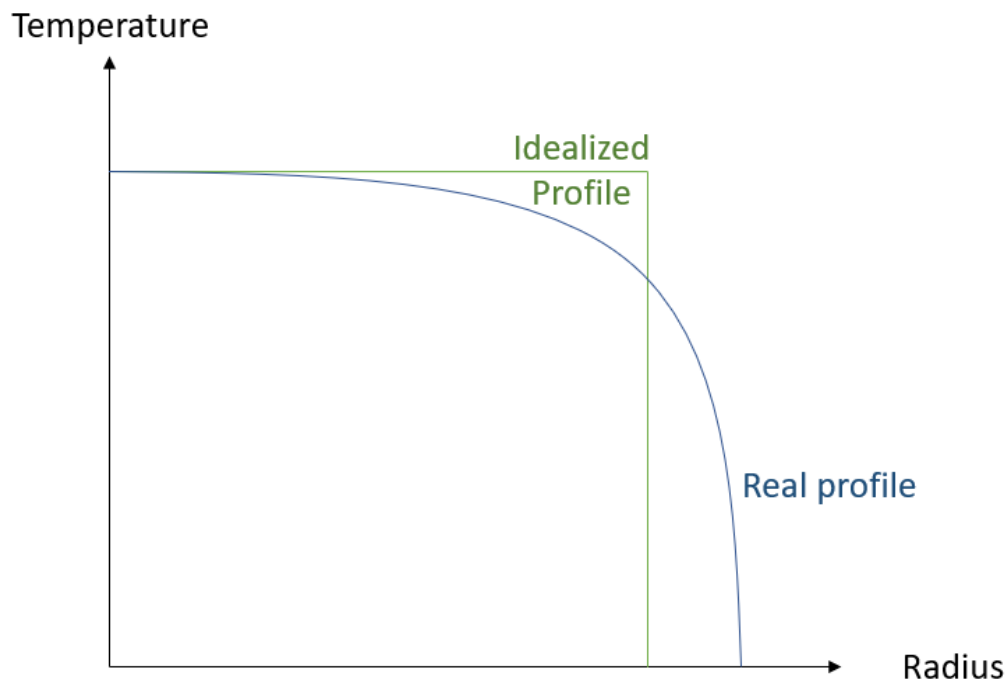
Figure 2-3: Idealized radial profile of the transferred plasma arc temperature for calculation of net emission losses

It is critical to use a correct estimation of the NEC which increases exponentially with the temperature and decreases with the plasma radius. For example, for argon and hydrogen, the coefficient of net emission increases dramatically with temperature below a threshold of about 15 000K, before the progression gets slower (Cressault, 2008).

The data for the NEC values of pure argon plasma and for mixtures of argon and hydrogen at various temperatures was extracted from the literature (Cressault, 2008), (Cressault, et al., 2010), (Menart & Malik, 2002), (Gleizes, et al., 1990) for radii ranging between 1mm and 1cm. Due to the fact that the data reported in these references were in relative but not perfect agreement, and since the radius of absorption best representing the plasma arc studied is not exactly known, the real NEC was considered to range between the extremum values extracted from these references for a given temperature. These extremum values are reported in Appendix B under the form of fitting equations depending on the temperature. This approximation of the NEC typically results in a plasma temperature approximation of ±500K using Equation (2-1).

2.2.1.2 Validation of the method

To evaluate the reliability of this approach, the average arc temperatures deduced from Equation (2-1) are here compared to results published in the literature ((Fudolig, et al., 1997), (Aithal, et al., 1998) and (Schnick, et al., 2010)), where numerical models of transferred plasma arcs comparable to the one studied in this work were developed. The average temperature in the bottom half of each of these arcs was roughly estimated from the general results reported in these works and then systematically compared to the predictions one would make with Equation (2-1) in Table 2-1, Table 2-2 and Table 2-3.

In the first reference considered (Fudolig, et al., 1997), the authors predicted the temperature profile of a pure argon and of a 90%Ar/10%H_2 transferred plasma arc at 200A and 250A with an optically thin plasma assumption and for a nozzle inner radius of about 3.3mm. The comparison of their results with what one would predict using Equation (2-1) is displayed in Table 2-1.

Table 2-1: Comparison of average temperature predictions for a transferred plasma arc

Type of Gas and Current	250A Argon	200A 90%Ar/10%H_2
Reference (Fudolig, et al., 1997)	15 000K	13 500K
Equation (2-1)	13 700 - 14 800K	12 700 – 13800K

It can be seen from Table 2-1 that the temperatures predicted by reference (Fudolig, et al., 1997) correspond approximately to the upper end of the range of predictions obtained using Equation (2-1).

In the second reference considered (Aithal, et al., 1998), the authors have undertaken the construction of a numerical model of a transferred argon plasma arc which was assumed to be optically thin, with a 1.6mm nozzle inner radius. The currents simulated were 100A and 150A and the gas used was always pure argon. The comparison of their results with what one would predict using Equation (2-1) is displayed in Table 2-2.

Table 2-2: Comparison of average temperature predictions for a transferred plasma arc

Type of Gas and Current	100A Argon	150A Argon
Reference (Aithal, et al., 1998)	17 000K	20 500K
Equation (2-1)	15 100 – 17 800K	17 500 – 20 700K

It can be seen from Table 2-2 that the temperatures predicted by reference (Aithal, et al., 1998) correspond approximately to the upper end of the range of predictions obtained using Equation (2-1).

In the third reference considered (Schnick, et al., 2010), another numerical model of a transferred plasma arc was conducted while considering the variation of several parameters. This time, the authors used net emission coefficients to evaluate the emitted radiation. The nozzle inner radius

was 1.5mm. The comparison of their results with what one would predict using Equation (2-1) is displayed in Table 2-3.

Table 2-3: Comparison of average temperature predictions for a transferred plasma arc

Type of Gas and Current	Reference (Schnick, et al., 2010)	Equation (2-1)
Argon 40A	13 000K	13 200 – 13 900K
Argon 60A	15 000K	14 000 – 15 600K
Argon 80A	16 500K	14 800 – 17 300K
Argon 100A	18 000K	15 600 – 18 600K
Argon 120A	19 500K	16 800 – 20 100K
Ar/5%H_2 100A	16 500K	15 000 – 18 000K

It can be seen from Table 2-3 that except for argon at 40A and for 95%Ar/5%H_2 at 100A, the temperatures predicted by reference (Schnick, et al., 2010) are closer to the upper end of the range of predictions obtained using Equation (2-1). For the case of 95%Ar/5%H_2 at 100A, the reported temperature is around the median value of the range of predictions obtained using Equation (2-1).

Based on all these comparisons, and especially the comparison with (Schnick, et al., 2010) where the authors used coefficients of net emission, it seems that the range of possible temperatures predicted using Equation (2-1) is close enough to the numerically predicted temperatures in the central axis of the arc in the region near the anode, where convective heat transfer from the cathode is minimal. For the case of pure argon, it seems that a temperature closer to the upper end of the range of predictions is better suited, while for argon with 5% hydrogen content a median value may be better suited.

In the context of the present work, an argon arc with a current of 50A is considered, and the nozzle inner radius is 2mm. Using Equation (2-1), it is predicted that the average arc temperature in the bottom half (anode side) should range between 12 600K and 12 900K. A temperature of 12 800K will therefore be selected for the rest of this work.

2.2.2 Plasma Velocity

The goal of this sub-section is to evaluate the radial profile of the plasma axial velocity without resorting to running a complete numerical simulation of the arc.

2.2.2.1 Calculation Method

The driving force for the plasma flow is assumed to be the magnetic pressure gradient generated by the Lorentz forces. Gravity is totally negligible, and, as will be verified, the constriction of the nozzle on the thermally expanding plasma should not be significant with the plasma gas flow being used in this work (1.5 lpm at room temperature).

The current density is assumed to be uniform:

$$\vec{j} = j_z\vec{e_z} = J\vec{e_z} \quad \text{with } J = \frac{I}{\pi r_a^2} \tag{2-2}$$

in which I is the current and r_a is the arc radius which may depend on the section height z.

Due to the Curie principle, the magnetic field generated by the uniform current density can be expressed in the following form:

$$\vec{B} = B_\theta(r,z)\vec{e_\theta} \tag{2-3}$$

Applying Ampère's theorem for r < r$_a$ then gives:

$$B_\theta(r,z) = \frac{\mu_0 J}{2} \tag{2-4}$$

Consequently, the Lorentz forces are expressed as

$$\vec{j} \wedge \vec{B} = \frac{-\mu_0 J^2}{2} r\vec{e_r} \tag{2-5}.$$

These Lorentz forces generate a radial pressure gradient defined by:

$$P(r) = \int_{r_a}^{r} (\vec{j} \wedge \vec{B}) . \vec{e_r} dr \tag{2-6}$$

Finally, the Maecher pressure is obtained:

$$P(r) = \frac{\mu_0 I^2}{4\pi^2 r_a^2}\left(1 - \left(\frac{r}{r_a}\right)^2\right)$$

(2-7)

with μ_0 being the vacuum magnetic permeability, and r the radial distance between the vertical axis and the point where the pressure is evaluated.

The electromagnetic pressure will be most elevated just below the cathode where the plasma is at its narrowest. The plasma arc radius will then increase as it flows and exits the torch. In the work of (Aithal, et al., 1998) the radial profile of ionization fraction was displayed at the exit plane of the torch for the transferred plasma arc the authors were simulating. It can be seen that the ionization fraction falls below 50% at less than a quarter of the nozzle inner radius. In this work, it will be assumed that the radius of the ionized portion of the gas only starts to increase noticeably after exiting the nozzle, and therefore that the electromagnetic pressure only starts to decrease below the nozzle. Due to this assumption, it seems reasonable enough to approximate the axial decrease in pressure as isothermal (although there should in fact be some axial decrease in temperature). In what follows then, the entire LTE region of the plasma below the nozzle will be considered as isothermal for velocity calculations, and the upstream pressure will be considered to be about the same as just under the cathode.

The plasma density is considered constant since the plasma is approximated as isothermal, and since the electromagnetic pressure is small compared to atmospheric pressure. The viscosity of the plasma gases around 14000K is considered negligible everywhere except in the boundary layer around the powder particles. Then, by applying the Bernoulli equation under the assumption of an incompressible, homogeneous, laminar and stationary flow of a perfect fluid, the following relation is obtained between two points in a given trajectory:

$$\rho\frac{v_c^2(r)}{2} + P_c(r) = \rho\frac{v_a^2(r)}{2} + P_a(r)$$

(2-8)

(the gravity term $\rho g z$ has a negligible variation)

In Equation (2-8), the subscript c means at the immediate vicinity of the cathode, the subscript a means in the plasma arc LTE zone outside of the nozzle, v is the plasma velocity, ρ is the plasma density and P is the pressure. The plasma radius just under the cathode will henceforth be noted r_c, and is considerably smaller than the plasma radius past the nozzle which will remain noted r_a and is assumed to be equal to 2mm (inner radius of nozzle). It follows that:

$$P_c(r) = \frac{\mu_0 I^2}{4\pi^2 r_c^2}\left(1 - \left(\frac{r}{r_a}\right)^2\right)$$

(2-9)

With a plasma gas flow rate of 2 slpm, and a pipe of radius 2mm for example, the initial flowing speed would be 2.65 m/s. Such a value is negligible compared to the velocity generated by the electromagnetic forces. Therefore, the effect of the plasma gas flow rate on the initial plasma velocity is neglected, and the plasma gas is assumed to have a velocity of 0 before being ionized under the cathode tip.

With $v_c^2 \approx 0$, the following comes:

$$v_a(0) = \sqrt{\frac{\mu_0}{2\rho}}\frac{I}{\pi}\sqrt{\frac{1}{r_c^2} - \frac{1}{r_a^2}} \approx * \sqrt{\frac{\mu_0}{2\rho}}\frac{I}{\pi r_c}$$

(2-10)

*since $r_c{}^2 \ll r_p{}^2$.

$$v_a(r) = v_a(0)\sqrt{1 - \left(\frac{r}{r_a}\right)^2}$$

(2-11)

A correct estimation of r_c is then essential to predicting the plasma velocity.
It is theorized that the cathode tip is brought close to melting temperature by the hot plasma and that the hot white zone of the cathode tip is thermionically emitting electrons thus defining the initial current density (Lowke, 1979). The radius of the emitting zone is r_c. It cannot be measured easily so this radius is evaluated through the relation:

$$r_c = \sqrt{\frac{I}{\pi j_c}}$$

(2-12)

28

The main difficulty is then to estimate the j_c value which is not affected significantly by the current but depends strongly on the electrode tip angle (Lee & Na, 1996; McKelliget & Szekely, 1986). The thermionic emission at the cathode surface which is following the Richardson equation (Equation (2-13)) is highly dependent on (and increases with) the cathode tip temperature where the emission occurs (Lee & Na, 1996).

$$j = AbT^2 exp\left(\frac{-\Phi}{k_B T}\right) \qquad (2-13)$$

In Equation (2-13), A is the Richardson constant (whose value is multiplied by a material dependent corrective factor b), T is the electrode tip temperature, Φ the work function of the electrode material, and k_B the Boltzmann constant. The value of A*b and Φ are estimated at 3.0 A.cm^{-2}.K^{-2} and at 2.63eV for thoriated tungsten respectively (Wolf, 1995), and $k_B = 8.62*10^{-5}$ eV.K^{-1}.

Sharper electrodes have hotter tips due to their reduced conductive cooling compared to the blunt ones (Abid, et al., 2013; Coudert, et al., 1993), so their thermionic emission and the resulting cathode current density should be higher (see Equation (2-13)), producing higher plasma velocity (considering Equations (2-10) to (2-12)). The fact that sharper electrodes produce higher plasma velocity is confirmed by experimentally by (Abid, et al., 2013).

Whether the electrode is in tungsten or thoriated tungsten also influences the cathode current density due to different plasma/cathode contact zone leading to a different cathode tip temperature (pure tungsten will be hotter) (Nestor, 1962; Zhou & Heberlein, 1998). In this work a sharp thoriated tungsten electrode of 3.2mm diameter with 20° angle tip is used. For such an electrode, the value of current density was selected based on the literature at $1x10^8$ A/m^2 for a 5mm long arc (Abid, et al., 2013). The radius deducted is $r_c = 0.399mm$ for a current of 50A, $r_c = 0.437mm$ for a current of 60A or $r_c = 0.564mm$ for a current of 100A.

Consequently, assuming a plasma temperature of 12 800K and a nozzle inner radius of 2mm the argon plasma velocity along its centerline $v_a(0)$ is computed to be 175 m/s at 50A.

2.2.2.2 Assumption verification

The electromagnetic pressure under the cathode tip computed with Equation (2-9) is in the order of the kPa, which is a negligible variation compared to atmospheric pressure. Therefore, the properties of the plasma can be kept at 1 bar (=101kPa) value everywhere, and since the plasma is approximated as isothermal, the hypothesis of a constant density (leading to the Bernoulli equation) is valid in this model.

With these results, the assumption that the gas flow rate is low enough for the nozzle constriction to not contribute significantly to an additional acceleration of the arc must be verified. Assuming a cylindrical arc core of radius r_a due to the nozzle collimating effect, and considering the conservation of the mass throughout the flow, the plasma gas flow rate may be expressed by Equation (2-14):

$$\rho_0 \dot{V} = \dot{m} = \rho \pi r_a^2 V \qquad (2\text{-}14)$$

where ρ and ρ_0 are the plasma arc core density and the room temperature unionized gas density respectively, $\dot{V}$ is the volume flow rate (selectable operating parameter) and V the flowing speed.

The flowing speed can be deduced by combining Equation (2-14) with the relation:

$$\dot{m} = \rho \int_0^{r_a} v_a(r) 2\pi r dr \qquad (2\text{-}15)$$

which with Equation (2-11) is rewritten as

$$\dot{m} = \rho \int_0^{r_a} 2\pi r v_a(0) \sqrt{1 - \left(\frac{r}{r_a}\right)^2} \, dr \qquad (2\text{-}16)$$

Or

$$\dot{m} = \rho 2\pi r_a^2 v_a(0) \int_0^1 R\sqrt{1 - R^2} dR \qquad (2\text{-}17)$$

the last integral in Equation (2-17) being equal to $\frac{1}{3}$.

The flowing speed is then deduced by combining Equations (2-14) and (2-17):

$$V = \frac{2}{3} v_a(0) \qquad (2\text{-}18)$$

Since $v_a(0)$ was calculated at 175 m/s then V=117 m/s.

Assuming that Equations (2-10) to (2-12) are correct for the plasma gas flow rate selected, the mass flow rate of the plasma may also be expressed as:

$$\dot{m} = \sqrt{\frac{2\mu_0 j_c}{9\pi}} \sqrt{\rho I} \pi r_a^2 \qquad\qquad (2\text{-}19)$$

The term $\sqrt{\frac{2\mu_0 j_c}{9\pi}}$ being constant, $\dot{m} \sim \sqrt{\rho I} \pi r_a^2$. If the current is set, the temperature and therefore the density of the plasma should be set as well. This means that if the plasma gas flow rate is decreased to below a certain threshold ($\dot{m}_t = \sqrt{\frac{2\mu_0 j_c}{9\pi}} \sqrt{\rho I} \pi r_n^2$, where r_n is the inner radius of the nozzle (2mm)), the radius of the plasma arc core should be reduced as well. However, if it is increased to more than this threshold, the constriction effect of the nozzle should have an acceleration effect on the plasma. The plasma gas flow rate is set at 1.5 lpm (at room temperature) which corresponds to 0.045 g/s. If $\dot{m}$ is set at 0.045 g/s in Equation (2-18), one can find r_a = 2.0 mm. Inversely, if r_a is set at 2 mm one will find $\dot{m}$ = 0.046 g/s. This means that the plasma gas flow rate computed with the velocity profile expressed in Equations (2-10) and (2-11) and assuming a temperature of 12 800K is very close to the selected flow rate of 1.5 lpm. In other words, there should not be any significant additional acceleration of the plasma due to the nozzle constriction of the thermally expanding plasma.

Finally, the initial assumption of a laminar flow may be verified by evaluating the Reynolds Number. The Reynolds number for the highest velocity (at the central axis) is 100, which confirms that the flow is laminar.

In conclusion, the plasma arc axial velocity will be considered to follow Equation (2-10) at the center (resulting in 175 m/s for the 50A argon arc) and its radial profile to follow Equation (2-11).

2.3 Plasma-powder particle interaction

In this section, the temperature and velocity evolution of any given spherical powder particle during its journey inside the plasma arc is evaluated. For simplicity, the powder particle is assumed to travel vertically alongside the plasma flow, which is locally uniform (Figure 2-4). A boundary layer forms around the powder particle that will affect the drag force applied by the plasma (F_d) and the heat transfer by convection (Figure 2-4). The powder particle may experience some degree of melting.
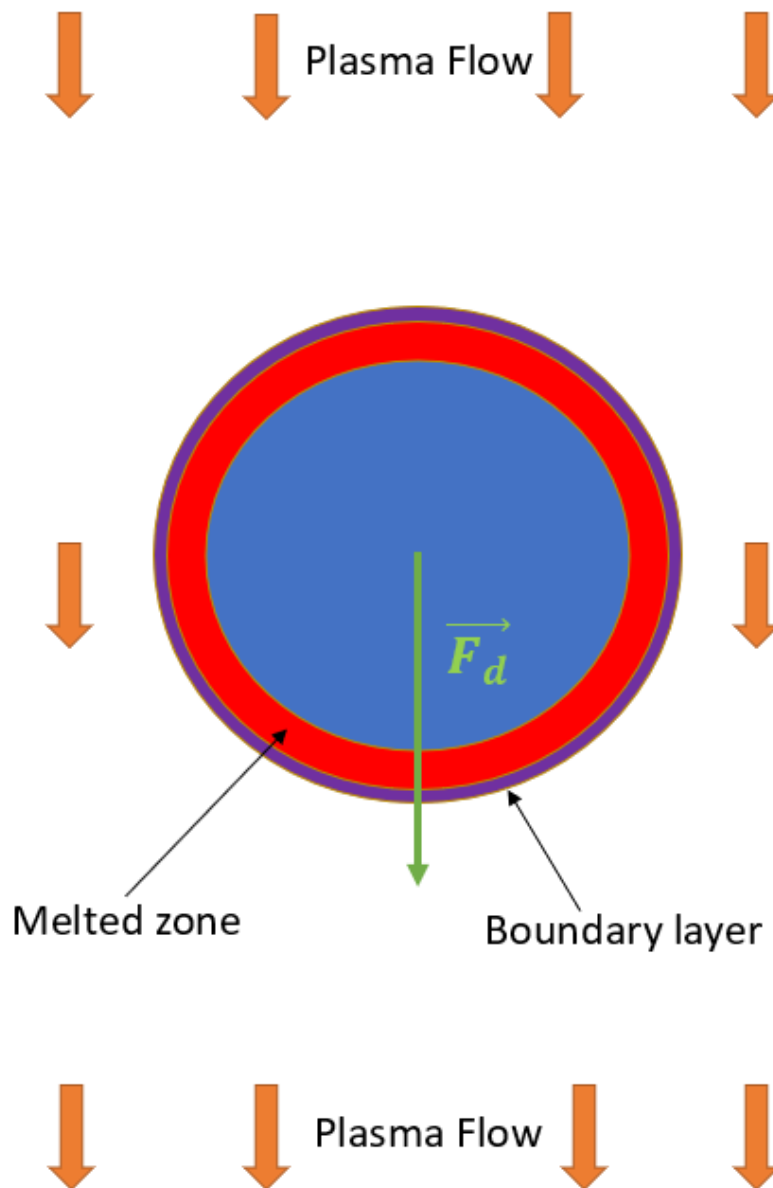
Figure 2-4: Dragging and Heating of a Powder Particle

2.3.1 Heating of the Powder Particle

This subsection describes the physics involving a spherical powder particle of any given material being heated by the plasma arc. Only spherical particles were considered for simplicity; but for a non-spherical particle it is expected that the heating rate by convection would be higher due to the increased surface to volume ratio (the sphere is the geometry with the smallest ratio).

In this Chapter, the subscript g means that the property is taken at the plasma gas temperature, m means taken at intermediate temperature between the plasma gas and the particle surface (a median value is suitable), av means that the property is integrally averaged between the plasma gas and the particle surface temperature, and s means taken at the particle surface temperature.

2.3.1.1 Convective heat transfer: general expressions

The powder particle is heated by the plasma through radiation and convection.

The Newton Law for the convection heat transfer to the spherical particle of radius r_p is:

$$Q_c = 4\pi r_p^2 . h(T_g - T_p) \qquad (2\text{-}20)$$

where h is the coefficient of heat transfer, T_p is the particle temperature and T_g is the plasma gas temperature.

Depending on the authors, the coefficient of heat transfer can be expressed as (Wan, et al., 1999; Yoshida & Akashi, 1977):

$$h = \frac{Nu.k_m}{d_p} \qquad (2\text{-}21)$$

or (Doucet & Flour, 1996)

$$h = \frac{Nu.k_g}{d_p} \qquad (2\text{-}22)$$

other authors consider the average conductivity (Ettouil, 2008; Bourdin, et al., 1983; Bobzin & Öte, 2017; Paik, et al., 1993; Chen, 1999)

$$h = \frac{Nu.k_{av}}{d_p} \tag{2-23}$$

where Nu is the Nusselt number, d_p is the powder particle diameter and k is the plasma thermal conductivity.

The Nusselt number may be expressed as (Wan, et al., 1999) (Lee, et al., 1985) (Chyou & Pfender, 1989):

$$Nu = \left(2 + 0.6 * Re_m^{\frac{1}{2}}.Pr_m^{\frac{1}{3}}\right) \tag{2-24}$$

Or (Djebali, et al., 2015):

$$Nu = \left(2 + 0.514 * Re_m^{\frac{1}{2}}.Pr_m^{\frac{1}{3}}\right) \tag{2-25}$$

where Re is the Reynolds number and Pr the Prandtl number.
These expressions are rooted in the Ranz & Marshall correlation.

The Reynolds and Prandtl numbers characterizing the thermal boundary layer are defined as (Wan, et al., 1999):

$$Re_m = \frac{\rho_m(v_a-v_p)d_p}{\mu_m} \tag{2-26}$$

$$Pr_m = \frac{\mu_m c_{p,m}}{k_m} \tag{2-27}$$

where μ is the dynamic viscosity, c_p the specific heat, ρ the density and v_a and v_p the plasma arc and powder particle velocities respectively.

However, different effects affect the heat transfer and the Nusselt number should be adjusted to take these effects into account. The effective Nusselt number is (Wan, et al., 1999) (Chen, 1999) (Chen & Pfender, 1983):

$$Nu_{eff} = Nu.f_{vp}.f_{Kn}.f_{ev} \tag{2-28}$$

where f_{Kn}, f_{pc}, and f_v are multiplicative factors respectively accounting for the Knudsen effect, the sharp variation of the plasma properties in the boundary layer with the powder particle, and

the mass transfer and screening effect generated by evaporation. Since it is assumed that no evaporation occurs, f_v is taken as 1 in this work (no effect). However, if vaporization from the nickel particle was observed for example, the contamination of the plasma by the metal vapor would greatly reduce the heat transfer to the particle (f_v<1) (Chen, et al., 1985) and it would also affect the net radiations from the plasma as was shown with calculations for other metals (Gleizes, et al., 1990) (Essoltani, et al., 1994), thus changing the plasma temperature.

2.3.1.2 Varying properties correction factor

The boundary layer between the particle and the plasma is characterized by an extreme temperature gradient, and therefore strongly varying plasma properties which affect the heat transfer. Corrective factors for the Nusselt number are proposed in the literature to account for that phenomenon. Different expressions were suggested in the literature; they are summarized and discussed in this section.

First proposition:

$$f_{vp} = (f_{prop})^{0.6} \; Correction \; of \; Fiszdon \; \text{(Fiszdon, 1979)} \qquad (2\text{-}29)$$

$$f_{prop} = \frac{\rho_g \mu_g}{\rho_s \mu_s} \qquad (2\text{-}30)$$

Which can be found in:

(Fiszdon, 1979; Lee, et al., 1985; Ettouil, 2008; Doucet & Flour, 1996)

Second proposition:

$$f_{vp} = \left(\frac{\eta_m}{\eta_g}\right)^{0.15} \; Correction \; of \; Lewis \; and \; Gauvin \; \text{(Lewis & Gauvin, 1973)} \qquad (2\text{-}31)$$

Which can be found in:

(Lewis & Gauvin, 1973; Boulos & Gauvin, 1974; Lee, et al., 1985; Ettouil, 2008; Doucet & Flour, 1996)

Third proposition:

$$f_{vp} = (f_{prop})^{0.6} \left(\frac{c_{p,g}}{c_{p,s}}\right)^{0.38} \quad Correction\ of\ Lee\ and\ al\ \text{(Lee, et al., 1981)} \qquad (2\text{-}32)$$

$$f_{prop} = \frac{\rho_g \mu_g}{\rho_s \mu_s} \qquad (2\text{-}33)$$

Which can be found in:

(Lee, et al., 1985; Ettouil, 2008; Wan, et al., 1999; Doucet & Flour, 1996)

f_{prop} is given by (Wan, et al., 1999) (Chen, 1999) (Chen & Pfender, 1983)

Finally, in the work of (Vardelle, et al., 1983), no correction factor is used but instead the properties of the plasma (density and viscosity) are averaged between the particle surface temperature and the plasma gas temperature (Doucet & Flour, 1996). For the viscosity for example, this gives:

$$\mu_{av} = \frac{1}{T_g - T_p} \int_{T_p}^{T_g} \mu_g(T)dT \qquad (2\text{-}34)$$

Then instead of evaluating the Reynolds number around the particle by taking the plasma properties at a median temperature between the plasma and the particle surface, the temperature averaged properties are used:

$$Re_m = \frac{\rho_{av}\ (v_a - v_p)d_p}{\mu_{av}} \qquad (2\text{-}35)$$

The Prandtl number is evaluated the same way. Finally, they also replace k_g with k_{av} in Equation (2-22). The same method was also used in (Bobzin & Öte, 2017).

The correlation that the literature calls of "Lewis and Gauvin" is derived from an experimental correlation by (Ahmed, 1968) for Reynolds numbers at the boundary layer ranging between 5 and 40 for plasma gases that neither contain argon or hydrogen. The experimental conditions under which this correlation was found are therefore different from this work.

Comparison between these different correlations was made in (Doucet & Flour, 1996; Lee, et al., 1985). Both works conclude that as long as the same conductivity is selected in Equation (2-21), the results of correlations - are similar for plasma temperatures below approximately 10 000K,

but diverge with that of Lee above that temperature. In particular, the correlation of Lee is the only one that returns a decreasing heat transfer coefficient after 13500K (Doucet & Flour, 1996). They also notice that the choice of plasma conductivity in Equation (2-21) leads to major differences.

A comparative study (Lee, et al., 1985) that included a numerical computation of the Nusselt number showed that among the previous correlations, the Lee & al. correlation was the most suited when taking the case of an argon plasma at 10 000 or 12 000K and with a weld pool surface temperature of 2 500 or 3 000K respectively. Therefore, it seems that the Lee & al. correlation is acceptable for the present work.

However, another correlation was proposed by Chen (Chen, 1988):

$$Nu_{prop} = 2[1 + 0.63 Re_g Pr_g^{0.8} \left(\frac{Pr_s}{Pr_g}\right)^{0.42} (f_{prop})^{0.52} C^2]^{0.5} \qquad (2\text{-}36)$$

$$C = (1 - \left(\frac{h_s}{h_g}\right)^{1.14})/(1 - \left(\frac{h_s}{h_g}\right)^{2}) \qquad (2\text{-}37)$$

Which can be found in:

$(Paik, et\ al., 1993;\ Ettouil, 2008;\ Chen, 1999)$

In a similar study as in (Lee, et al., 1985), Chen has evaluated the applicability of the previous correlations and concluded that only their own was satisfactory for both argon, argon-hydrogen mixture and nitrogen plasma and for a range of plasma temperatures up to 16 000K and plasma-particle relative velocities up to several hundred m/s and particle radius from microns to 100 microns (Chen, 1988). The author also compared his results to experimental data and found better agreement with his own correlation compared to the other correlations.

The above-mentioned range of plasma-particle conditions corresponds exactly to the range studied in this work. Therefore, the correlation of Chen (2-36) will be used to evaluate the Nusselt number. For the operating conditions used in this work, the corrected Nusselt number in (2-36) will always be lower than the uncorrected Nusselt number (2-24), meaning that the boundary layer has the effect of reducing the heat transfer to the particle.

2.3.1.3 Knudsen effect

The Knudsen effect is a rarefaction effect causing a reduction of the plasma-particle heat flux as small particle sizes and/or low gas pressures are involved (Chen, 1988). It can also be called a non-continuum effect as the particle size becomes of the order of the local mean free path of the gaseous particles surrounding it. The Knudsen number is introduced to measure this effect.

The Knudsen number Kn describes different regimes of convective heat transfer (Chen, 1999). It is defined by the ratio between the mean free path length of the gaseous particles in the powder particle boundary layer, to the diameter of the powder particle suspended in the plasma. If the effective mean free path length is taken instead, the effective Knudsen number is obtained and can be expressed as (Wan, et al., 1999):

$$Kn^* = \frac{Pr_s}{\rho_s v_s r_p} \frac{k_m}{c_{p,m}} \qquad (2\text{-}38)$$

where Pr is the Prandtl number, ρ is the density and v is the mean molecular speed. The subscript s means that these variables must be taken at the powder particle surface temperature. The * indicates that the effective Knudsen number is taken rather than the Knudsen number. However, in (Chen, 1999) (Chen & Pfender, 1983) the average conductivity and heat capacity are taken. Furthermore, in (Chen, 1999) the following expression is considered to be better:

$$Kn^* = \frac{Pr_s}{\rho_s v_s r_p} \frac{k_{av}}{c_{p,av}} \frac{1+\sqrt{T_g/T_s}}{2} \qquad (2\text{-}39)$$

The mean molecular speed v_s can be expressed as (Wan, et al., 1999):

$$v_s = \left(\frac{8RT_s}{\pi M}\right)^{0.5} \qquad (2\text{-}40)$$

where R is the constant of perfect gases (8.314 J K^{-1} mol^{-1}), M the average molecular mass of the plasma, and T$_s$ the powder particle surface temperature. For argon, M = 39.948 g. mol^{-1}, and for 95%Ar/5%H$_2$ M = 38.051 g. mol^{-1}.

When the Knudsen number is not negligible (Kn > 0.001), it will become a parameter in the expressions of the heat flux and drag force (Chen & Pfender, 1983). The mean free paths of molecules in an atmospheric pressure thermal plasma is in the order of 1 to 10 μm (Chen &

Pfender, 1983). This means that powder particles smaller than 1 mm are likely to experience the Knudsen effect.

For Knudsen numbers such as 0.001 < Kn < 0.8, the Knudsen effect f_{Kn} can be expressed by (Wan, et al., 1999) (Lee, et al., 1985) (Chen, 1999) (Chen & Pfender, 1983):

$$f_{Kn} = \frac{1}{1 + \frac{2-a}{a} \cdot \frac{\gamma_s}{1+\gamma_s} \cdot \frac{4}{Pr_s} \cdot Kn^*} \qquad (2\text{-}41)$$

where a is the thermal accommodation factor with a recommended value of 0.8 (Wan, et al., 1999) (Chen, 1999), γ the specific heat ratio. The specific heat ratio is equal to 5/3 = 1.67 for a monoatomic perfect gas and 7/5 = 1.4 for a diatomic perfect gas. For pure argon, a value of 5/3 will be selected. For an Ar/H$_2$ mixture of ratio 1:4, the specific heat ratio was estimated at 1.411 (Chen & Pfender, 1983). For a ratio of 1:20 (95%Ar/5%H$_2$) a linear interpolation is made and a value of 1.61 will be selected.

With this and with the previous corrective factor accounting for varying plasma properties in the boundary layer, the convective heat transfer from the plasma to any powder particle can be evaluated.

2.3.1.4 Radiation

An order of magnitude of the radiation heat transfer can be calculated and compared to the convection with the reasoning below.

The plasma arc is assumed to be optically thick. As explained in section 2)a)i), to the plasma temperature, when multiplied by the solid angle 4π and the elementary volume dV, the plasma net emission coefficient (NEC) for a given plasma temperature and radius expresses how much net radiation power a given elementary volume dV in the center of the plasma is emitting beyond a sphere of said radius.

If a powder particle cross-section is included in the surface of that sphere of radius r, then the amount of net radiation emitted at the location of the powder particle will be the solid angle of the cone linking that particle and the emitting plasma elementary volume multiplied by the NEC:

$$dQ_R = \epsilon_T(r)d\theta dV \qquad (2\text{-}42)$$

With

$$d\theta = \frac{\pi r_p^2}{r^2} \qquad (2\text{-}43)$$

being the solid angle (r_p is the powder particle radius) (Cf. Figure 2-5).
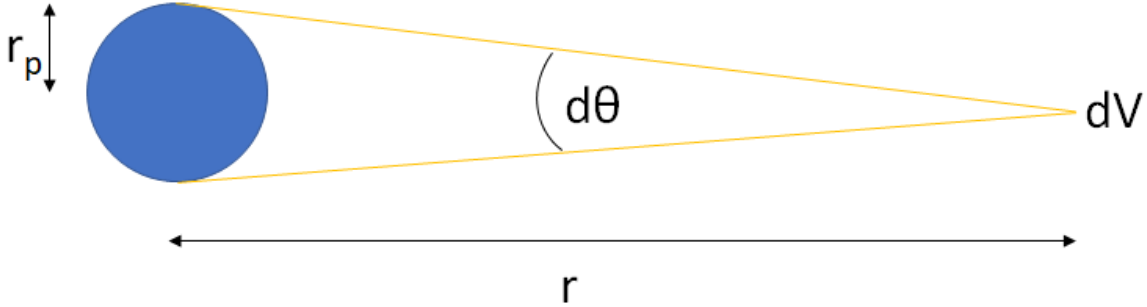
Figure 2-5: Radiation emitted by an infinitesimal plasma volume towards a powder particle

Assuming that a sphere of radius r around the powder particle is small enough to be contained in the plasma arc, the radiation emitted by the surface of that sphere (with thickness dr) towards the particle will be:

$$dQ_R = 4\pi r^2 dr \frac{\pi r_p^2}{r^2} \epsilon_T(r) \qquad (2\text{-}44)$$

When considering a powder particle in the central axis of the plasma arc, which receives the highest amount of radiation, the total radiation emitted at its location is the sum of the contributions of all the sphere surfaces around it:

$$Q_{R\,received} = \int_0^{r_a} 4\pi^2 r_p^2 \epsilon_T(r)dr \qquad (2\text{-}45)$$

Integrating $\epsilon_T(r)$ is not a simple task as very little data is available on the values of this function. From (Menart & Malik, 2002), it is known that for Argon at 14 000K,

$$\begin{cases} \epsilon_T(0mm) \approx 7W.mm^{-3}.st^{-1} \\ \epsilon_T(1mm) \approx 0.65W.mm^{-3}.st^{-1} \\ \epsilon_T(2mm) \approx 0.23W.mm^{-3}.st^{-1} \end{cases}$$

From excel an approximative correlation is proposed (using mm units):

$$ln(\epsilon_T) \approx -1.7078r + 1.7229 \qquad\qquad (2\text{-}46)$$

(This correlation over-estimates the NEC).

By using this correlation, the integration can be made analytically for a powder particle of 90µm diameter:

$$Q_{R\,received} = \frac{4\pi^2 r_p^2}{1.7078} e^{1.7229}(1 - e^{-1.7078r_a}) \approx 0.25W \qquad\qquad (2\text{-}47)$$

Since the analysis was made for a powder particle at the center of the plasma arc, and since the NEC was overestimated by the correlation, it is deduced that at all times a powder particle of 90µm diameter bathed in a 14 000K Argon plasma of 2mm radius should receive less than 0.25W of radiation power from the arc.

This is the power of all radiation lines going through the powder particle cross-section. Among them, only a fraction will be absorbed by the particle. This fraction will depend on the size of the particle, and its composition.

In comparison, calculations of the coefficient of heat transfer for convection to the powder particle from the same plasma returns values in the order of 10^4 W.m^{-2}.K^{-1} during the simulations, which is converted to a particle heating power in the order of 10W.

In conclusion, there are quantitative elements showing that the radiation power from a 14000K argon plasma going through the cross-section of a powder particle of 90µm diameter should be less than about 2-3% of that of the convective heat transfer. Among that radiation power, only a fraction is absorbed by the powder particle. The smaller the particle, the smaller the proportion of absorbed radiation should be.

In this work where 90µm a diameter constitutes the average particle size, radiation heat transfer from the plasma to the particle will be neglected. For larger particle sizes (>150 µm), it is possible that the radiation contribution may not be negligible since not only the proportion of absorbed radiation, but also the amount of received radiation would be increasing.

In the literature, radiation heat transfer from the plasma to the particle is also often neglected, especially for high enthalpy (such as Ar/H_2) or high temperature plasmas (>10 000K), and for reasonably small particles (unclear threshold).

The radiation emitted by the particle is even more negligible. It may be expressed by the Stefan-Boltzmann Law:

$$q_{R,part} = \epsilon \sigma_{SB} T_p^4 \qquad (2\text{-}48)$$

where ϵ is the emissivity, σ_{SB} the Stefan-Boltzmann constant ($5.67*10^{-8}$ W.m^{-2}.K^{-4}), and T_p the particle temperature. Even if the emissivity was 1 (black body radiation), and if the 90μm diameter particle temperature was 2000K, the result would be $q_{R,part} \approx 0.014W$ which is negligible.

2.3.1.5 Internal conduction

Finally, the internal conduction within the powder particle may be considered as well.

In that regard, the Biot number for a powder particle indicates a ratio between convection and conduction. A low Biot number (<0.1) means that the conduction inside the particle is fast enough to equilibrate the temperature while it is heated by convection. The temperature can then be considered uniform. The Biot number is expressed as:

$$Bi = \frac{h d_p}{k} \qquad (2\text{-}49)$$

During simulations, the Biot number is consistently found to be well below 0.1 for all the powder particles considered. Comparison of the results for particles simulated without the assumption of a uniform temperature and for particles with this assumption also confirms that their temperature can be considered uniform.

2.3.1.6 Conclusion

To conclude this section, in what follows, it will be considered that only convective heat transfer from the plasma to the particle is significant and that it may be expressed in the Newton Law form:

$$Q_c = 4\pi r_p^2 . h(T_g - T_p) \tag{2-50}$$

The coefficient of heat transfer h will be evaluated as:

$$h = \frac{Nu.k_{av}}{d_p} \tag{2-51}$$

And the Nusselt number is computed as:

$$Nu = Nu_{prop}.f_{Kn}.f_v \tag{2-52}$$

(but evaporation is neglected so $f_v = 1$)

The Nusselt number accounting for varying plasma properties in the boundary layer is calculated using Chen's correlation:

$$Nu_{prop} = 2[1 + 0.63Re_g Pr_g^{0.8} \left(\frac{Pr_s}{Pr_g}\right)^{0.42} (f_{prop})^{0.52}C^2]^{0.5} \tag{2-53}$$

$$C = (1 - \left(\frac{h_s}{h_g}\right)^{1.14})/(1 - \left(\frac{h_s}{h_g}\right)^2) \tag{2-54}$$

The Knudsen effect is expressed through Equations (2-38) to (2-41).

The Law of Evolution of the powder particle temperature is deduced from the first principle of Thermodynamic:

$$dH = \delta Q \tag{2-55}$$

which is rewritten as:

$$\rho \frac{4}{3}\pi r_p^3 c_p dT = 4\pi r_p^2 h(T_g - T_p)dt \tag{2-56}$$

since only convection is considered significant.
Then,

$$\frac{dT}{dt} = \frac{3}{r_p}\frac{h}{\rho c_p}(T_g - T_p) \tag{2-57}$$

2.3.2 Drag of the powder

In this subsection the forces applied on the spherical powder particle in Figure 2-4 are evaluated in order to deduce the evolution of its velocity.

2.3.2.1 Forces applied on the powder particle

The forces applied on the powder particle include the drag force exerted by the plasma, the pressure gradient and gravity. Most of the driving forces, can be neglected compared to the viscous drag force for a powder particle under 100 μm diameter (Wan, et al., 1999).

The drag force exerted by the plasma on the spherical powder particle can be expressed by:

$$F_d = \frac{1}{2} C_D \rho_g S |v_g - v_p|^2 \qquad (2\text{-}58)$$

with S being the cross-sectional area of the particle powder ($S = \pi r_p^2$).

The drag coefficient C_D typically depends on the fluid Reynolds number.

For a non-spherical particle (sphericity lower than one), it is expected that the drag force would be higher as the correlation proposed in (Song, et al., 2017) between a Newtonian fluid Reynolds number and the drag coefficient shows.

2.3.2.2 General expressions for the drag coefficient

Different expressions for drag coefficient C_D have been suggested in the literature depending on the Reynolds number characterizing the powder particle boundary layer.

For $Re_m < 0.2$, the drag coefficient can be taken as:

(Boulos & Gauvin, 1974; Vardelle, et al., 1983; Fiszdon, 1979; Doucet & Flour, 1996; Yoshida & Akashi, 1977; Bobzin & Öte, 2017)

$$C_D = \frac{24}{Re_m} \qquad (2\text{-}59)$$

The correlation for $0.2 < Re_m < 2$ is typically reported as :

(Boulos & Gauvin, 1974; Vardelle, et al., 1983; Doucet & Flour, 1996; Yoshida & Akashi, 1977)

$$C_D = \frac{24}{Re_m}\left(1 + \frac{3Re_m}{16}\right) \qquad (2\text{-}60)$$

But other suggestions were also made

$$C_D = \frac{24}{Re_m}(1 + 0.1Re_m^{0.99}) \text{ } \text{ } \qquad (2\text{-}61)$$

(Lewis & Gauvin, 1973; Bobzin & Öte, 2017)

$$C_D = \frac{27}{Re_m^{0.84}} \qquad (2\text{-}62)$$

(Yoshida & Akashi, 1977)

The expression for $2 < Re_m < 20$ is typically given as
(Ettouil, 2008; Boulos & Gauvin, 1974; Vardelle, et al., 1983; Lewis & Gauvin, 1973; Delluc, et al., 2005; Doucet & Flour, 1996; Bobzin & Öte, 2017)

$$C_d = \frac{24}{Re_m} + 0.11 Re_m^{0.81} \qquad (2\text{-}63)$$

Another correlation was given for $0.4 < Re_m < 10$ (Xibao & Hua, 1998):

$$C_D = \frac{16.6}{Re_g^{0.75}} + 0.2 \qquad (2\text{-}64)$$

For the range $20 < Re_m < 200$, the drag coefficient may be expressed as
(Boulos & Gauvin, 1974; Vardelle, et al., 1983; Lewis & Gauvin, 1973; Doucet & Flour, 1996; Bobzin & Öte, 2017)

$$C_d = \frac{24}{Re_m} + 0.189 Re_m^{0.632} \qquad (2\text{-}65)$$

Other correlations have been reported, such as:

For $Re_m < 100$:

$$C_D = \frac{24}{Re_m} + \frac{6}{1 + \sqrt{Re_m}} + 0.4 \qquad (2\text{-}66)$$

(Wan, et al., 1999; Pfender & Lee, 1985)

For $2 < Re_m < 500$:

$$C_D = \frac{18.5}{Re_m^{0.6}} \qquad (2\text{-}67)$$

(Fiszdon, 1979)

For $Re_m > 500$

$$C_D = 0.44 \qquad (2\text{-}68)$$

(Fiszdon, 1979; Bobzin & Öte, 2017)

These alternative expressions result in approximately the same C_D values.

2.3.2.3 Correction factors

The presence of steep temperature gradients in the boundary layer surrounding the particle means that the plasma properties such as density and viscosity also vary drastically across this layer. Just like for the heat transfer coefficient, many authors account for this phenomenon by introducing a semi-empirical corrective factor for the drag coefficient. The particle still may experience some non-continuum effect if the mean free path of the plasma particles in the boundary layer is of the same order of magnitude as the size of the powder particle. Authors in the literature also use a corrective factor accounting for this phenomenon, the Knudsen effect.

Correction factors for the drag coefficient due to extreme temperature and property gradients in the vicinity of the particle surface and non-continuum effects can be applied so that an effective drag coefficient can be deduced:
(Wan, et al., 1999) (Pfender & Lee, 1985) (Delluc, et al., 2005) (Ettouil, 2008) (Chen, 1999)

$$C_{D,eff} = C_D \cdot f_{vp,d} \cdot (f_{Kn})^{0.45} \qquad (2\text{-}69)$$

In Equation (2-69), the Knudsen effect corrective factor f_{Kn} is the same as for the heat transfer coefficient case (Equations (2-38) to (2-41)).

Different expressions for the corrective factor due to property gradients have been suggested and used in the literature. It is fair to say that the literature has not yet reached a common agreement mostly due to lack of experimental data.

The correlation of Lewis and Gauvin (Lewis & Gauvin, 1973) is one of the most reported correlations:
(Boulos & Gauvin, 1974; Lewis & Gauvin, 1973; Ettouil, 2008; Doucet & Flour, 1996)

$$f_{vp,d} = \left(\frac{\eta_f}{\eta_g}\right)^{0.15} \qquad (2\text{-}70)$$

But in (Pfender & Lee, 1985), the correlation of Lewis and Gauvin is reported as:

$$f_{vp,d} = \frac{\rho_g}{\rho_f}\left(\frac{\eta_f}{\eta_g}\right)^{0.15} \qquad (2\text{-}71)$$

46

It seems that it is a typographic error as in their numerical applications, the authors seem to have used the formula (2-70).

In (Yoshida & Akashi, 1977), the correlation of Lewis and Gauvin is used but ρ_g is replaced with ρ_f in Equation (2-58) as noted in (Doucet & Flour, 1996), which is equivalent from using the following corrective factor:

$$f_{vp,d} = \frac{\rho_f}{\rho_g}\left(\frac{\eta_f}{\eta_g}\right)^{0.15} \tag{2-72}$$

The correlation of Lee and Pfender is also often mentioned in the literature:
(Wan, et al., 1999; Pfender & Lee, 1985; Doucet & Flour, 1996)

$$f_{vp,d} = \left(f_{prop}\right)^{-0.45} \tag{2-73}$$

In (Delluc, et al., 2005) the correlation of Lee and Pfender was reported as:

$$f_{vp,d} = \left(f_{prop}\right)^{0.45} \tag{2-74}$$

Which seems to be a typographic error as the evaluation made in the next subsection will show.

In (Ettouil, 2008), the correlation of "Lee and al." was reported as:

$$f_{vp,d} = \left(f_{prop}\right)^{0.15} \tag{2-75}$$

Where f_{prop} is defined in Equation (2-33).

Finally, in (Vardelle, et al., 1983) no correction factor is used but instead the properties of the plasma (density and viscosity) are integrally averaged between the particle surface temperature and the plasma gas temperature, as noted in (Doucet & Flour, 1996). Then instead of evaluating the Reynolds number around the particle by taking the plasma properties at a median temperature between the plasma and the particle surface, the temperature averaged properties are used:

$$Re_{av} = \frac{\rho_{av}(V_g - v_p)d_p}{\mu_{av}} \tag{2-76}$$

Finally, ρ_g is replaced with ρ_{av} in Equation (2-58). The same method was also used in (Bobzin & Öte, 2017).

2.3.2.4 Evaluation of the proposed correction factors

There is a lot of inconsistency in the literature in the reported corrective factor for the varying plasma properties in the boundary layer around the particle. In (Chen, et al., 1991), the authors underline that the correlation suggested by Lewis and Gauvin was obtained under experimental conditions where the gas temperature was under 1000K and in an argon (10% Ar) air mixture at ~20m/s velocity or lower (which is typically not mentioned by authors using this correlation). Those conditions are very different from those used in this work, so similar to the heat transfer coefficient case it seems unlikely that the correlation of Lewis and Gauvin could be applied in this work. The correlation of Lee and Pfender was based on computational data for a small particle exposed to an argon plasma flow (Chen, et al., 1991). Their work has not been directly accessed so no more information is known about it.

In (Chen, et al., 1991), the large discrepancy between the values resulting from the different correlations from the literature was also noted. As a consequence, an experimental study was conducted where a measurement was made of the drag force exerted on a spherical particle by a thermal argon plasma whose axial temperature and velocity were also measured (Chen, et al., 1991). From Equation (2-58), an experimental drag coefficient for different sets of plasma temperatures and velocities was then deduced. It was eventually concluded that none of the proposed corrective factors in the literature are in good agreement with the experimental data obtained in this work, and that more research efforts are needed in this topic (Chen, et al., 1991). In (Paik, et al., 1993), the authors compare the experimental results of (Chen, et al., 1991) with their own predictions under the same operating conditions.

The experimental results in (Chen, et al., 1991) and computational results in (Paik, et al., 1993) are compared in Table 2-4 and Table 2-5 with the predictions obtained using the corrective factors of Lewis and Gauvin, of Lee and Pfender, and by averaging the plasma properties. The drag coefficients are reported for a set of plasma temperatures and free flow Reynolds number. In both tables, the third column labeled with (1) represents Chen's experimental results (Chen, et al., 1991) and the 4th labeled with (2) represents the predictions from computational studies (Paik, et al., 1993). The column with C_{D0} corresponds to the uncorrected drag coefficient. The columns (LG1), (LG2) and (LG3) represent the corrected drag coefficient made with the

correlations (2-70), (2-71) and (2-72) respectively (LG for Lewis and Gauvin), and the columns (LP1), (LP2) and (LP3) represent the corrected drag coefficient made with the correlations (2-73), (2-74) and (2-75) respectively (LP for Lee and Pfender). In Table 2-4 the formulae (2-70) to (2-75) are used with integrally averaged properties while in Table 2-5 median temperature properties are used. In the last column labelled (V), no correction factor is applied but every property, including the density in Equation (2-58), is taken at the boundary layer median and integrally averaged temperature dependent properties in Table 2-4 and Table 2-5 respectively (V for Vardelle).

Table 2-4: Drag coefficient values for each correlation suggested (median temperature)

Plasma Temperature (K)	Plasma Reynolds Number	C_D (1)	C_D (2)	C_{D0}	C_D (LG1)	C_D (LG2)	C_D (LG3)	C_D (LP1)	C_D (LP2)	C_D (LP3)	C_D (V)
9994	20.4	$1.76^{+0.05}_{-0.18}$	1.79	1.35	1.15	0.59	2.24	2.07	0.88	1.17	2.64
10228	22.5	$1.61^{+0.08}_{-0.05}$	1.67	1.29	1.10	0.56	2.14	1.99	0.84	1.12	2.52
10472	25.1	$1.60^{+0.08}_{-0.05}$	1.56	1.22	1.04	0.53	2.04	1.90	0.78	1.05	2.41
10797	28.2	$1.42^{+0.08}_{-0.05}$	1.45	1.15	0.98	0.49	1.96	1.83	0.73	0.99	2.31
10830	30.7	$1.36^{+0.14}_{-0.15}$	1.40	1.10	0.94	0.47	1.88	1.75	0.69	0.95	2.21

Table 2-5: Drag coefficient values for each correlation suggested (average temperature)

Plasma Temperature (K)	Plasma Reynolds Number	C_D (1)	C_D (2)	C_{D0}	C_D (LG1)	C_D (LG2)	C_D (LG3)	C_D (LP1)	C_D (LP2)	C_D (LP3)	C_D (V)
9994	20.4	$1.76^{+0.05}_{-0.18}$	1.79	1.02	0.79	0.25	2.57	1.55	0.66	0.88	3.28
10228	22.5	$1.61^{+0.08}_{-0.05}$	1.67	0.97	0.76	0.23	2.47	1.49	0.63	0.84	3.16
10472	25.1	$1.60^{+0.08}_{-0.05}$	1.56	0.92	0.72	0.22	2.37	1.43	0.59	0.79	3.04
10797	28.2	$1.42^{+0.08}_{-0.05}$	1.45	0.87	0.68	0.20	2.28	1.38	0.55	0.74	2.93
10830	30.7	$1.36^{+0.14}_{-0.15}$	1.40	0.83	0.65	0.19	2.19	1.32	0.52	0.71	2.81

From Table 2-4 and Table 2-5 it can be seen that the computational study results from (Paik, et al., 1993) (column C_D (2)) match well the experimental results from (Chen, et al., 1991) (column C_D (1)). The correlation that fit the best to these results is that of Lee and Pfender (Column LP1),

taken with all plasma properties being averaged from the wall temperature to free flow temperature as in Table 2-5 (instead of taking it at median temperature as in Table 2-4). The density in Equation (2-58) remains that of the plasma gas (not evaluated at boundary layer temperature). The predictions using this correlation tend to be about 10% lower than the experimental results. A sensitivity analysis will be performed in subsequent work to evaluated the impact of a 10% error for the drag coefficient on the final velocity results.

2.3.2.5 Effective plasma velocity

Regardless of which expression is used for the effective drag coefficient, a precise evaluation of the Reynolds number in the powder particle boundary layer is critical. Therefore, the plasma velocity observed on average in the locations where the powder flows must be selected carefully.

In that regard, the average powder particle was first assumed to penetrate through the entire radius of the LTE zone of the plasma arc before reaching the anode. So, one may want to select the median or average plasma velocity to represent the flow around the particle in a one-dimensional model.

The median value of the fluid velocity between the centerline and the edge of the plasma arc is

$$v_a\left(\frac{r_p}{2}\right) = \frac{\sqrt{3}}{2} v_a(0) \qquad (2\text{-}77)$$

The average velocity is defined by

$$v_m = \frac{1}{r_p} \int_0^{r_p} v_a(r) dr \qquad (2\text{-}78)$$

This expression can be rewritten as:

$$\frac{1}{r_p} \int_0^{r_p} v_a(0) \sqrt{1 - \left(\frac{r}{r_p}\right)^2} \, dr = \frac{v_a(0)}{r_p} \int_0^{\frac{\pi}{2}} cos^2(\theta) r_p d\theta \qquad (2\text{-}79)$$

Therefore,

$$v_m = \frac{\pi}{4} v_a(0) \qquad (2\text{-}80)$$

Therefore, the median plasma velocity for the 50A argon plasma considered is predicted at 140 m/s and the average velocity at 127 m/s.

2.3.2.6 Conclusion

To conclude this section, in the simulations of a single powder particle in a plasma flow that will follow, the plasma velocity will be set constant for simplicity, at its average value.

The uncorrected drag coefficient will be considered to follow the relations:

$$C_D = \frac{24}{Re_{av}} \quad (for \ Re_{av} < 0.2) \tag{2-81}$$

$$C_D = \frac{24}{Re_{av}}\left(1 + \frac{3Re_{av}}{16}\right) \quad (for \ 0.2 < Re_{av} < 2) \tag{2-82}$$

$$C_D = \frac{24}{Re_{av}}(1 + 0.11 Re_{av}^{0.81}) \quad (for \ 2 < Re_{av} < 20) \tag{2-83}$$

$$C_D = \frac{24}{Re_{av}}(1 + 0.189 Re_{av}^{0.63}) \quad (for \ 20 < Re_{av} < 200) \tag{2-84}$$

During the simulations, Re$_{av}$ will in fact always be between 2 and 20.

The following corrective factors are applied to the coefficient:

$$C_{D,eff} = C_D.\left(f_{prop}\right)^{-0.45}.(f_{Kn})^{0.45} \tag{2-85}$$

Where f_{prop} is defined in Equation (2-33) and f_{Kn} is defined in Equation (2-41).

The Law of Evolution of the particle velocity can be deduced from:

$$F_d \approx \Sigma F = m_p \frac{dv_p}{dt} \tag{2-86}$$

which is then rewritten as:

$$\frac{1}{2}C_D \rho_g \pi r_p^2 |v_a - v_p|^2 = \rho_{p,0}\frac{4}{3}\pi r_p^3 \frac{dv_p}{dt} \tag{2-87}$$

Therefore,

$$\frac{dv_p}{dt} = \frac{3}{8}C_D \frac{1}{r_p}\frac{\rho_g}{\rho_0}|v_a - v_p|^2 \tag{2-88}$$

Calculations show that no significant counter action from the powder particles to the plasma is observed to reduce its momentum with the range of powder flow rates considered. The same is true for heat exchange. The influence of gravity has been included by adding g into the right term of Equation (2-82), but it does not make any significant difference.

2.4 Model validation

The present model allows predictions of powder velocity and temperature evolution in the PTA. These predictions are compared to a set of experimental results that consist of the tracking of powder particles flowing through the plasma using a high-speed camera (Gajbhiye, 2022). The experimental results are also used to determine some boundary conditions, such as the typical range of powder particle injection angles and initial velocities.

The experimental data contains the tracking of 14 powder particles injected in an argon plasma arc at 60A and at 100A, with a record of their successive positions and a record of their speeds as a function of time. The powder used was that of nickel-based material mixed with tungsten carbide, and the particles sizes ranged approximately from 50 to 150 μm. Based on the manufacturer data and on a sieve analysis, the median particle diameter seemed to be around 90μm. The tracked particle individual sizes were not reported. The gas used in the experiments was pure argon. The operating parameters are given in Table 2-6:

Table 2-6: Operating parameters used during the powder tracking experiments

Current	Powder flow (g/min)	Travel speed (mm/min)	Stand-off distance (mm)	Powder gas flow (slpm)	Shielding gas flow (slpm)	Plasma gas flow (slpm)	Electrode tip angle
60A & 100A	27	600	7	1.5	12	1.5	20°

It is clear from (Gajbhiye, 2022) that even among the average trajectories that are considered in the model, a range of initial velocities and injection angles must be addressed. Based on an analysis of the particle tracking images displayed in (Gajbhiye, 2022), the typical range of injection angles is selected between 48° and 58° from the horizontal plane and the range of initial velocities was between 1 and 1.5 m/s. This along with the operating parameters displayed in Table 2-6 completes the set of boundary conditions needed for the simulation.

It is also noted that in the case of a 60A argon arc, the particles crossed about 65% of the plasma arc radius on average before reaching the melt pool. This average dropped to below 50% in the case of the 100A argon arc. Therefore, instead of taking the average plasma axial velocity throughout its entire radius, only the average value seen by the particles is taken. If proportion of the plasma radius that is crossed by the average particle is x, then the average plasma velocity seen by the particle is (considering the velocity profile from Equation (2-11)):

$$v_m = \frac{1}{xr_p} \int_{(1-x)r_p}^{r_p} v_a(0) \sqrt{1 - \left(\frac{r}{r_p}\right)^2} \, dr \qquad (2\text{-}89)$$

$$v_m = \frac{v_a(0)}{4*x} \left(\pi - 2 * arcsin(1-x) - sin(2 * arcsin(1-x)) \right) \qquad (2\text{-}90)$$

For example, if x = 0.65, then $v_m \approx 0.68 v_a(0)$ instead of $\frac{\pi}{4} v_a(0) \approx 0.785 v_a(0)$ for x = 1.

Therefore, for the 60A argon arc, the effective average plasma axial velocity will be taken at 68% of the maximum/central velocity, which is evaluated at 199 m/s. The resulting effective velocity is 131 m/s.

In Figure 2-6, the prediction of the history of an average sized WC particle temperature and vertical distance travelled from the nozzle as a function of time is shown for a range of 3 injection angles and initial velocities (48°, 53° and 58°; 1 m/s, 1.25 m/s and 1.5 m/s) deduced from the average trajectories. The dotted curves represent the vertical distance of a particle from the nozzle and the full curves the particle temperature. The blue curve (upper dashed curve) corresponds to the particle with a 58° injection angle and 1.5 m/s initial velocity, the red curve (lower dashed curve) corresponds to the particle with a 48°injection angle and 1 m/s initial velocity, and the green curve (middle dashed curve) is the intermediate case (53° and initial velocity of 1.25 m/s). The origin of time is taken when each of the powder particles enter the plasma, resulting in an initial distance from the nozzle (starting point of the dotted curves) that varies depending on the injection angle for each of the 3 cases considered: respectively 3.6, 4.0 and 4.4 mm. The temperature curves are superimposed and cannot be distinguished, as the heating rate is similar for each case (isothermal plasma approximation). The nozzle to anode standoff-distance is 7 mm (black horizontal line in Figure 2-6). Therefore, when the distance travelled from the nozzle (dotted curves) intersect with the 7 mm horizontal line, the total time

spent in the plasma t_f is deduced (vertical lines), and the intersection of the vertical lines with the temperature curves correspond to the final temperature reached by each of the powder particles (T_f).
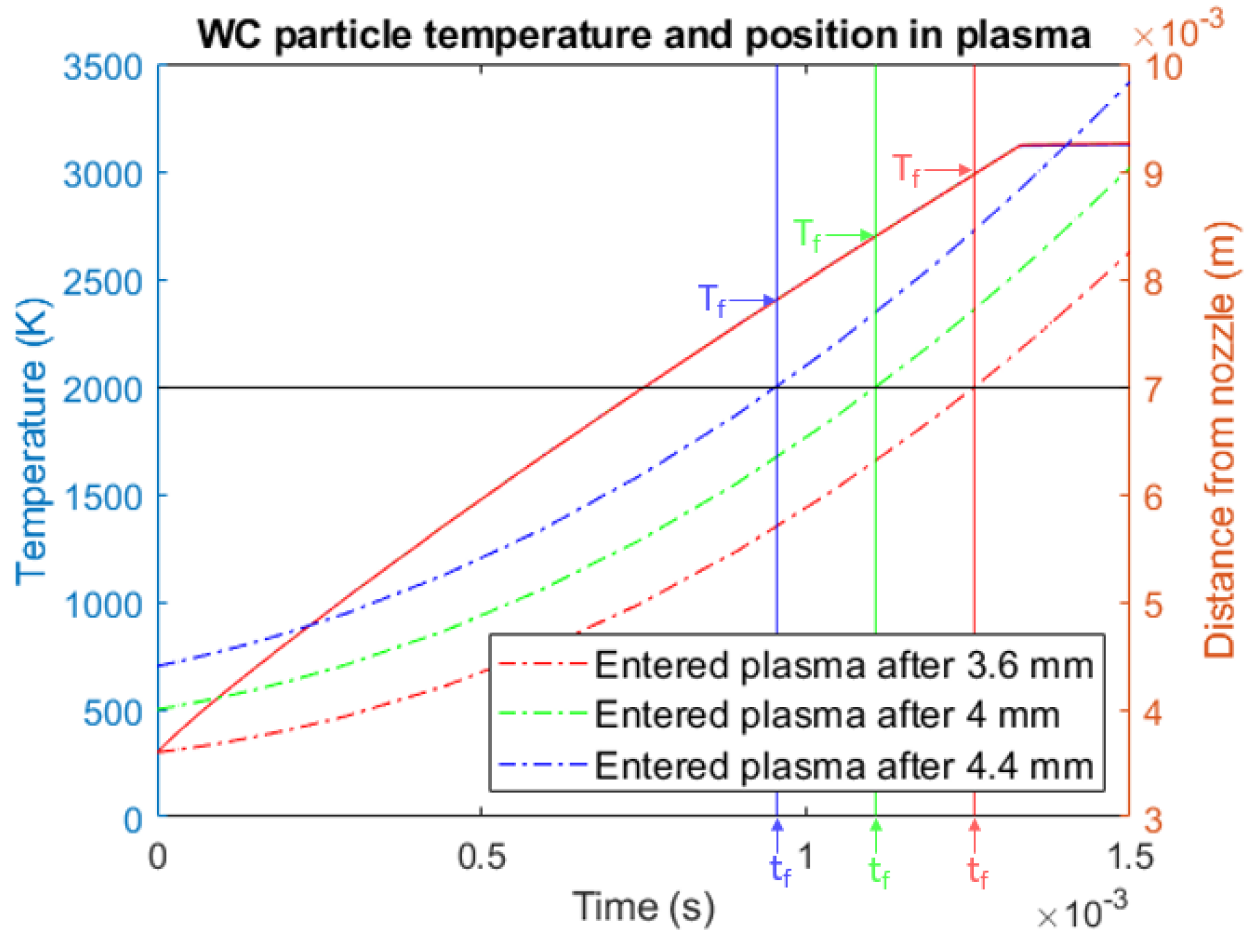
Figure 2-6: Prediction of the time evolution of the temperature and vertical distance from the nozzle of three WC powder particles of 90 μm diameter in the 7mm long 60 A argon transferred plasma arc after their injection at different angles and initial speeds from the nozzle exit

In Figure 2-6, it can be seen that for the entire range of injection angles considered, the average sized WC particle does not reach melting temperature (around 3100 K) before reaching the weld pool, and that the total time spent inside the plasma arc range between 0.9 and 1.3 ms resulting in final temperatures around 2700 K. It can also be seen from this graph that if the nozzle to anode standoff distance had been selected at 9 mm instead of 7 mm, the average sized WC powder particles (90 μm) with average trajectories would experience partial melting with a total time spent in the plasma arc of about 1.5 ms. However, it is worth noting that for an increased

standoff distance, the powder particles might cross a higher proportion of the plasma radius, resulting in an increase of the plasma average velocity (see equations (2-89) and (2-90)) and therefore slightly less time spent in the plasma and thus lower final temperatures reached by the particles, compared to the predictions shown in the graph. Therefore, one should be cautious when extending the predictions which are here valid for a 7 mm standoff distance to a wider range of distances. A 2D modeling of the trajectories might be necessary for such an extension (instead of 1D), as only experimental data for the 7 mm standoff distance is currently available to deduce the proportion of plasma radius crossed on average (x in Equation (2-89)).

The experimental results reported in (Gajbhiye, 2022) were compared to the model predictions under the same conditions. In the case of a 60A argon arc, the trajectories analyzed were the trajectories labeled 7, 8 and 9 in (Gajbhiye, 2022). The conditions characterizing these specific trajectories are summarized in Table 2-7. The comparison with the model predictions for these trajectories can be found in Table 2-8. The experimental results reported in (Gajbhiye, 2022) only included the final velocity results, which are summarized in the middle columns labeled "Exp." (Experimental) in Table 2-8, but the model predictions and the left and right side columns (labeled "Model") also included the total time spent in the arc and final temperatures reached by the powder particles upon entering the weld pool. In Table 2-8, the trajectories (7-9) were sorted based on their injection angles. The difference in their injection angles and spots of injection is what determines the distance already travelled by the powder before it enters the plasma zone.

Table 2-7: Boundary Conditions for Trajectories 7-9

Trajectories	7	8	9
Angle of injection	58°	52°	45°
Distance from the nozzle when entering the plasma	4.3 mm	3.3 mm	3.6 mm
Initial absolute velocity	1.5 m/s	1.5 m/s	1 m/s
Proportion of plasma arc radius crossed	40%	75%	60%

Unfortunately, the results reported in (Gajbhiye, 2022) did not mention the tracked particle individual sizes or their material composition. Therefore, in Table 2-8, a minimum size of 60 µm, a median size of 90 µm and a maximum size of 150 µm are considered for both the nickel-based material and the tungsten carbide material.

From Table 2-8, it can be seen that the predictions agree well with experimental results from (Gajbhiye, 2022) if the trajectories analyzed correspond to larger sized WC particles. Indeed, for each trajectory, the predictions of final velocity for a 150 μm WC particle (right side, in red) are always lower than the experimental results, whereas the predictions for a 90 μm WC particle (right side, in green) are always higher than the experimental results. However, it can be seen that the predictions of final velocity for a 150 μm NiBSi spherical particle are equal to or higher than the experimental results. Since the bigger the particle, the lower the final velocity, the model predictions exclude the possibility that the tracked particles in Trajectories 7-9 were made of NiBSi.

Unfortunately, the size and material composition of the particles tracked in (Gajbhiye, 2022) is unclear. One might assume that the particles tracked were typically the larger WC particles because they are easier to see. However, there is no proof of that claim. More experimental data is needed to completely validate the model. Nevertheless, the comparison made in Table 2-8 and the comparison that was also made for the 100A Argon case with more trajectories analyzed both seem to indicate that the model is reliable.

Table 2-8: Comparison of model predictions to experimental results for a 60A Argon Plasma

Material		NiBSi	NiBSi	NiBSi	Both	Both	Both	WC	WC	WC
Source		Model	Model	Model	Exp.	Exp.	Exp.	Model	Model	Model
Injection angle ➡	Particle size (μm) ⬇	Max (Traj. 7)	Mean (Traj. 9)	Min (Traj. 8)	Max (Traj. 7)	Mean (Traj. 9)	Min (Traj. 8)	Max (Traj. 7)	Mean (Traj. 9)	Min (Traj. 8)
Final velocity (m/s)	60	6.9	8.6	9.4	3	3.9	3.7	5.7	6.8	7.5
	90	4.9	6.0	6.6	3	3.9	3.7	3.9	4.7	5.2
	150	3.3	3.9	4.4	3	3.9	3.7	2.7	3.0	3.5
Time spent in arc (ms)	60	0.67	0.75	0.72	X	X	X	0.81	0.94	0.89
	90	0.89	1.03	0.96	X	X	X	1.1	1.3	1.2
	150	1.2	1.5	1.3	X	X	X	1.4	1.8	1.6
Final Temperature (K)	60	2240	2480	2400	X	X	X	3140 (52% liq.)	3140 (88% liq.)	3140 (82% liq.)
	90	1620	1850	1770	X	X	X	2560	3030	2860
	150	1130	1300 (50% liq.)	1270	X	X	X	1590	2010	1840

2.5 Main results

In order to obtain exploitable results, the model is now used to predict the final temperature of an average sized (90 µm) NiBSi and WC particle respectively, assuming that these particles are experiencing an average trajectory in the 50A argon plasma arc. The characteristics of what is considered to be an average trajectory for such an arc are summarized in Table 2-9 based on the remarks of the previous section on the work of (Gajbhiye, 2022) with a 60A argon arc. Besides the current, the other operational parameters are set to be the same as in (Gajbhiye, 2022) (Cf. Table 2-6).

Table 2-9: Characteristics of an average trajectory in a 50A argon plasma arc

Angle of injection (°)	Initial absolute velocity (m/s)	Initial vertical velocity (m/s)	Initial distance from the nozzle (mm)	Proportion of plasma arc radius crossed (%)
53	1.2	1.0	4	65

The final temperature reached by the NiBSi particle is obtained to be about 1590K on average, and about 2540K for the WC particle on average.

When a powder mixture containing several materials is used (which is always the case in PTA-AM of FGMs), the first law of thermodynamics may be used to average the final temperature reached by each powder particle. If two powder particles 1 and 2 of different compositions and reaching different final temperatures equilibrate with each other, their final temperature T_f can be calculated as expressed in (2-91), with x being the weight proportion of the first powder particle.

$$T_f = \frac{x c_{p,1} T_1 + (1-x) c_{p,2} T_2}{x c_{p,1} + (1-x) c_{p,2}} \qquad (2\text{-}91)$$

In Equation (2-91), T_i is the temperature reached by the powder particle i, and c_p is its average heat capacity from temperature T_i to T_f. Using Equation (2-91), Table 2-10 is deduced from the simulation results for a 50 A plasma. The operating conditions used are those displayed in Table 2-6 with a particle size of 90µm injected at 1.25 m/s at an average injection angle (53°) in such a way that it fell 4 mm below the nozzle before entering the plasma zone.

Table 2-10: Powder mixtures average final temperature in the 50A argon plasma

Material Comp. (wt%)	100% Ni 0% WC	90% Ni 10% WC	80% Ni 20% WC	70% Ni 30% WC	60% Ni 40% WC	50% Ni 50% WC	40% Ni 60% WC
50A Ar. Init. Temp. (K)	1590	1620	1670	1720	1770	1840	1920

For predicting the initial layer temperature of any composition intermediate between those calculated in Table 2-10, one may simply use a linear interpolation.

2.6 Arc-anode heat transfer

This section describes the physics of the heat transfer occurring from the plasma arc to the anode substrate.

The power delivered directly from the arc to the anode can be decomposed as follows (Cobine & Burger, 1955; Metcalfe & Quigley, 1975; Choo, et al., 1990):

$$Q_a = Q_e + Q_{cv} + Q_R \qquad (2\text{-}92)$$

Where:

- Q_e is the power delivered by electronically from the arc to the anode
- Q_{cv} is the power delivered by convection from the arc to the anode
- Q_R is the power delivered by radiation from the arc to the anode

The three next subsections describe how each of these terms is evaluated.

2.6.1 Electronic Contribution

The power delivered by the electrons can be decomposed as

$$Q_e = IV_e \qquad (2\text{-}93)$$

where I is the current and V_e is the voltage associated with this electronic contribution.

This voltage can be decomposed as follows (Lee & Na, 1996; Metcalfe & Quigley, 1975):

$$V_e = V_{anode,fall} + \Phi + V_{th} \qquad (2\text{-}94)$$

Where:

- $V_{anode,fall}$ is the anode fall voltage
- V_{th} is the voltage due to the Thomson effect
- Φ is the work function

Work function

The work function corresponds to the potential energy given up by an electron when it enters the anode. The voltage is typically around 4.2V, but can range between approximately 4.0 and 4.5V for iron and most metals, depending on other constituents (Lee & Na, 1996; Metcalfe & Quigley, 1975; Quigley, et al., 1973).

Thomson effect

In between the plasma arc core and the anode, there is a thermal boundary layer that has a thickness ranging between 0.1 and 0.5mm (Dinulescu & Pfender, 1980) and in which the condition of Local Thermodynamic Equilibrium (LTE) is no longer respected: while the heavy particles temperature gradually decreases to match that of the anode, the electrons temperature decreases by a few thousand degrees but remain close to that of the plasma arc core (~10 000K) (Dinulescu & Pfender, 1980; Choo, et al., 1990; Sanders & Pfender, 1984; McKelliget & Szekely, 1986). When the electrons reach the anode, they transfer their kinetic energy to the anode as a form of thermal energy: a phenomenon known as the Thomson effect. The potential associated with the Thomson effect can be expressed as (Quigley, et al., 1973):

$$V_{th} = \frac{3}{2}\frac{k_B(T_{e,a}-T_a)}{e} \qquad (2\text{-}95)$$

Where:

- e is the electron electric charge ($-1.602*10^{-19}$ C)
- k_B is the Boltzmann constant ($1.38*10^{-23}$ J/K)
- $T_{e,a}$ is the electron temperature near the anode and T_a is the anode temperature

Anode fall voltage

The anode fall region corresponds to the transition zone where a sharp temperature reduction results in considerably lower thermal ionization and therefore insufficient ion generation to maintain neutrality (Quigley, et al., 1973). The excess negative charge is responsible for the voltage drop at the anode (Quigley, et al., 1973). If some vaporization occurs at the anode surface, thus providing a new source of positives ions with low ionization potential, the anode fall voltage will be reduced (Lee & Na, 1996; Quigley, et al., 1973). In this work, it is assumed that the amount of metal vaporization is negligible at the anode.

With this assumption, the electric potential associated with the Thomson effect and the anode fall voltage combined together can be derived as (Metcalfe & Quigley, 1975; Choo, et al., 1990; Dinulescu & Pfender, 1980; Goodarzi & al., 1997; Choo, et al., 1992; Sanders & Pfender, 1984; McKelliget & Szekely, 1986):

$$V_{th} + V_{anode,fall} = \left(\frac{5}{2}+\frac{e\phi}{k_B\sigma}\right)\frac{k_BT_{e,a}}{e} \qquad (2\text{-}96)$$

where σ is the plasma electrical conductivity and ϕ is the electron thermal diffusion coefficient.

It was shown (Dinulescu & Pfender, 1980) that for an electron temperature around or exceeding 10 000K in the anode boundary layer in an argon plasma, this contribution can be taken as:

$$V_{th}+V_{anode,fall} \simeq \frac{\left(\frac{5}{2}+0.7\right)*k_B T_{e,a}}{e} \qquad (2\text{-}97)$$

The electron temperature at the vicinity of the anode $T_{e,a}$ is not known in this work but is estimated at around 10 000K for the anode current densities considered, and could range from 8000K to 12000K (Choo, et al., 1990; Dinulescu & Pfender, 1980; Sanders & Pfender, 1984). Therefore, the voltage associated with the Thomson effect and the anode fall voltage can be taken at (Choo, et al., 1990; Lee & Na, 1976; McKelliget & Szekely, 1986):

$$V_{th}+V_{anode,fall} \simeq 2.75V \qquad (2\text{-}98)$$

To conclude this study, the following values are selected in this work:

$$\begin{cases} V_{th} + V_{anode,fall} = 2.75V \\ \quad\; \Phi = 4.15V \end{cases} \qquad (2\text{-}99)$$

Considering the uncertainty of the anode electron temperature, the sum $V_{th} + V_{anode,fall}$ could range between 2.2V and 3.3V, although selected at 2.75V for 10000K. Similarly, the work function is not exactly known and could range between 4 and 4.5V.

The voltage associated with electronic heat transfer is:

$$V_e = 6.9V \qquad (2\text{-}100)$$

Although selected at 6.9V, this voltage could range between 6.2V and 7.8V.

With a voltage of 6.9V, the electronic power delivered to the anode Q_e is therefore equal to $6.9 * I$ W where I is the current delivered. For a 50A arc, this would be 345W.

2.6.2 Convective Contribution

2.6.2.1 Generalities

The convective heat transfer depends on whether the flow on the anode is an impinging jet (high currents/ short standoff-distance), in which case the jet is in the cathode jet dominated mode, or if the flow has weakened by the time it reaches the anode (anode jet dominated mode), in which case the convective heat transfer is negligible (McKelliget & Szekely, 1986). A cathode jet dominated mode leads to a diffuse anode attachment mode in which the plasma flows outward after it reaches the anode, while the anode jet dominated mode corresponds to a case where the plasma arc is constricted near the anode due to the relatively higher influence of the Lorentz forces, with a cold gas flowing inward and upward, generating an anode flow towards the cathode (McKelliget & Szekely, 1986; Zhu & al, 2019). The flow from the cathode then impinges with that of the anode to generate a stagnation layer away from the anode, changing the shape of the arc (Sanders, et al., 1982). The plasma gas flow rate also impacts the anode attachment mode, as higher plasma flow rates generate a diffuse arc root while lower rates generate a constricted arc, which can be seen visually (Amakawa & al, 1998; Hartmann & Heberlein, 2001). In the diffuse mode, increasing the plasma flow rate increases the power transferred to the anode due to steeper axial temperature gradients of both heavy particles and electrons and higher electron temperature at the anode's surface (Amakawa & al, 1998), while increasing the current also increases the convective heat transfer to the anode (Sanders & Pfender, 1984). Increasing the current also shifts the stagnation point towards the anode (Amakawa & al, 1998; Sanders, et al., 1982).

Conductive heat transfer, which is the heat transfer that would occur if the fluid was static, can be included in the convective term in derivations from the literature. In this work, the flow is assumed to be in cathode jet dominated/diffusive mode (which is confirmed experimentally by visual observation of the plasma jet). In what follows, all the displayed convective heat transfer derivations are applicable for the diffuse anode attachment mode.

2.6.2.2 General expressions for the convective heat transfer

The first general expression for the convective heat transfer from a plasma originates from the work of Fay and Riddell in 1958, who were studying the heat flux in the stagnation point in front of a satellite re-entering atmosphere at an extreme velocity, turning the surrounding ambient air into a plasma (Dresvin & Amouroux, 2007). The general expression for the body entering the atmosphere at a hypersonic speed was (Dresvin & Amouroux, 2007; Rosenhow, et al., 1973):

$$q_{cv} = \frac{Nu_s}{\sqrt{Re_s}} \sqrt{\rho_s \mu_s \frac{dv}{dx} \frac{\Delta h}{Pr_s}} \qquad (2\text{-}101)$$

where the subscript s refers to conditions adjacent to the boundary layer across which heat and mass transfers occur - at the body surface temperature, v is the gas longitudinal velocity relative to the body, x is the longitudinal direction, Δh is the plasma gas enthalpy difference between its temperature and the body surface temperature, ρ is the density, μ the dynamic viscosity, Nu the Nusselt number, Re the Reynolds number and Pr the Prandtl number.

The ratio $\frac{1}{Pr_s} \frac{Nu_s}{\sqrt{Re_s}}$ was then estimated at[1] (Dresvin & Amouroux, 2007; Rosenhow, et al., 1973):

$$\frac{1}{Pr_s} \frac{Nu_s}{\sqrt{Re_s}} = \frac{0.76}{Pr_s^{0.6}} \left(\frac{\mu_g \rho_g}{\mu_s \rho_s}\right)^{0.4} \qquad (2\text{-}102)$$

Which then gives:

$$q_{cv} = \frac{0.76}{Pr_s^{0.6}} \left(\frac{\mu_p \rho_g}{\mu_s \rho_s}\right)^{0.4} \sqrt{\rho_s \mu_s \frac{dv}{dx}} \Delta H \qquad (2\text{-}103)$$

However, the most commonly used formula for plasma arc convective heat transfer in the literature is a modified version of (2-103) (McKelliget & Szekely, 1986; Choo, et al., 1992; Lee & Na, 1996; Choo, et al., 1990; Goodarzi & al., 1997):

$$q_{cv} = \frac{0.515}{Pr_s} \left(\frac{\mu_g \rho_g}{\mu_s \rho_s}\right)^{0.11} \left(\mu_s \rho_s \frac{dv_r}{dr}\right)^{0.5} (h_g - h_s) \qquad (2\text{-}104)$$

In which v_r is the radial velocity.

---

[1] in (Rosenhow, et al., 1973), the constant 0.76 was given at 0.767 and the exponent 0.4 at 0.43.

Equation (2-104) will therefore be selected for the convective heat transfer derivations, since this expression seems to have a stronger theoretical background as was discussed in this subsection and because this derivation is widely used in the literature.

However, it was noted that another evaluation of the heat transfer by convection was given for an arc impinging on the weld pool surface on a flat plate and deflecting away from the stagnation point radially (valid for the diffusive attachment mode), which was only found in (Metcalfe & Quigley, 1975):

$$Q_{cv} = A * k * 0.76 * Re^{0.5} Pr^{0.33} \frac{\delta H}{c_p D} \qquad (2\text{-}105)$$

where A is the impingement area and D the arc diameter, k is the plasma thermal conductivity, c_p the plasma heat capacity, Re the Reynold number, Pr the Prandtl number and δH the plasma enthalpy difference between its core temperature and the weld pool temperature. The properties, and the Reynold and Prandtl numbers must be taken at a temperature T_m at which the plasma enthalpy is intermediate between its core temperature enthalpy and the weld pool temperature enthalpy. The authors assumed that the area of impingement had a diameter twice as large as the arc diameter. They also state that the constant 0.76 has an uncertainty of 40% due to the dramatic radial variation of the heat transfer coefficient. Due to the approximation level associated with this correlation and the fact that the previous correlation (Equation (2-104)) seems to have more theoretical background, Equation (2-105) was not used in this work.

2.6.2.3 Hydrodynamic boundary layer

In order to apply Equation (2-104), one must evaluate the $\frac{\partial v_r}{\partial r}$ term.

The radial flow v_r needs to be evaluated at the top of the hydrodynamic boundary layer between the flowing plasma and the anode (Dresvin & Amouroux, 2007), which is assumed to be a plate for simplicity. By definition, viscosity effects operate in that layer so that the fluid velocity decreases from the free flow velocity v_r to 0 at the wall.

An estimation of the orders of magnitude of the viscous force balancing by the inertial force in the boundary layer gives a rough estimate of the boundary layer thickness (Dresvin & Amouroux, 2007):

$$\delta \backsim \frac{d}{\sqrt{Re}} \qquad (2\text{-}106)$$

where d is the characteristic body dimension along the flow direction and $Re = \frac{\rho v d}{\mu}$ the Reynolds number. Due to the nozzle collimation of the arc and the diffuse anode attachment hypothesis, it is assumed that the perceived body dimension is that of the diameter of the arc. This implies that taking the previous estimation of the argon plasma arc Reynolds number which was around 100 at 50A, and the characteristic body dimension at the plasma diameter (4mm), the formula gives the following estimate: $\delta \backsim 0.4mm$.

The thickness of the thermal boundary layer may not necessary match with that of the dynamic boundary layer and a rough approximation is given by (Dresvin & Amouroux, 2007):

$$\delta_T \backsim \frac{k_g}{h} \qquad (2\text{-}107)$$

where k_g is the plasma gas thermal conductivity taken at its temperature, and h is the coefficient of convective heat transfer.

Now the location where the radial gradient of velocity must be evaluated is well defined.

2.6.2.4 Radial gradient of velocity of the impinging jet

The local balance of mass and momentum in Eulerian reference can be written as:

$$\begin{cases} \dfrac{\partial \rho}{\partial t} + div(\rho \overline{v}) = 0 \quad (a) \\ \dfrac{\partial(\rho\overline{v})}{\partial t} + \overline{div}(\rho\overline{v}\otimes\overline{v}) = \overline{f_{vol}} + \overline{div}(\overline{\overline{\sigma}}) \quad (b) \end{cases} \qquad (2\text{-}108)$$

where $\overline{\overline{\sigma}}$ is the tensor representing the surface forces (viscous and pressure), and $\overline{f_{vol}}$ is the local volume force being applied (gravity and Lorentz force). In the core of the arc, the Lorentz forces far surpass gravity: $\dfrac{\rho g}{jB} = \dfrac{\rho g}{\mu_0 J^2 r_p} \approx \dfrac{1}{10^6}$ meaning that they are the driving force leading the flow, and gravity can be neglected.

By definition, the horizontal plan at which the radial velocity needs to be evaluated is assumed to be in free and stationary flow and the viscous effect are neglected (Dresvin & Amouroux, 2007). A cylinder symmetry is assumed (invariance of all variables with the angle θ) and $v_\theta(r, z) = 0$. The origin of coordinates is taken at the intersection between the top of the hydrodynamic layer and the central axis of the plasma. The entire system is approximated as being isothermal. The thickness of the thermal boundary layer δ_T will be evaluated afterwards.

 Due to the nature of the constricted plasma arc in PTA welding, it is assumed that above the hydrodynamic boundary layer, a small transition layer of thickness d_t can be distinguished where the plasma radial velocity gradually becomes negligible ($\forall z > d_t, v_r(r, z) \approx 0$) and that the vertical velocity v_z is reduced to 0 at the top of the hydrodynamic boundary layer $(v_z(r, 0) = 0)$ with a purely radial flow locally: $\overline{v} = v_r(r, \delta)\overline{e_r}$.

With the system of Equations (2-108), all the above can be summarized by stating that the partial derivatives by the time or by θ are zero and that:

$$\begin{cases} \overline{f_{vol}} = \overline{j} \wedge \overline{B} \quad (a) \\ \overline{div}(\overline{\overline{\sigma}}) = -\overline{\nabla}p \quad (b) \\ \overline{v} = v_r(r, z)\overline{e_r} + v_z(r, z)\overline{e_z} \quad (c) \\ v_z(r, 0) = 0 \quad (d) \\ v_z(r, d_t) = \sqrt{\dfrac{\mu_0}{2\rho}}\dfrac{I}{\pi}\sqrt{\dfrac{1}{r_c^2} - \dfrac{1}{r_a^2}}\sqrt{\left(1 - \left(\dfrac{r}{r_a}\right)^2\right)} \quad (e) \\ v_r(r, d_t) = 0 \quad (f) \end{cases} \qquad (2\text{-}109)$$

For simplicity, it is also assumed that the region studied is located in the LTE zone outside of the thermodynamic boundary layer, and remains isothermal.

The balance equations in (2-108) become:

$$\begin{cases} \overline{div(\rho\overline{v})} = 0 \ \ (a) \\ \overline{div(\rho\overline{v}\otimes\overline{v})} = \overline{j}\wedge\overline{B} - \overline{\nabla}p \ \ (b) \end{cases}$$
(2-110)

These equations can be rewritten into three scalar equations in polar coordinates when r > 0:

$$\begin{cases} \dfrac{1}{r}\dfrac{\partial(rv_r)}{\partial r} + \dfrac{\partial v_z}{\partial z} = 0 \ \ (a) \\ \dfrac{1}{r}\dfrac{\partial(rv_r^2)}{\partial r} + \dfrac{\partial(v_r v_z)}{\partial z} = \dfrac{-j_z B_\theta}{\rho} - \dfrac{1}{\rho}\dfrac{\partial p}{\partial r} \ \ (b) \\ \dfrac{1}{r}\dfrac{\partial(rv_r v_z)}{\partial r} + \dfrac{\partial(v_z^2)}{\partial z} = \dfrac{j_r B_\theta}{\rho} - \dfrac{1}{\rho}\dfrac{\partial p}{\partial z} \ \ (c) \end{cases}$$
(2-111)

By injecting (a) into (b) and (c), and by noting $v_r > 0$ and $-v_z > 0$ with the symbols u and w for convenience, the following system is deduced:

$$\begin{cases} \dfrac{\partial u}{\partial r} + \dfrac{u}{r} - \dfrac{\partial w}{\partial z} = 0 \ \ (a) \\ u\dfrac{\partial u}{\partial r} - w\dfrac{\partial u}{\partial z} = \dfrac{-j_z B_\theta}{\rho} - \dfrac{1}{\rho}\dfrac{\partial p}{\partial r} \ \ (b) \\ w\dfrac{\partial w}{\partial z} - u\dfrac{\partial w}{\partial r} = \dfrac{j_r B_\theta}{\rho} - \dfrac{1}{\rho}\dfrac{\partial p}{\partial z} \ \ (c) \end{cases}$$
(2-112)

The mass and momentum balance equations that would be obtained for r=0 (central axis) are exactly the same as in (2-112) except that $\dfrac{u}{r}$ in the first equation is replaced by 0.

In order to solve this system of coupled non-linear partial differential equations, either a numerical method can be applied or the system must be simplified.

Here a simplified version is considered, where the thickness d_t of the transition zone between axial and radial flow is assumed to be small enough so that the amount of radial displacement that occurs along it is not enough to significantly stretch the plasma radius, or that the plasma radius remains the same as in the rest of the arc core just before a fully radial flow is observed.

By integrating (2-112c) along the central axis of the plasma arc (z direction), and by neglecting $j_r B_\theta$, one immediately obtains the Bernoulli theorem. It follows that at the stagnation point in the central axis above the anode:

$$P(0,0) = \frac{\mu_0 I^2}{4\pi^2 r_c^2} \qquad (2\text{-}113)$$

The pressure at this central stagnation point is the same as the central pressure below the cathode tip, since in both cases the plasma velocity is 0.

Now if the transition zone thickness d_t is assumed to be very small, one may integrate (112b) between this stagnation point and the outer zone of the flow while following a purely radial direction. Since $w \approx 0$ locally, Equation (2-112b) would become:

$$\frac{\rho}{2}\frac{\partial u^2}{\partial r} = -\left(j_z B_\theta + \frac{\partial p}{\partial r}\right) \qquad (2\text{-}114)$$

Noticing that for $r < r_a$:

$$\frac{\partial(\frac{r}{2} j_z B_\theta)}{\partial r} = \frac{\partial\left(\frac{\mu_0 J^2}{4} r^2\right)}{\partial r} = j_z B_\theta \qquad (2\text{-}115)$$

Equation (2-114) is rewritten as

$$\frac{\partial\left(\frac{\rho}{2} u^2\right)}{\partial r} = -\frac{\partial \hat{p}}{\partial r} \qquad (2\text{-}116)$$

where:

$$\hat{p} = p + \frac{r}{2} j_z B_\theta \qquad (2\text{-}117)$$

The integration of (2-112b) then returns the Bernoulli theorem again, but with a modified pressure that accounts for the Lorentz forces (when $r < r_a$). When $r > r_a$, no axial electron flow is assumed and the Lorentz forces are assumed to be 0, leading to the normal Bernoulli equation starting from r_a.

The above is then summarized by the two following equations:

$$\frac{\rho}{2} u^2(r_a) + P(r_a) + \frac{\mu_0 J^2}{4} r_a^2 = \frac{\mu_0 I^2}{4\pi^2 r_c^2} \qquad (2\text{-}118)$$

$$\frac{\rho}{2} u^2(r_a) + P(r_a) = \frac{\rho}{2} u^2(r) + P(r) \quad (for\ r > r_a) \qquad (2\text{-}119)$$

Therefore, at the point where the pressure is back to atmospheric pressure,

$$\frac{\rho}{2}u^2(r_0) = \frac{\rho}{2}u^2(r_a) + P(r_a) = \frac{\mu_0 I^2}{4\pi^2}\left(\frac{1}{r_c^2} - \frac{1}{r_a^2}\right) \qquad (2\text{-}120)$$

Leading to:

$$u(r_0) = \sqrt{\frac{\mu_0}{2\rho}\frac{I}{\pi}}\sqrt{\frac{1}{r_c^2} - \frac{1}{r_a^2}} \qquad (2\text{-}121)$$

This expression of $u(r_0)$ is equal to the central axis axial flow velocity v_0.

Where exactly the flow is depressurized depends on the exact conditions of the flow and can only be deduced by solving the system (2-112) numerically.

However, based on (Metcalfe & Quigley, 1975), it may be assumed that:

$$r_0 \approx 2r_a \qquad (2\text{-}122)$$

Looking at the velocity profiles displayed in (McKelliget & Szekely, 1986; Aithal, et al., 1998; Choo, et al., 1992) which were generated from the numerical simulations of an argon arc impinging on the anode, it indeed seems like a fair approximation to consider that the radial velocity reaches its maximum at $r_0 \approx 2r_a$.

A common approximation of the radial derivative of u is (Dresvin & Amouroux, 2007; Lee & Na, 1976; Choo, et al., 1990)

$$\frac{du}{dr} = \frac{u}{r} \qquad (2\text{-}123)$$

therefore assuming a linear increase of the radial velocity.

Considering (2-121) to (2-123), it may then be assumed that

$$\frac{du}{dr} \approx \frac{\sqrt{\frac{\mu_0}{2\rho\pi}\frac{I}{\sqrt{\frac{1}{r_c^2} - \frac{1}{r_a^2}}}}}{2r_a} \qquad (2\text{-}124)$$

The numerical application for the 50A argon arc with r_a=2mm then returns $\frac{du}{dr} \approx 40400\ s^{-1}$.

2.6.2.5 Conclusion

Using the expression (2-104) with a surface temperature of 2000K and a radial gradient of velocity $\frac{dv_r}{dr}$ of $40400\ s^{-1}\ (m.s^{-1}/m)$, one may obtain $q_{cv} = 6.77$ W.mm^{-2}.

In order to evaluate if d_t is indeed small, one may apply the law of conservation the mass:

$$d_t. 2\pi(2r_a)v_0 = \int_0^{r_a} 2\pi r v_0 \sqrt{1 - \left(\frac{r}{r_a}\right)^2}\, dr \qquad (2\text{-}125)$$

Rewriting the integral by posing $\theta = arcsin\left(\frac{r}{r_a}\right)$:

$$\int_0^{r_a} 2\pi r v_0 \sqrt{1 - \left(\frac{r}{r_a}\right)^2}\, dr = 2\pi v_0 r_a^2 \int_0^{\frac{\pi}{2}} sin(\theta)cos^2(\theta)d\theta \qquad (2\text{-}126)$$

One may find that:

$$\int_0^{\frac{\pi}{2}} sin(\theta)cos^2(\theta)d\theta = \left[\frac{-cos(\theta)}{2} + \frac{2}{3}sin(\theta)sin(2\theta) + \frac{1}{3}cos(\theta)cos(2\theta)\right]_0^{\frac{\pi}{2}} \qquad (2\text{-}127)$$

Therefore,

$$\int_0^{\frac{\pi}{2}} sin(\theta)cos^2(\theta)d\theta = \frac{1}{6} \qquad (2\text{-}128)$$

This leads to:

$$d_t. 2\pi(2r_a)v_0 = \frac{1}{3}\pi v_0 r_a^2 \qquad (2\text{-}129)$$

And then:

$$d_t = \frac{r_a}{12} \qquad (2\text{-}130)$$

This finding confirms the hypothesis that d_t was small.

It can be added that in (Jenista, et al., 1997) a numerical model for a constricted argon arc flow and heat transfer on the anode region displays the real streamlines of the plasma for both the constricted attachment and the diffuse attachment. For the diffuse mode, the convective heat flux on the anode stretches over a circle whose radius is two times that of the axial stream, giving more confidence in the (2-122) approximation. However, there is not enough information shared to compare (2-124) with their results as the axial velocity profile of their flow is not known.

Finally, using expression (2-107) for the estimation of the thickness of the thermal boundary layer and defining h as the ratio between q_c and $(T_g\text{-}T_s)$, one finds that $\delta_T \backsim 2mm$. This is larger than the hydrodynamic boundary layer thickness which was evaluated at about 0.4mm with Equation (2-106). The hypothesis of a constant density in the region where the variation of the radial flow was calculated may therefore not be true. Furthermore, it should be underlined that

71

the relation (2-104) should theoretically only be applied at the stagnation point of the flow, that is at the center of the arc just above the anode. Away from the center the amount of convective heat transfer should decrease slightly, based on the literature numerical results (Jenista, et al., 1997).

Nevertheless, the obtained value of convective heat transfer to the anode may still be used as an approximation. The accuracy of this result is unclear, and an experimental measurement of the heat transfer from the arc to the anode may be relevant to confirm this study.

2.6.3 Radiative Contribution

In numerical models, the general expression for the radiative flux received by the anode elementary surface dS_i from the plasma elementary volume element dV_j is (McKelliget & Szekely, 1986; Goodarzi & al., 1997; Choo, et al., 1990; Choo, et al., 1992):

$$dR = \frac{S_{R,j}}{4\pi r_{i,j}^2} \cos(\psi) dV_j \qquad (2\text{-}131)$$

Where $r_{i,j}$ is the distance between dS_i and dV_j, ψ is the angle between the normal of the surface dS_i and the line that connects it to dV_j, and $S_{R,j}$ is the radiation per unit volume emitted by the elementary volume dV_j. Then one can numerically integrate (2-124) over the entire plasma volume, and then then over the entire anode surface. But the form $\frac{S_{R,j}}{4\pi r_{i,j}^2}$ is for an optically thin plasma approximation. Its function will here be replaced by $\varepsilon_{T,j}$.

Instead of integrating (2-131) numerically, an attempt is made to roughly evaluate the radiation received by the anode from an elementary volume in the centerline of the arc located at a distance z and with a temperature T, $\theta(z)$ being the solid angle in from the height z:

$$\varepsilon_T(z) * \theta(z) dV \qquad (2\text{-}132)$$

Then the amount of radiation per unit volume from the centerline is:

$$rad = \frac{1}{H - z_0} \int_{z_0}^{H} \varepsilon_T(z) * \theta(z) dz \qquad (2\text{-}133)$$

Since the thermal boundary layer was estimated to have a thickness of 2mm, and since the net emission coefficient becomes negligible below 10 000K, the integration may start at z_0=1mm and end at H=7mm (arc length).

However, the function $\varepsilon_T(z)$ is not known for any plasma temperature. Since only an order of magnitude is sought, it will be assumed that it can be averaged with the value of $\varepsilon_T(2mm)$ in the integral in (2-133). Then, since $\theta(z) = \frac{\pi R^2}{z^2}$ for a circular weld pool of radius R receiving the radiation, it follows that:

$$rad \sim \frac{\pi R^2 \varepsilon_T(2mm)}{H-z_0}\left(\frac{1}{z_0} - \frac{1}{H}\right) \qquad (2\text{-}134)$$

A temperature of 13 000K will be assumed. An averaged value of ε_T ranging between 0.1 and 0.3 W.mm^{-3}.sr^{-1} seems reasonable for an argon arc. With a radius R = 2mm, one may obtain a radiation power of 0.3 to 0.4 W.mm^{-3} from the centerline. Then by integrating this result over the cylindrical plasma arc volume, the resulting power would be about 30W. This is most likely an over-estimation since the plasma edges contribute much less to the radiation power.

In conclusion, the radiative contribution most likely does not exceed 30W.

2.7 Summary

The heat input of a 50A argon transferred plasma arc with the operating parameters taken the same as in Table 2-6 (besides the current) was characterized. It was divided into a heat transfer to the injected powder particles and a heat transfer to the weld pool or anode.

A 90µm NiBSi or WC powder particle was predicted to reach a final temperature of 1590K or 2540K on average respectively. The initial weld pool temperature that would be obtained with a mix of these powders is summarized in Table 2-10.

The powder delivered directly by the arc to the anode can be subdivided into an electronic, a convective and a radiative contribution. The electronic contribution was estimated at 345W. The convective contribution was estimated at 6.77 W.mm^{-2} at the center of the arc. It seems from studies in the literature that the convective heat transfer is significant over a radius twice as large as the plasma arc radius. If this value of 6.77 W.mm^{-2} is integrated over a circular surface equal to twice the plasma arc radius, this would give a convective power of 340W. Then the radiative contribution is most likely less than 30W. If a radiative power of 15W is taken, the total power resulting from each contribution is 700W. The power delivered directly by this arc to the anode is therefore estimated at roughly 700W.

Chapter 3 : The influence of the argon Plasma Transferred Arc current and hydrogen content on its heat input to powder particles and weld pool

3.1 Introduction

A simplified modeling of the transferred plasma arc was developed in Chapter 2 in order to predict the final temperature reached on average by the nickel alloy and by the tungsten carbide powder particles respectively. The arc average temperature in the region where the powder is injected as well as its velocity profile were predicted. Finally, the portion of the plasma arc power being absorbed by the anode was also estimated.

However, results were only given for a unique set of PTA-AM operating parameters, while the applicability of the model extends to a wider range. In particular, in the context of this work where the deposition of functionally graded materials is studied, one might want to vary the PTA operating parameters during the printing of the part to adapt to the varying material composition of each layer being deposited, or simply to prevent excessive heat build-up.

In Chapter 2, the arc considered was an argon plasma arc with a 50A current, which was meant for welding the WC-reinforced Ni-based alloy. Depending on the material being welded however, not only the selected current but also the plasma gas might differ. For example, in (Moghazi, et al., 2020) the 17-4PH martensitic stainless steel is welded with a mixture of Ar/5%H_2 in order to prevent oxidization, and the current used is 63A. Instead of grading the coating with WC, a material gradient where the 17-4PH steel is gradually being replaced by the MMC was also considered in this work. The model that was developed is a tool that can be used to evaluate if and under what conditions an intermediate set of operating parameters could be used for the arc to melt a powder mixture of these two materials. Therefore, in the present Chapter the predictions made in Chapter 2 are extended for different values of selected current and for both pure argon and Ar/5%H_2 mixture. A study of what would happen to 17-4PH powder particle in the arc is also included. The Ar/5%H_2 plasma mixture having higher enthalpy and thermal conductivity than the argon plasma, higher heating rates by convection will be observed.

Additionally, the sensitivity of the model on its parameters is evaluated quantitatively to assess the results accuracy.

3.2 Influence of the current and hydrogen content on the plasma arc average temperature and axial velocity

A simplified modeling of the transferred plasma arc was developed in Chapter 2 in order to evaluate its average temperature in the region where the powder is injected as well as its velocity profile. However, only the predictions for an argon plasma arc with a 50A current were given for the purpose of welding a WC-reinforced Ni-based alloy. Depending on the material being welded, the selected current or plasma gas might differ. For example, in (Moghazi, et al., 2020) the 17-4PH martensitic stainless steel is welded with a mixture of Ar/5%H_2 in order to prevent oxidization, and the current used is 63A. One might also want to vary the operating parameters slightly layer by layer to prevent excessive heat build-up. Therefore, predictions are here made for different values of selected current and for both pure argon and Ar/5%H_2 mixture.

3.2.1 Plasma Temperature

In this subsection, the average plasma temperature on the anode side is estimated for a range of selected currents with and without hydrogen.

3.2.1.1 Calculation Method

As explained in Chapter 2, the local equation for the heat balance in the stationary arc was reduced to the following simple form after making some simplifying assumptions:

$$\frac{j^2}{\sigma} - 4\pi\varepsilon_T = 0 \qquad\qquad\qquad (3\text{-}1)$$

The collimated arc was assumed to be in local thermodynamic equilibrium, homogeneous, isothermal and optically thick, and this equation was only meant to estimate the average plasma temperature in the bottom half region of the arc (anode/plate side). Despite all the simplifying assumptions, it was found by comparing the predictions made with Equation (3-1) with detailed numerical modeling of similar transferred plasma arcs that these approximations still gave reliable results. However, due to some degree of approximation concerning the values of the NEC, a range of possible plasma temperature (with a minimum and a maximum possible value) was given rather than an exact temperature. The temperature dependent properties of the argon and Ar/H_2 plasma can be found in (Boulos, et al., 1994).

In Table 3-1 and Table 3-2 are displayed the selected average plasma temperature in the bottom half of the plasma arc for the pure argon case and the Ar/5%H$_2$ case respectively. The range of possible values resulting from the NEC approximation range is also displayed (min and max values). The recommended temperature value to select was given based on an evaluation of the model's predictions tendencies as evaluated in Chapter 2.

Table 3-1: Predicted average temperature of Argon plasma at different currents

Plasma/Current	50A	57A	60A	63A	100A
Argon minimal	12 600K	12 800K	12 900K	13 000K	13 900K
Argon maximal	12 900K	13 300K	13 400K	13 500K	15 200K
Argon recommended	12 800K	13 100K	13200K	13 400K	14 800K

Table 3-2: Predicted average temperature of Ar/5%H$_2$ plasma at different currents

Plasma/Current	50A	57A	60A	63A	100A
95%Ar/5%H$_2$ min	12 100K	12 300K	12 400K	12 400K	13 400K
95%Ar/5%H$_2$ max	12 800K	13 200K	13 300K	13 400K	14 700K
95%Ar/5%H$_2$ recommended	12 400K	12 700K	12 800K	12 900K	14 000K

3.2.2 Plasma velocity

In this subsection, the plasma axial velocity is estimated for a range of selected currents with and without hydrogen.

3.2.2.1 Calculation Method

Under the assumption of an isothermal, homogeneous, incompressible and laminar stationary flow, and if the plasma gas flow rate selected does not exceed a certain threshold value, it was concluded that the axial velocity profile could be expressed in the following way (Cf. Chapter 2):

$$v_a(r) = v_a(0)\sqrt{1 - \left(\frac{r}{r_a}\right)^2} \qquad (3\text{-}2)$$

With:

$$v_a(0) = \sqrt{\frac{\mu_0}{2\rho}\frac{I}{\pi r_c}} \qquad (3\text{-}3)$$

In these formulas, r_a is the cylindrical plasma arc radius (when flowing past the nozzle exit), r_c is the plasma arc radius just under the cathode tip, r is the radial coordinate considered in cylindrical coordinates, I is the current selected, ρ is the plasma density and μ_0 is the magnetic permeability of void. The cathode tip radius r_c is expressed in the following way:

$$r_c = \sqrt{\frac{I}{\pi j_c}} \qquad (3\text{-}4)$$

where j_c is the cathodic current density which was evaluated at 100 A/mm² for the present work where a thoriated tungsten electrode with a 20° angle is used.

Consequently, the following values of r_c are deducted depending on the current (Table 3-3):

Table 3-3: Plasma arc radius under the cathode tip for different currents

Current	50A	57A	60A	63A	100A
r_c (mm)	0.399	0.426	0.437	0.448	0.564

3.2.2.2 Results

The following values of plasma velocity at the center line $v_p(0)$ are deduced for various currents in Table 3-4 considering the plasma densities corresponding to the recommended temperatures from Table 3-1 and Table 3-2:

Table 3-4: Center velocity of Ar & Ar/5%H₂ plasma at different currents

Plasma/Current	50A	57A	60A	63A	100A
Pure Argon	175 m/s	192 m/s	199 m/s	206 m/s	293 m/s
95%Ar/5%H₂	177 m/s	193 m/s	200 m/s	207 m/s	286 m/s

In Table 3-5 are displayed the median values of the fluid velocity for different currents.

Table 3-5: Median velocity of 2mm radius Ar & Ar/5%H₂ plasmas at different currents

Plasma/Current	50A	60A	100A
Pure Argon	140 m/s	158 m/s	242 m/s
95%Ar/5%H₂	142 m/s	161 m/s	248 m/s

In Table 3-6 are displayed the mean values of the fluid velocity for different currents.

Table 3-6: Average velocity of 2mm radius Ar & Ar/5%H₂ plasmas at different currents

Plasma/Current	50A	60A	100A
Pure Argon	127 m/s	143 m/s	219 m/s
95%Ar/5%H₂	129 m/s	146 m/s	225m/s

3.2.2.3 Assumptions verification

The assumptions made in Chapter 2 to obtain such results were verified *a posteriori* for an argon plasma at 50A, but will be verified again here for a wider range of operating parameters.

In particular, the assumption that the selected plasma gas flow rate does not further increase the flowing speed due to the nozzle constriction must be verified. Assuming a cylindrical shape of the arc core of radius r_a due to the collimation effect of the nozzle, and considering the conservation of mass throughout the flow, the plasma gas flow rate must be constant and is expressed by Equation (3-5):

$$\rho_0 \dot{V} = \dot{m} = \rho \pi r_a^2 V \qquad (3\text{-}5)$$

where ρ and ρ_0 are the ionized plasma arc density and the room temperature plasma gas density respectively, $\dot{V}$ is the volume flow rate (selectable operating parameter) and V the plasma arc flowing speed.

The flowing speed derived from the velocity profile expressed by Equation (3-2) is equal to (Cf. Chapter 2):

$$V = \frac{2}{3} v_a(0) \qquad (3\text{-}6)$$

The flowing speeds deduced are displayed in Table 3-7 for different currents.

Table 3-7: Flowing speed of Ar & Ar/5%H₂ plasma at different currents

Plasma/Current	50A	57A	60A	63A	100A
Pure Argon	117 m/s	128 m/s	132 m/s	137 m/s	195 m/s
95%Ar/5%H₂	118 m/s	129 m/s	133 m/s	138 m/s	190 m/s

Considering Equations (3-3), (3-5) and (3-6), it follows that:

$$\dot{m} = \sqrt{\frac{2\mu_0 j_c}{9\pi}} \sqrt{\rho I} \pi r_a^2 \qquad (3\text{-}7)$$

A appropriate room temperature volume flow rate on the PTA was empirically determined to be 1.5lpm for welding the Ni-WC alloy at 50A with argon (Rojas, 2021) and at 2lpm for welding 17-4PH at 63A with 5%H_2-95%Ar (Moghazi, et al., 2020).

In Table 3-8 is displayed a comparison of these chosen input flow rates with those calculated from Equation (3-7) for j_c = 100 A/mm^2 and various currents or plasma radii, assuming r_a = 2 mm (nozzle inner radius). The deduced r_a is also given if the mass flow rate is set instead.

Table 3-8: Plasma gas flow rate – Inputs and predictions

Gas	Input volume flow rate (lpm)	Input mass flow rate (g/s)	Calculated mass flow rate if r_a = 2mm (Equation (3-7)) (g/s)	Calculated r_a (Equation (3-7)) if mass flow rate is set (mm)
Argon at 50A	1.5	0.045	0.046	2.0
95%Ar/5%H_2 at 50A	1.5	0.042	0.046	1.9
Argon at 63A	1.5	0.045	0.049	1.9
95%Ar/5%H_2 at 63A	1.5	0.042	0.049	1.9
Argon at 50A	2	0.059	0.046	2.2
95%Ar/5%H_2 at 50A	2	0.057	0.046	2.3
Argon at 63A	2	0.059	0.049	2.2
95%Ar/5%H_2 at 63A	2	0.057	0.049	2.2

Table 3-8 shows that the empirically selected input plasma gas flow rate for welding Ni-WC with argon at 50A was 0.045 g/s, which matches well with the flow rate deduced from the previously calculated velocity profile (0.046 g/s). With such a mass flow rate, and if the same velocity profile was assumed but with a potentially different arc radius, the deduced arc radius would still be 2.0 mm.

For welding 17-4PH at 63A with 95%Ar/5%H$_2$, the empirically selected plasma flow rate was 0.057 g/s instead of 0.042 g/s if the volume flow rate had been held at 1.5 lpm. The flow rate deduced from the calculated velocity profile lies between these two values (0.049 g/s). Or it could be said that the mass flow rate deduced from this velocity profile would correspond to the input if the arc radius was 2.2mm.

Overall, with the range of plasma flow rates considered in this work (1.5 – 2 lpm), it appears that the initial assumption that the nozzle constricting the arc at a radius of 2mm should not force a significant acceleration of the plasma is consistent with the results from Table 3-8.

Finally, the assumption of a laminar flow may be verified by evaluating the Reynolds Number for each of these operating parameters. Even if the central/max velocity is used, the results displayed in Table 3-9 below show Reynolds numbers consistently below 250.

Table 3-9: Reynold numbers characterizing the plasma flow at central axis velocity

Gas/Current	50A	60A	100A
Argon	100	118	234
95%Ar/5%H$_2$	91	107	182

In conclusion, the results obtained in Table 3-4 and the profile described in equation (3-2) will be regarded as describing correctly the plasma velocity profile in the LTE zone.

3.3 Influence of the current and hydrogen content on the powder particles average final temperature

A simplified modeling of the plasma-particle interaction was built in Chapter 2. As a result, predictions were given on the average final temperature reached by a 90 µm NiBSi or WC particle after being injected in a 50A argon transferred plasma arc under certain conditions. The arc length was 7 mm, but after analysis the work of (Gajbhiye, 2022) it was found that the powder particles only entered the plasma after an average drop of 4 mm, meaning that the vertical distance traveled in the plasma was 3 mm. The exact operating conditions and boundary conditions can be found in Chapter 2. The scope of the results obtained in the previous Chapter is extended here by varying the current and by considering the case of an argon-hydrogen mixture. Furthermore, predictions are also given for an additional material, the 17-4PH stainless steel. A current up to 63A is considered because it is the current that was used in (Moghazi, et al., 2020) for 17-4PH, using a 95%Ar/5%H_2 gas mixture. All the properties used in the simulations are temperature dependent and can be found in the appendices.

The model results are displayed in Table 3-10 for a pure argon gas and in Table 3-11 for a 95%Ar-5%H_2 gas.

Table 3-10: Model predictions for the average particle path of a median sized (90 µm) powder particle for different powder material compositions & arc currents with pure argon plasma

Material	17-4PH	NiBSi	WC	17-4PH	NiBSi	WC	17-4PH	NiBSi	WC
Current (A)	50	50	50	57	57	57	63	63	63
Final velocity (m/s)	5.8	5.2	4.1	6.2	5.6	4.4	6.6	5.9	4.6
Time spent in the arc (ms)	0.89	0.98	1.2	0.84	0.92	1.1	0.80	0.88	1.1
Final temperature (K)	1670	1590	2540	1680	1640	2650	1690	1700	2740

Table 3-11: Model predictions for the average particle path of a median sized powder particle depending on the powder material compositions & arc currents with 95%Ar/5%H₂ plasma

Material	17-4PH	NiBSi	WC	17-4PH	NiBSi	WC	17-4PH	NiBSi	WC
Current (A)	50	50	50	57	57	57	63	63	63
Final velocity (m/s)	5.7	5.1	4.1	6.1	5.5	4.4	6.4	5.7	4.6
Time spent in the arc (ms)	0.91	0.99	1.2	0.86	0.94	1.2	0.82	0.90	1.1
Final temperature (K)	1720	1840	2910	1740	1900	3024	1800	1930	3090

From Table 3-10, it can be seen that with the 50 A argon gas used for NiBSi and WC (Rojas, 2021), the average 90 μm 17-4PH particle is expected to reach only solidus temperature but would not be fully melted even as the current increases (calculated melting range between 1666 and 1727 K with Thermocalc). However, from Table 3-11 it can be seen that with the 95%Ar/5%H₂ gas used in (Moghazi, et al., 2020) at 63A for 17-4PH, the average 90 μm 17-4PH is expected to be fully melted starting from 57A. This difference is essentially due to the higher thermal conductivity of this plasma. It can also be noted that the other materials are also elevated to a higher temperature with 95%Ar/5%H₂ compared to pure argon, at any current. In particular, the average 90 μm WC particle almost reaches melting temperature (3120-3143 K) at 63A. It follows that smaller WC particles (60-70 μm), or average sized WC particles (90 μm) with a smaller injection angle (40-50°) are likely to experience partial or complete melting under these conditions. Therefore, it could be said that the model predicts that if the same operating parameters are kept, choosing a 95%Ar/5%H₂ plasma gas instead of pure argon for the nickel alloy mixed with tungsten carbide would result in too much heat input to the powder (with melting of part of the WC), while choosing argon instead of 95%Ar/5%H₂ would conversely lead to an insufficient heat input to the 17-4PH (incomplete fusion).

These predictions agree with the empirical optimization of the operating parameters that were performed in (Moghazi, et al., 2020) using the Taguchi method for the 17-4PH, and in (Rojas, 2021) for the Ni-WC powders. Indeed, in these works, the current and gas composition selected

were tuned so that the injected powders would receive the right amount of heat input. The present model also concludes that the parameters selected in these works are well fitted to the respective powders that they were using.

From a functionally graded materials perspective however, it seems that there is an incompatibility between the 17-4PH powder and the MMC powder as none of the operating parameters considered in Table 3-10 and Table 3-11 were fitted to both powders. This is due to the fact that the required Ar/5%H$_2$ arc heat input to melt the 17-4PH powder particles also has the effect of melting some WC powder particles as shows the analysis of Table 3-11: even a current reduced at 50A could have this effect with this gas. The presence of hydrogen in the plasma gas is necessary to prevent 17-4PH oxidization (Moghazi, et al., 2020). Thus, in this thesis only a gradient of tungsten carbide in the nickel matrix will be considered.

3.4 Influence of the current and hydrogen content on plasma-anode heat transfer

A rough estimate of the plasma-anode heat transfer was proposed in Chapter 2 for a 50A argon transferred plasma arc. The influence of increasing the current and of adding hydrogen to the gas is now evaluated.

The following summarizes how the heat transfer from the arc to the anode was evaluated. The power delivered directly from the arc to the anode can be broken down as follows (Cobine & Burger, 1955; Metcalfe & Quigley, 1975; Choo, et al., 1990):

$$Q_a = Q_e + Q_{cv} + Q_R \qquad (3\text{-}8)$$

Where:
- Q_e is the power delivered by electronically from the arc to the anode
- Q_c is the power delivered by convection from the arc to the anode
- Q_R is the power delivered by radiation from the arc to the anode

Electronic power

The electronic power is the product of the arc current with the electronic voltage:

$$Q_e = IV_e \qquad (3\text{-}9)$$

Assuming an electron temperature of about 10 000K in the anode boundary layer for a 50A argon arc, it was previously estimated that V_e could range between 6.2V and 7.8V depending on the exact electron temperature and anode work function. The intermediate value of 6.9V was selected. Increasing the current is likely to increase V_e slightly due to higher electron temperature. Based on this remark, the following approximate values of P_e are suggested depending on the current (and regardless of the hydrogen content):

Table 3-12: Estimation of the electronic power delivered to anode depending on the current

Current (A)	50	57	63
P_e	350	400	450

Convective power

The most commonly used expression for the plasma arc convective heat transfer to the anode can be found in (McKelliget & Szekely, 1986; Choo, et al., 1992; Lee & Na, 1996; Choo, et al., 1990; Goodarzi & al., 1997):

$$Q_c = \frac{0.515}{Pr_s} \left(\frac{\mu_g \rho_g}{\mu_s \rho_s} \right)^{0.11} \left(\mu_s \rho_s \frac{dv_r}{dr} \right)^{0.5} \left(h_g - h_s \right) \qquad (3\text{-}10)$$

This expression involves the radial gradient of the radial velocity of the plasma impinging on the anode. In Chapter 2, this gradient was roughly evaluated based on to permit an estimation of the convective contribution:

$$\frac{du}{dr} \approx \frac{\sqrt{\frac{\mu_0 I}{2\rho\pi}} \sqrt{\frac{1}{r_c^2} - \frac{1}{r_a^2}}}{2r_a} \qquad (3\text{-}11)$$

Results are shown in Table 3-13 and Table 3-14 for pure argon and 95%Ar/5%H$_2$ plasma arc, for different currents. Regardless of the current or gas used, the anode surface temperature is taken at 2000K.

Table 3-13: Predictions of radial velocity gradient and anode convective heat transfer from the argon transferred plasma arc impinging on the anode, for different currents

Current (A)	50	57	63
$\dfrac{du}{dr}$ (s^{-1})	43,600	47,800	51,600
q_{cv} (W.mm^{-2})	10.0	11.9	13.7

Table 3-14: Predictions of radial velocity radial gradient and anode convective heat transfer from the 95%Ar/5%H$_2$ transferred plasma arc impinging on the anode, for different currents

Current (A)	50	57	63
$\dfrac{du}{dr}$ (s^{-1})	44,100	48,100	51,400
q_{cv} (W.mm^{-2})	12.4	14.4	16.0

Radiation power

In Chapter 2, a rough estimate of the order of magnitude of the radiation contribution was made for a 50A argon arc. The contribution was found to be most likely less than 30W for a 13 000K argon arc. From Table 3-1, it can be seen that the argon plasma arc was estimated to have an average temperature equal to or less than 13 000K on the anode side, for currents between 50A and 63A. With the same current, the net emissions received from the ArH$_2$ mixture would be the same as for argon, because the net emission coefficient would be the same (Cf. Equation (3-1)). Therefore, the same conclusion would be drawn for both gases and for currents ranging between 50A and 63A that the radiation power received by the weld pool would not exceed 30W.

Total power

Assuming that convective heat transfer is significant over a circular area whose radius is twice as large as the collimated impinging plasma arc, all the above can be summarized by the following rough estimates of the power transferred from the arc to the anode (Table 3-15 and Table 3-16).

Table 3-15: Estimations of argon arc power received by the weld pool depending on current

Current (A)	50	57	63
Q_e (W)	350	400	450
Q_c (W)	500	600	690
Q_r (W)	10	20	30
Q_{total} (W)	860	1020	1170

Table 3-16: Estimations of Ar/5%H$_2$ arc power received by the weld pool depending on current

Current (A)	50	57	63
Q_e (W)	350	400	450
Q_c (W)	620	720	800
Q_r (W)	10	20	30
Q_{total} (W)	980	1140	1280

3.5 Influence of some critical parameters on result accuracy

In Table 3-17 is presented a sensitivity analysis of the parameters that are critical for the prediction of the average final temperature of the powder particles.

These parameters are the average plasma temperature as seen by the particle, the average plasma velocity as seen by the particle, the particle injection site and initial velocity, and the estimated Nusselt number and drag coefficient.

The analysis was conducted for the three materials considered (17-4PH, Nickel-based, WC) with their respective optimal operating parameters. As shown in Table 3-17, a 5% change in plasma temperature, coupled with the corresponding change in velocity profile resulting from the change in density (see Equation (3-3)) results in a 13% change in the final particle temperature. However, by changing only the plasma velocity by 10%, the final particle temperature changes by 3%. Overall, as shown in Table 3-17, the parameters with the most impact are the plasma temperature, followed by the Nusselt number evaluation, while the parameters with the least impact are the drag coefficient and the plasma velocity evaluation.

The parameter variations considered in Table 3-17 are a pessimistic estimate of the accuracy of the estimated value of these parameters. If all the parameter variations in Table 3-17 are

combined together and assumed to be independent, the resulting variation in final particle temperature is 21.5%. The main conclusions that can be drawn from this sensitivity analysis are that the accuracy of the results will be improved primarily by improving the accuracy of the evaluation of the plasma temperature and the Nusselt number, and that the average final particle temperature predicted in this work may differ by up to 20% from the actual average. For a predicted final temperature of 1800K, for example, this means that the actual final temperature may be between 1440K and 2160K; the extreme values of this range corresponding to a pessimistic assessment of the model accuracy.

The impact of up to 20% variation in the average final particle temperature on the macro-scale thermo-mechanical simulation of the deposition process on Abaqus is to be studied with a subsequent sensitivity analysis in Chapter 4.

Table 3-17: Sensitivity Analysis for the estimation of the powder particle final temperature

Parameter	Plasma temperature (with associated velocity change)	Plasma average velocity seen by particle (unchanged temperature)	Particle Injection Site and Initial velocity	Nusselt Number	Drag coefficient
Parameter variation	±5%	±10%	±10%	±20%	±20%
Average particle final temperature variation	±13%	±3%	±5%	±15%	±6%

3.6 Summary

The impact of increasing the current and/or adding hydrogen to an argon transferred plasma arc was evaluated. The influence on the average temperature and velocity of the plasma, as well as on the average final velocity and temperature of the injected powder particles was studied. A rough estimate of the heat transfer from the arc to the weld pool was given as a function of the selected current. Finally, the sensitivity of the model on the parameters used was evaluated. It was found that the plasma temperature and the Nusselt number estimate were the most critical when predicting the average final temperature of the powder particles.

Chapter 4 : Prediction of Residual Stresses for Functionally Graded Materials deposited with Plasma Transferred Arc Additive Manufacturing

4.1 Introduction

In the previous chapters, a model was built to account for as many variables as possible in order to predict the temperature history and trajectory of the powder particles in the transferred plasma arc, and deduce the final temperature they reach upon merging with the weld pool on average. The effect of changing some operating parameters on the final powder temperature was studied. The heat input delivered from the torch to the anode was also estimated in the previous chapters, depending on the current. Inferences from this work are used here as input data to simulate the additive manufacturing of functionally graded materials at the macro scale level, as was explained in the section 4) of Chapter 1.

The thermal history followed by the thermal stress history of the process was predicted, and finally the residual stress distribution was obtained for a wall-shaped printed part. The initial temperatures of each deposited layer were set at the powder particles final temperature obtained for the corresponding WC content. Simulations were performed on Abaqus for different material gradients under the same operating conditions. In this chapter, the residual stress profiles obtained for each material gradient are compared to each other and to a wall without gradient. The effect of approximating the input variables based on the sensitivity analysis from Chapter 3 is also shown. Finally, a discussion is made and conclusions are drawn as to the material gradient that is most susceptible to improve the part wear resistance from a residual stress perspective.

4.2 General purpose

The general purpose of the present study is to estimate which material gradient in a WC-NiBSi coating is likely to result in increased abrasion and wear resistance. As stated in the introduction, the general criterion is to reduce the amount of tensile residual stresses near the coating surface. Compressive residual stresses near the surface are expected to increase the wear resistance of the coating.

The desired composition of the final layer is that of a nickel-based metal matrix composite with 60%wt of tungsten carbide. A total of N=20 layers are deposited in total. The variable to be changed as a function of layer number n will be the tungsten carbide content. As successive layers are deposited, the weight percentage of WC will be increased from 0 to 60. The set of gradation profiles considered is one that follows a power law function as described in Equation (4-1).

$$WC\ wt\% \ = \ 60.\left(\frac{n}{N}\right)^p \tag{4-1}$$

The profiles that were considered in this work are shown in Figure 4-1 with their exponent p. Increasing values of p are plotted with colors corresponding to increasing wavelengths in the light spectrum. An exponent p lower than one corresponds to a WC-rich structure, while a p exponent greater than one corresponds to a nickel-rich structure. The gradient of WC content is higher near the first layers when p is lower than one, and higher near the last layers when p is higher than one. A p value of 0 corresponds to a situation where the entire wall has 60 wt% WC (no gradient), and an infinite value corresponds to a situation where only the last layer has 60 wt% WC, but the other layers contain 0% WC. It can be seen that a p value of 0.001 is almost identical to the former case, while a p value of 100 is almost identical to the latter.

Simulation of the Additive Manufacturing of Functionally Graded Walls using the PTA was performed on Abaqus. The different gradation profiles that are considered are those in Figure 4-1, and the residual stress profiles obtained with each of these gradients are compared in the Results section.
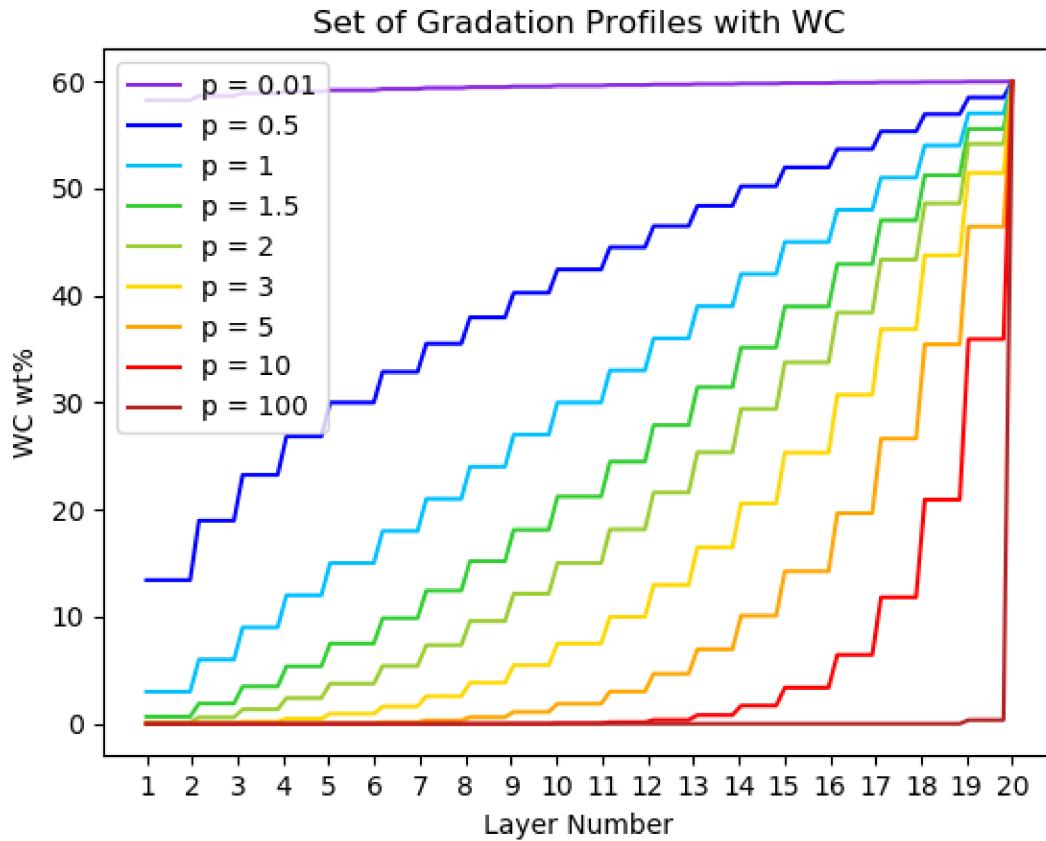
Figure 4-1: Set of tested gradation profiles

4.3 Input variables of the simulated deposition process

The Additive Manufacturing of a graded wall part using the PTA with argon gas and the following operating parameters was simulated (Table 4-1):

Table 4-1: Selected PTA-AM Operating Parameters

Current	Powder flow (g/min)	Travel speed (mm/min)	Stand-off distance (mm)	Powder gas flow (slpm)	Shielding gas flow (slpm)	Plasma gas flow (slpm)	Electrode tip angle
50A	40	480	7	1.5	10	1.5	20°

The dimensions of a weld bead consisting of 60% WC in a Ni-based matrix was measured experimentally at 2.5 mm width and 2.1 mm height.

In Abaqus, the initial temperature of each deposited layer can be prescribed as well as the path and intensity of the energy source. The Abaqus AM plug-in was used to specify these paths. These input parameters were linked to the operating parameters of the PTA-AM in Chapter 2.

Based on Chapter 2, the temperature reached by the NiBSi and tungsten carbide particles are estimated to be on average 1320°C and 2270°C respectively, resulting in the following initial bead temperatures as a function of WC content:

Table 4-2: Initial Layer Temperatures Depending on the WC Content

Material Comp. (wt%)	100% NiBSi 0% WC	90% NiBSi 10% WC	80% NiBSi 20% WC	70% NiBSi 30% WC	60% NiBSi 40% WC	50% NiBSi 50% WC	40% NiBSi 60% WC
Init. Temp. (°C)	1320	1350	1400	1450	1500	1570	1650

For any layer with a composition intermediate between those considered in Table 4-2, a linear interpolation is performed to infer its initial temperature. The power transferred by the heat source was also estimated in Chapter 2 to be about 700W. Since only half of the build part is modeled, the heat source power prescribed in Abaqus was 350W and was set to be fully absorbed by the half part. The goal was not to simulate the exact physics of heat exchange occurring in the weld pool during the deposition - such as Marangoni convection and heat source distribution, but only to capture the overall heat input from the arc with a fairly good accuracy. Air cooling was estimated to be about 30 $W.m^{-2}.K^{-1}$. A cooling time of 10 seconds was arbitrarily prescribed after the deposition of each layer to limit the heat build-up effect. The torch speed was 8 mm/s, so each bead was printed in 10s as they were 8 cm long. Thus, each section in a deposited layer had the same amount of time before the next subsequent layer was deposited. After printing, the part is slowly cooled down to room temperature (25°C) by natural air convection. The predicted residual stresses after cooling are shown in the Results section.

4.4 Description of the numerical model

In Abaqus, a thin wall consisting of 20 layers was modeled on a substrate, as shown in Figure 4-2. Only half of the substrate and wall were modeled due to symmetry. Each wall layer was modeled with a rectangular cross-section of 2.5x2.1 mm. The full dimensions of the substrate were 10x10x1cm and the length of the wall was 8 cm. Since there was 20 layers, the height of the wall was 42mm.
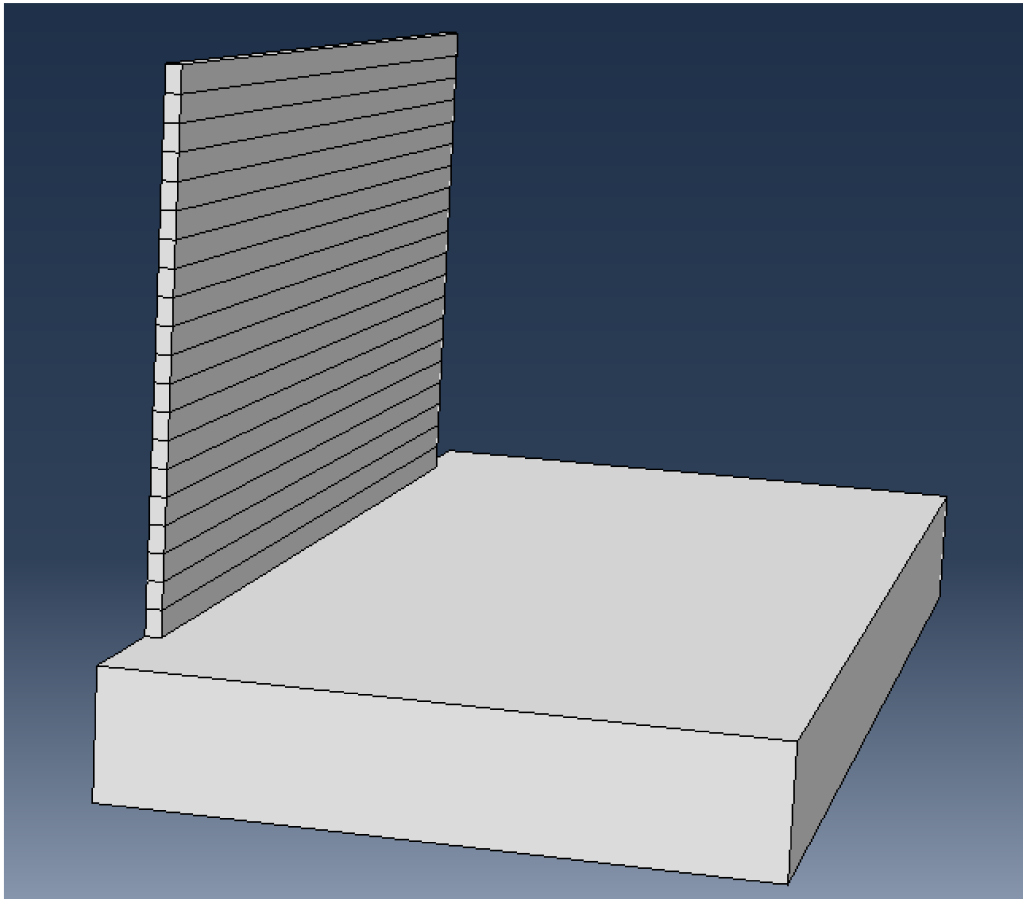

Figure 4-2: Additively Manufactured Thin Wall on Abaqus

Each layer has been assigned a specific set of temperature-dependent material properties based on WC content. More information is available in Appendix A regarding these properties. The substrate was assigned the temperature dependent properties of the 17-4PH stainless steel.

A sequentially coupled thermomechanical model was run: the temperature history was first predicted, then the thermal strains and stresses that develop during deposition were deduced.

A mechanical boundary condition was prescribed where all degrees of freedom of the substrate bottom were constrained. The residual stresses are obtained after the part has cooled.

The mesh of the entire part was defined as shown in Figure 4-3. Although no large bending is expected, especially due to the mechanical boundary condition restraining the bottom surface of the substrate, each layer was divided into 3 elements along their height to decrease shear locking. A higher number than 3 was not necessary given the precision sought in this study; dividing each layer into 5 elements instead only resulted in a relative difference of about 5% in the results. No reduced integration was made, thus avoiding hourglassing. The mesh consisted in a total of 5556 elements. An automatic time increment was prescribed. The direct method with the quasi-Newton solution technique was employed due to the significant nonlinearities of the model.
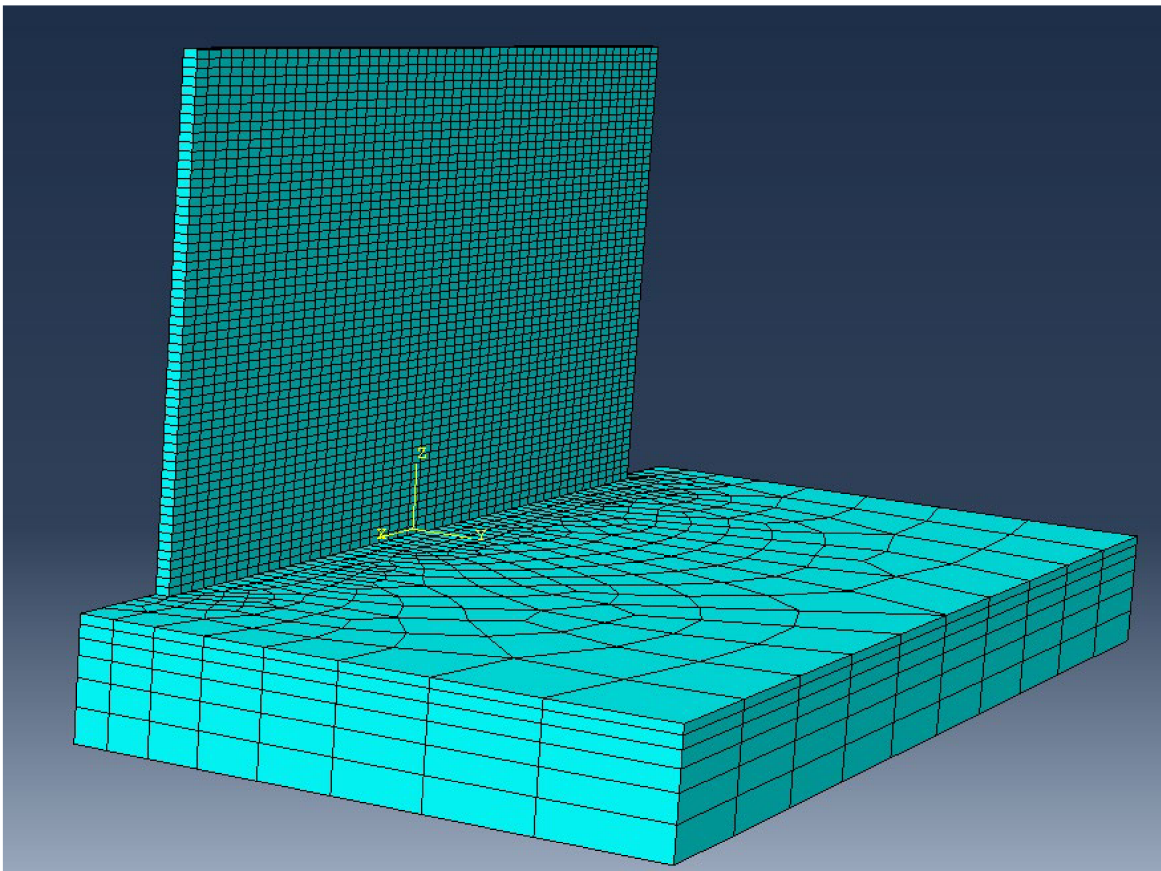

Figure 4-3: Part Meshing

Automatic stabilization was prescribed with the standard Abaqus energy dissipation parameters, but the accuracy of the results should not be significantly affected since the energy lost by all dissipation sources was less than 2% of the total system energy at the end of the simulation.

4.5 Results

Before presenting the comparison between different residual stress profiles resulting from different material gradations, the PTA-AM of an ungraded wall was simulated to get better insight into the overall advantage of using a graded profile. The ungraded wall also corresponds to the case where the gradation exponent p is equal to 0. Twenty identical layers consisting of a NiBSi-based matrix with 60 wt% WC with an initial temperature of 1650°C were progressively deposited as shown in Figure 4-4.
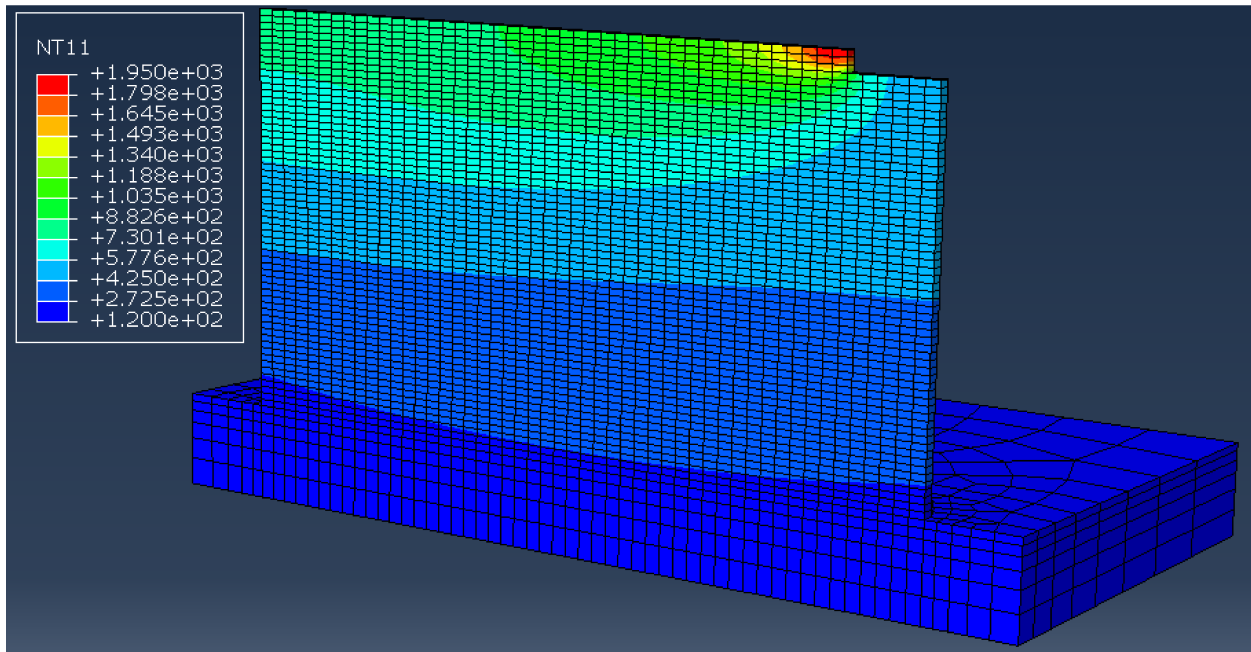

Figure 4-4: Thermal simulation of a non-graded wall – deposition of the last layer (in °C)

The additional heat input from the arc (700W), and the heat build-up resulting from the interpass temperatures increase the initial temperature of the activated elements from 1650°C to about 2000°C during the deposition of the last layers. With a cooling time of 10 seconds between each layer, during the deposition of the last layer (20th layer), the previous layer is almost completely remelted - as shown in Figure 4-5 where only the region above solidus temperature is colored - and the interpass temperature reaches 550°C. This suggests that a higher cooling time could be considered, or that the current or the torch standoff-distance could be progressively decreased layer after layer to counteract the heat build effect. In addition, the solidification time of the weld pool in the last layer ranges between 3 and 3.5s, which could adversely affect the good homogeneity of the WC particles inside the solidified bead due to their sinking while the bead is

still liquid, as analyzed in (Wolfe, 2010). An improvement of the present work could therefore consist in deducing a set of operating parameters for each deposited layer leading to a sufficiently low solidification time, depending on the cooling time between each deposited pass.
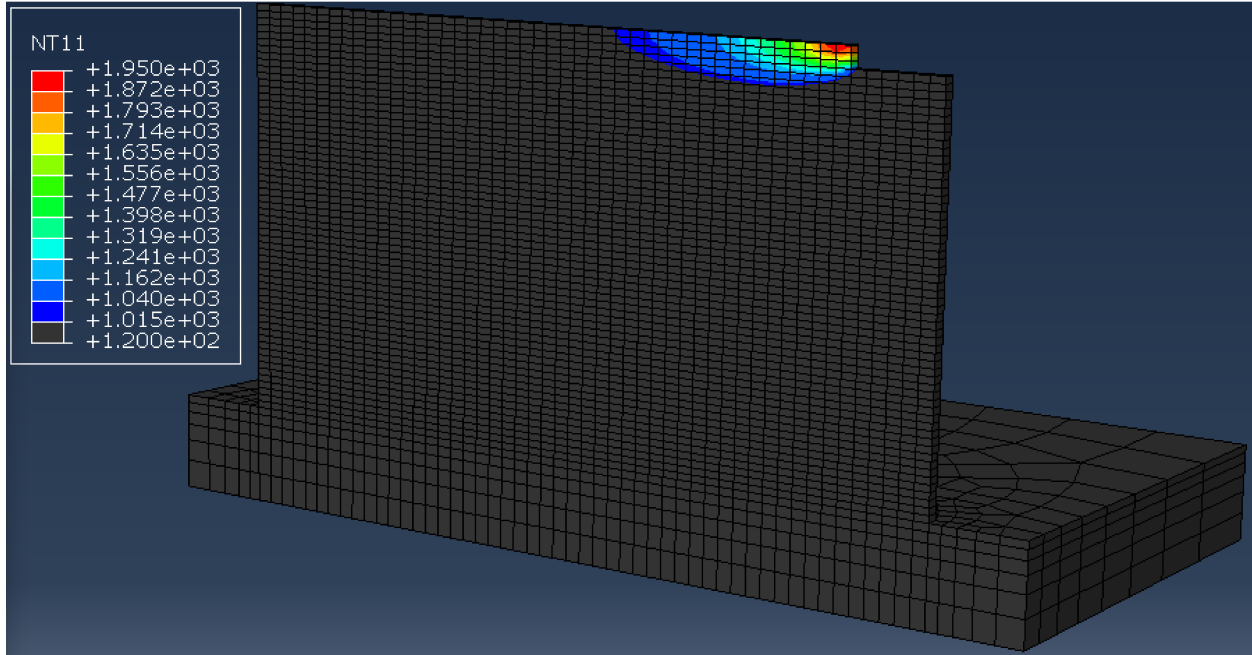

Figure 4-5: Thermal simulation of a non-graded wall – melted zone during last layer deposition (in °C)

The residual stress field inside the ungraded wall that results from the temperature history of the aforementioned deposition is shown in Figure 4-6. The longitudinal stress (S11, in the direction of the weld) is displayed because it is the most significant stress. Tensile stresses of up to 500 MPa can be observed around the last layers deposited, which are the layers assumed to be exposed to wear and abrasion. These tensile stresses are likely to be detrimental to their wear resistance. The residual stress field obtained after removal of the substrate is shown in Figure 4-7. Although the residual tensile stresses in the upper part of the wall are relieved to some extent, they remain relatively high on average and can reach 375 MPa. In addition, high tensile stresses remain in the first deposited layer. Most of the compressive stresses developed in the intermediate layers due to the subsequent shrinkage of the subsequent layers. The use of material gradation can then help shift these compressive stresses to the upper layers.

The residual stress field obtained with an ungraded wall can be compared with the residual stress field obtained with a material gradient for p = 3 for example, as shown in Figure 4-8 and Figure 4-9. It is worth noting that a higher heat buildup was observed compared to the ungraded case due to the higher amount of latent heat to be dissipated in the first layers containing more nickel-based material. Overall, it can be seen that compared to the ungraded case, the compressive residual stresses were shifted to the upper layers when the wall is still bonded to the substrate (Figure 4-8). When the substrate is removed, the tensile residual stresses throughout the wall are relieved and their maximum value is reduced by half. Some tensile stresses still remain, especially in the 18th and 19th layers due to the considerably smaller shrinkage rate of the 20th layer, but these stresses are nevertheless lower than for the ungraded wall. In addition, the residual stresses are highly compressive in the last layer. Therefore, this comparison confirms the effectiveness of using a material gradation to shift the location where compressive residual stresses develop.

It is worth noting that although the yield strength of the nickel super-alloy was approximated at about 1000 MPa (Cf. Appendix A), this high yield strength can generally be reached only after heat treatment and not for the as welded part. Furthermore, for the composite layers' properties, perfect bonding was assumed between the WC and the nickel matrix and a linear interpolation based on the WC volume fraction was made between the two materials respective yield strengths to estimate the composite yield strength. However, many factors influence the strength of the MMC. For example, the presence of tungsten carbides in the matrix increases its brittleness, generates an inhomogeneous residual stress distribution in the layer due to the coefficient of thermal expansion mismatch, and the Ni-WC interface can act as a crack initiation site under tensile loading, resulting in much lower ultimate tensile strength (Deenadayalan, et al., 2021). Therefore, it is expected that the real tensile strength of each layer is lower than what was estimated in this work and that some stress relaxation mechanisms could occur in areas where tensile residual stresses are high (such as WC debonding with the matrix). As a result, the amount of residual stresses would be lower than predicted in this work. When the local stress state goes above the yield stress, we are not modeling any deformation of the composite for stresses beyond the yield stress. For the Ultimate tensile stress, when a local stress state exceeds it, the materials should result in some local failure. This could be modeled by decoupling the nodes that experience this condition. But that crack will grow due to stress concentrations at the

crack tip. These issues require microstructural information and are beyond the scope of this work. However, the purpose of this study is to predict the residual stresses trends along the wall material gradation depending on the gradient chosen, rather than predicting the exact residual stresses. Even if the true residual stresses are lower than what is predicted here due to the material yield strength being overestimated, the trends observed for each gradation profile would remain similar.

In the following, an attempt is made to compare the value of each gradation profile considered. The longitudinal residual stresses within the wall were averaged along the welding direction and plotted against the height in Figure 4-10 and Figure 4-11 with and without the presence of the substrate restraining the wall shrinkage respectively. The residual stresses of the substrate displayed (negative height) are those in the central region of the substrate, below the wall. To differentiate the different material gradations, the same color coding as in Figure 4-1 was used. The averaged longitudinal residual stresses are displayed over the height of the wall to give a global perspective, but the region of interest is the upper region where the last layers are deposited.

For more clarity, a zoom was performed on this region ($z > 3.5$cm was arbitrarily selected) and the results for some of the selected material gradients are plotted in Figure 4-12 and Figure 4-13. It can be seen that the higher the value of p, the more compressive the residual stresses are in the last layer, which is intuitive. However, depending on the value, this may imply higher tensile stresses in the previous layers (the 18th and 19th are shown). In particular, a situation where the WC weight percentage suddenly shifts from 0 to 60 from the 19th to the 20th layer (p = 100 or more) results in the most compressive residual stresses in the last layer but also in the highest tensile stresses in the 19th layer. A smoother gradient however, may result in highly compressive stresses in the last layer while not significantly increasing the tensile stresses in the contiguous layers as the comparison between p = 0 and p = 3 shows.

To better compare these effects, the maximum and minimum residual stresses obtained near the top of the wall and averaged along the deposition direction are plotted in Figure 4-14 for different material gradations. One criterion that could be chosen in order to effectively compare each gradation profile could be the minimization of both the minimum (most negative) value of compressive stresses (blue curve in Figure 4-14) and of the maximum tensile stresses (red curve

in Figure 4-14) near the last layers. This criterion could be summarized by summing these two extreme values and plotting the results, which then gives the green curve (SUM) in Figure 4-14. With such a criterion, the minimum value of this curve would correspond to the best p value.

It can be seen that p values lower than 1 correspond to the worst-case scenario, while the sum decreases continuously with p for higher values of p until it reaches a minimum around $p = 10$, before increasing again. The exact location of the minimum is not known exactly because more values of p should be tested, especially between 10 and 100. However, it can be concluded that a good trade-off is obtained with a p value of 10 (see corresponding material gradation in Figure 4-1).

Additional improvement should be possible by relieving the tensile residual stresses at the contact with the substrate. This should be possible by increasing the heat input with which the first layer is deposited or/and by preheating the substrate. Furthermore, the cooling time between each layer, the resulting interpass temperature and possibly a decreasing heat input layer by layer is another area of study that could further improve the obtained residual stress profile.
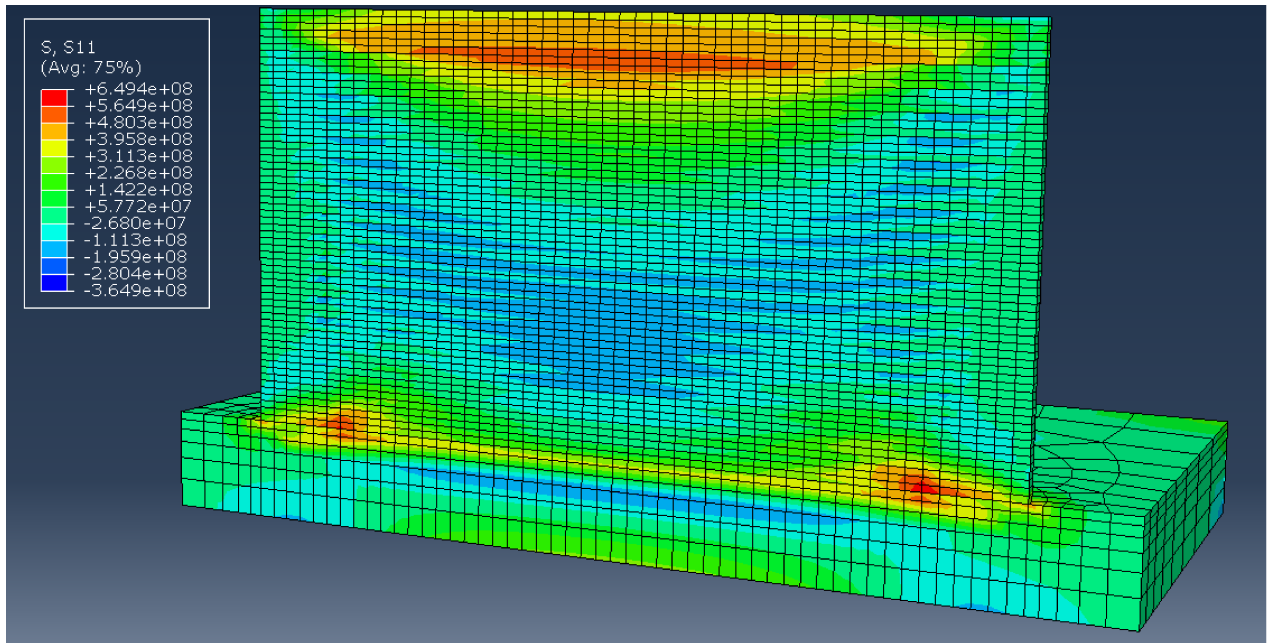
Figure 4-6: Residual stress field (in Pa) after printing of the non-graded wall

Figure 4-7: Residual stress field (in Pa) after printing of the non-graded wall (substrate removed)

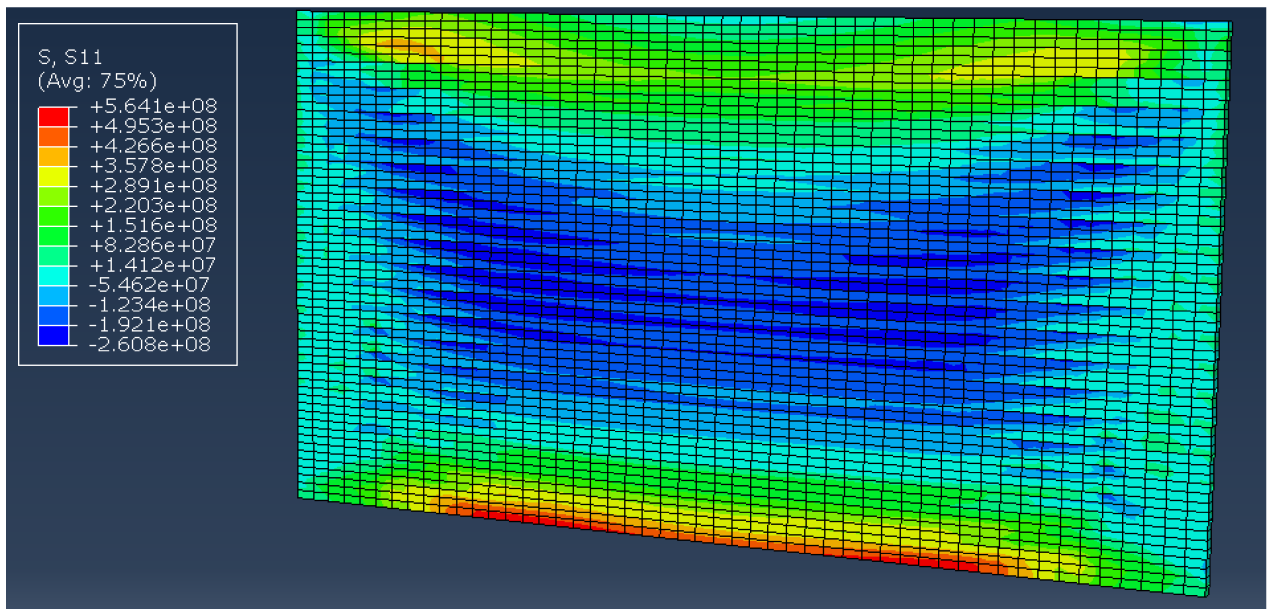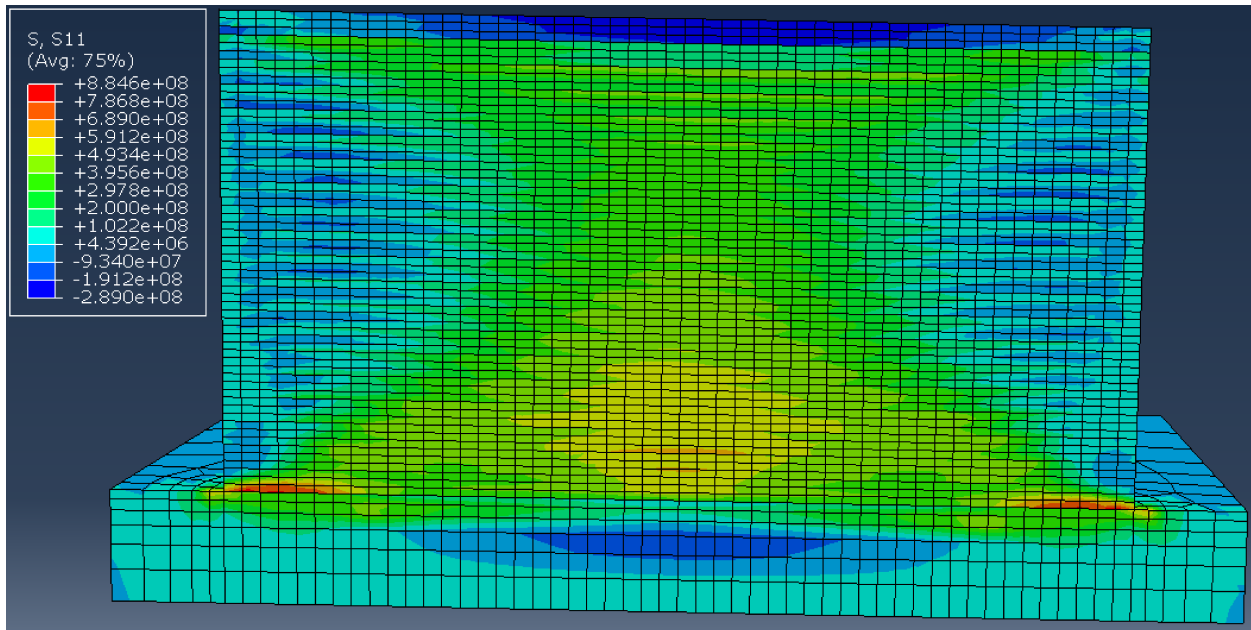*Figure 4-8: Residual stress field (in Pa) after printing of the p=3 graded wall*
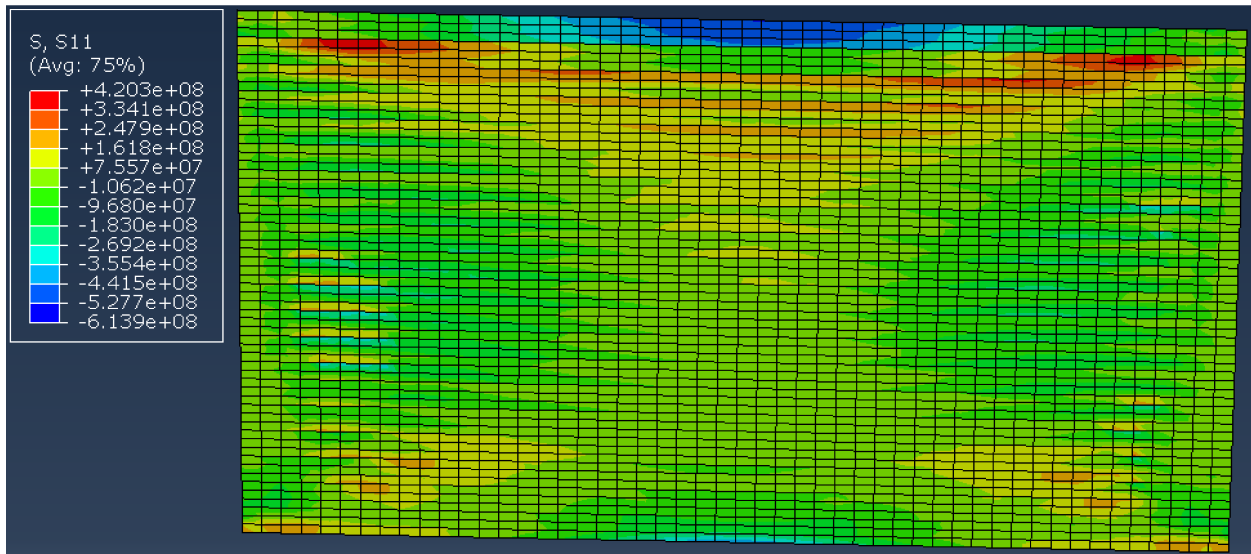
Figure 4-9: Residual stress field (in Pa) after printing of the p=3 graded wall (substrate removed)

Figure 4-10: Longitudinal residual stresses along height (with substrate)

Figure 4-11: Longitudinal residual stresses along height (substrate removed)

102

Figure 4-12: Zoom on longitudinal residual stresses along height (with substrate)
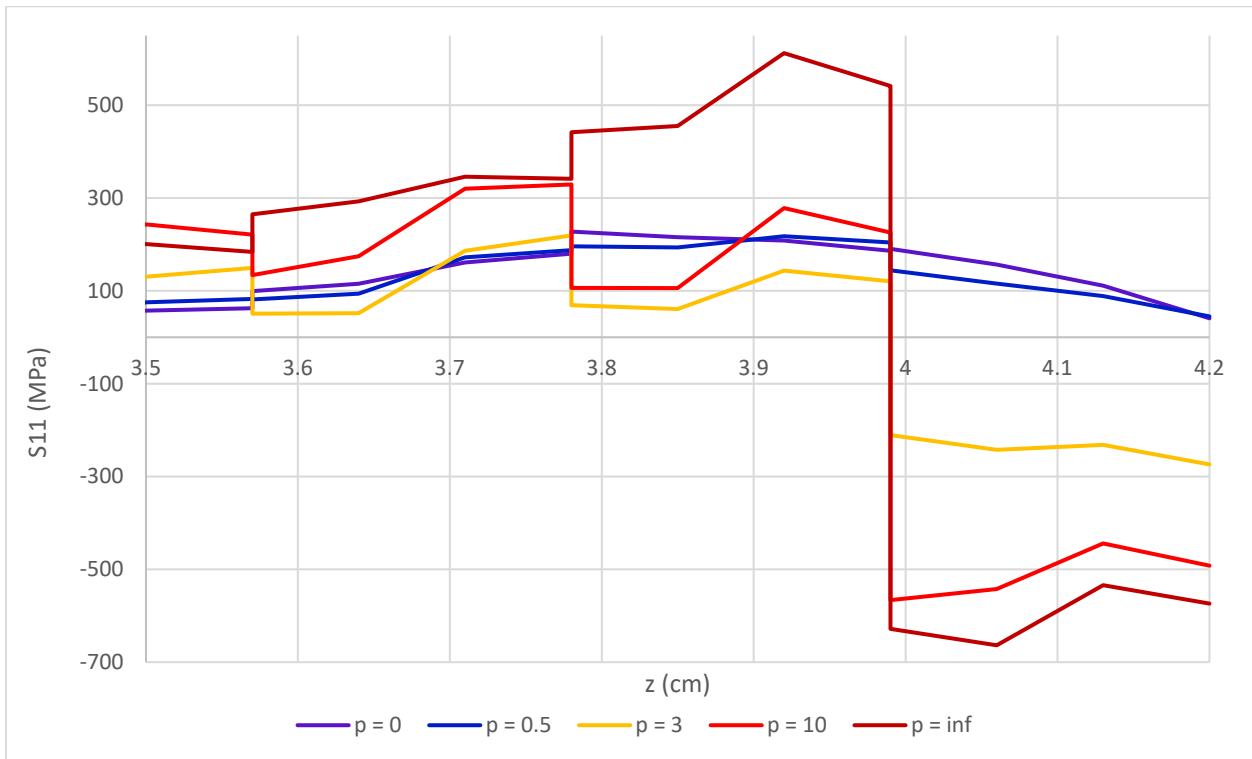
Figure 4-13: Zoom on longitudinal residual stresses along height (substrate removed)
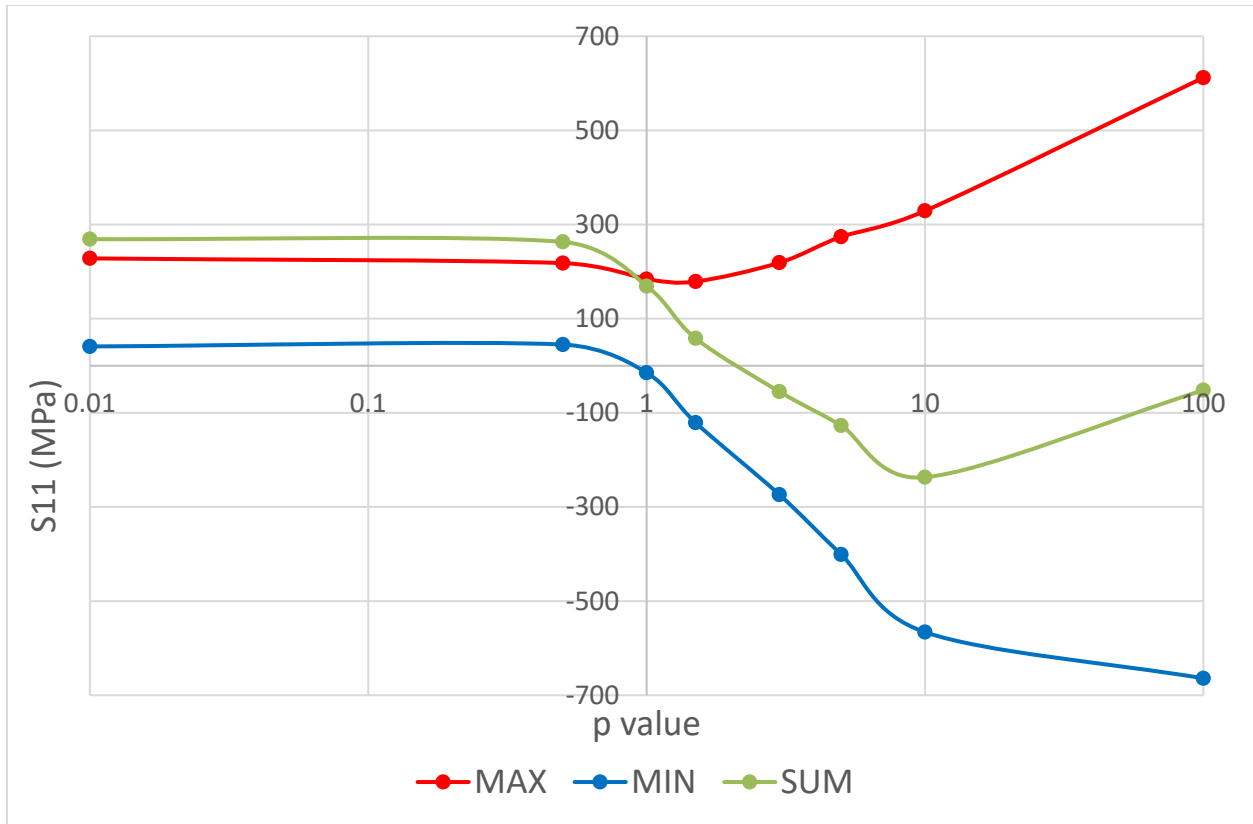
Figure 4-14: Maximum and minimum residual stresses near the wall top as a function of p

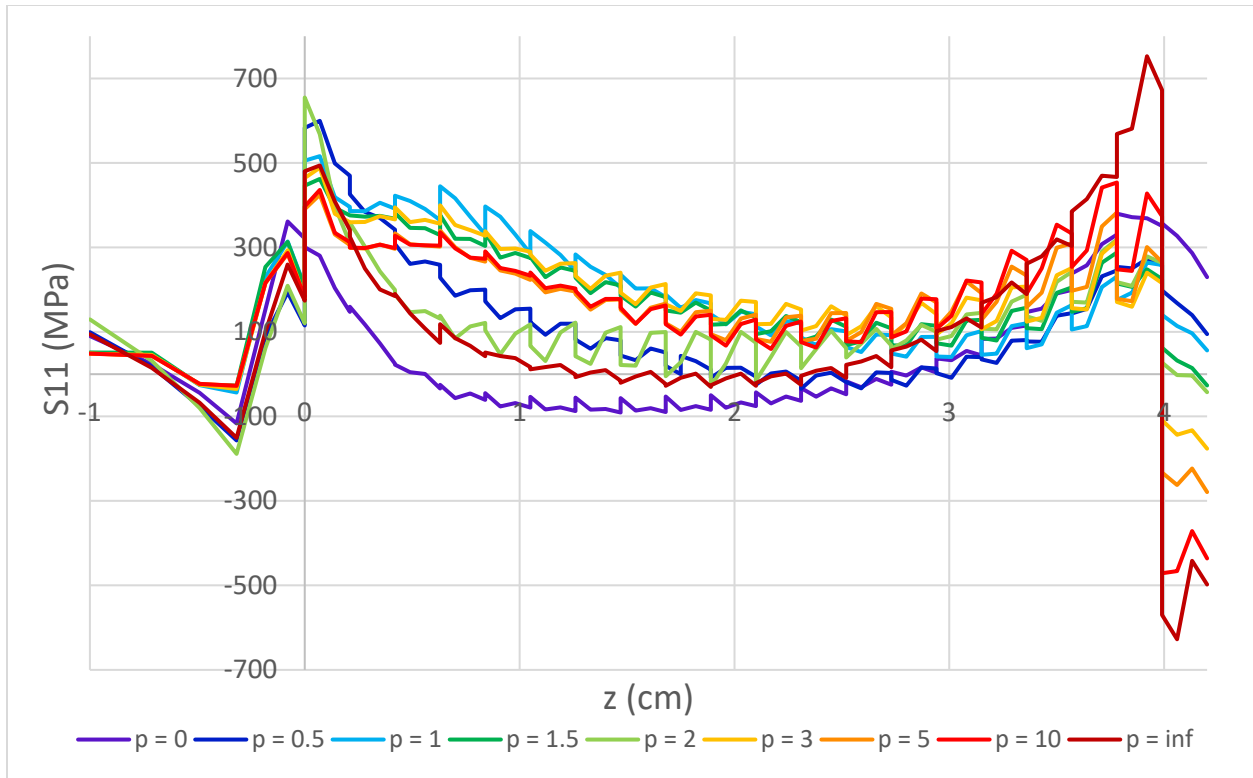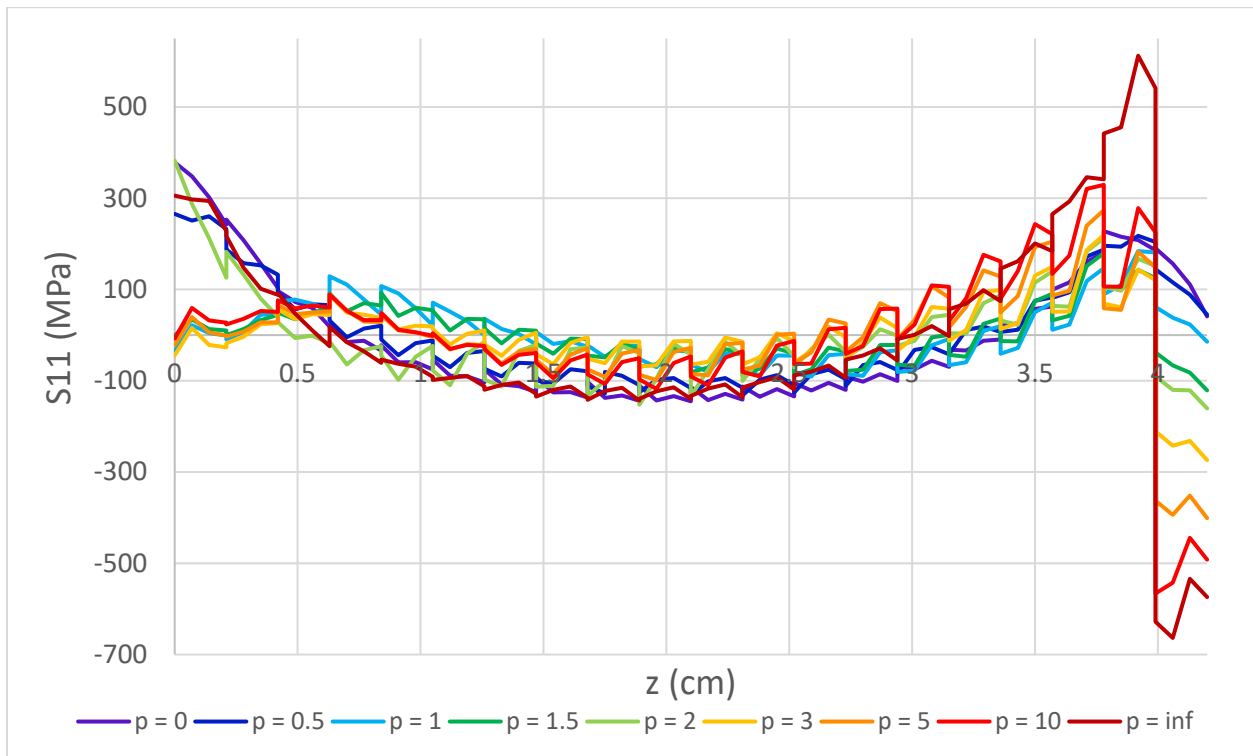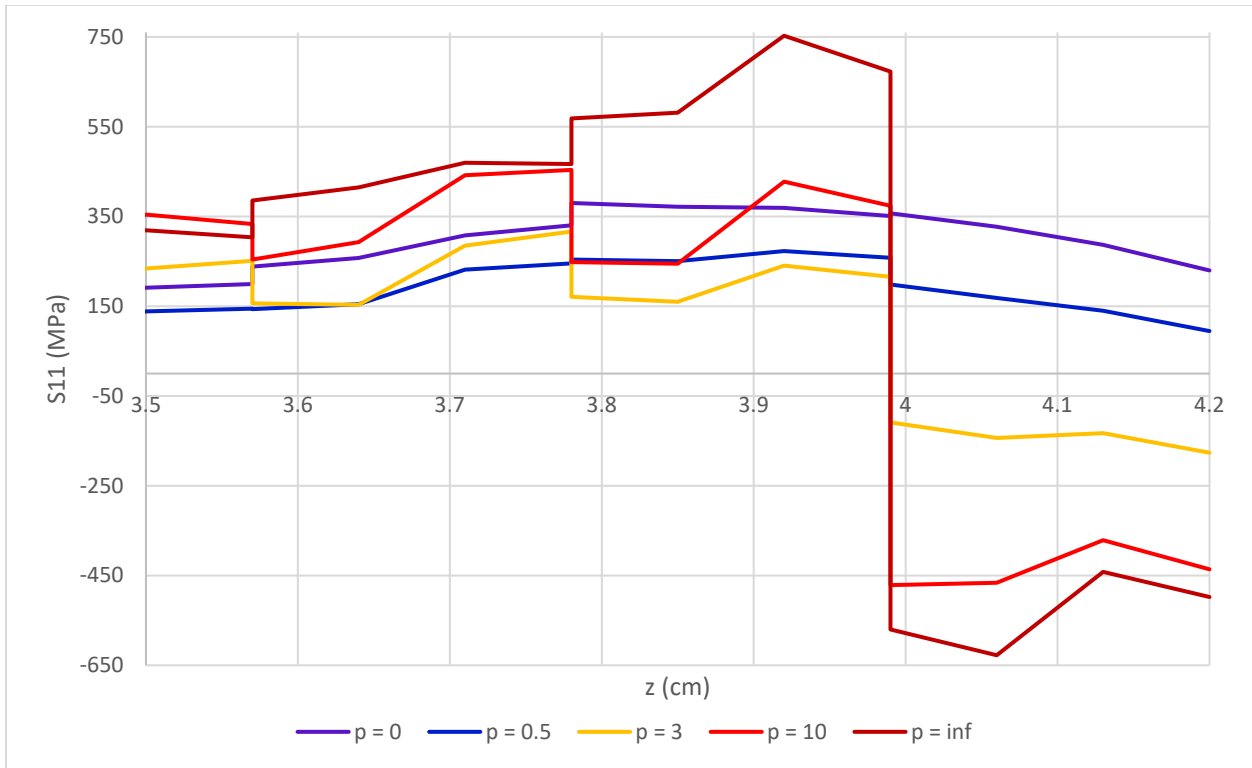The sensitivity of the results on the prescribed initial temperature of each layer was investigated. In Chapter 3, it was estimated that the accuracy of the predictions made in Table 4-2 was at least ±20%, or better. Therefore, the residual stress results for a linearly graded wall (p=1) were compared to the cases where the initial temperatures in Table 4-2 were varied by ±250°C. The comparison is shown in Figure 4-15 and Figure 4-16 with and without the substrate respectively. The blue curves (T-) correspond to the case where the initial temperatures were decreased by 250°C, the red curves (T+) correspond to the case where the initial temperatures were increased by 250°C, and the green curves are the original results for p = 1. In Table 4-3, the differences between each curve is summarized, with and without the substrate. The standard deviation, the maximum difference overall and the maximum difference near the top of the wall (z > 3.5cm) are given. It can be seen that overall, the differences are small (standard deviation of about 30 MPa), but when the layer initial temperatures are increased by 250°C the residual stress variation near the wall top is not negligible (~100 MPa). However, this level of sensitivity should not invalidate the trends obtained in this work which are summarized in Figure 4-14.
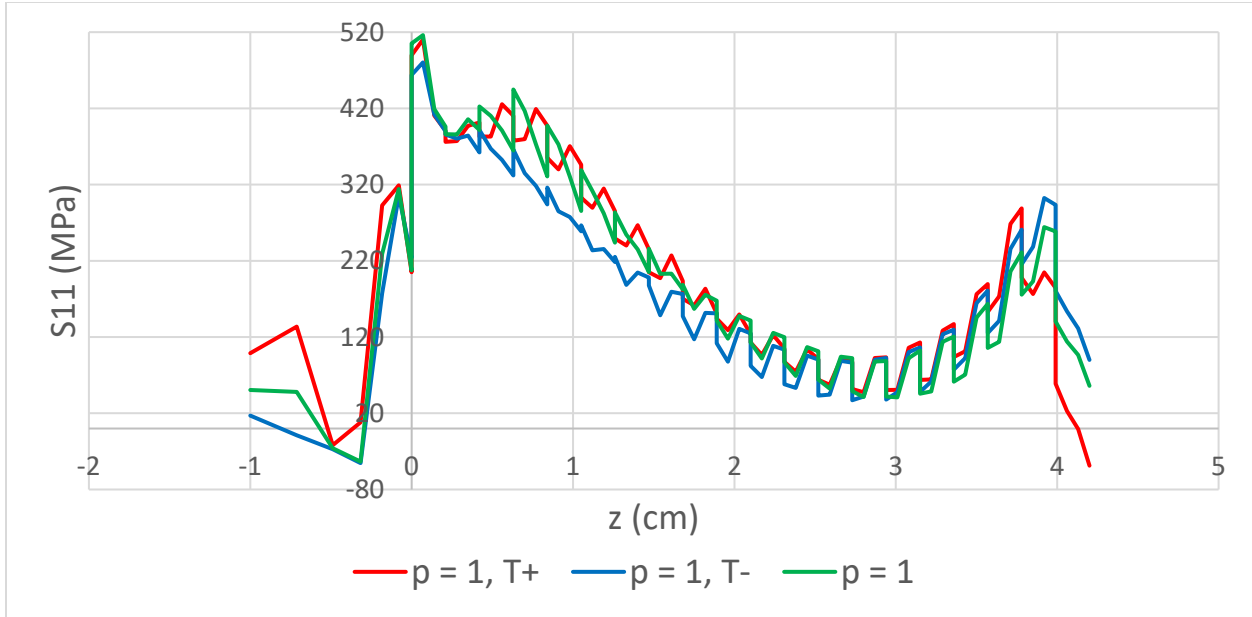
Figure 4-15: Residual stresses sensitivity on initial temperatures for p = 1 (with substrate)
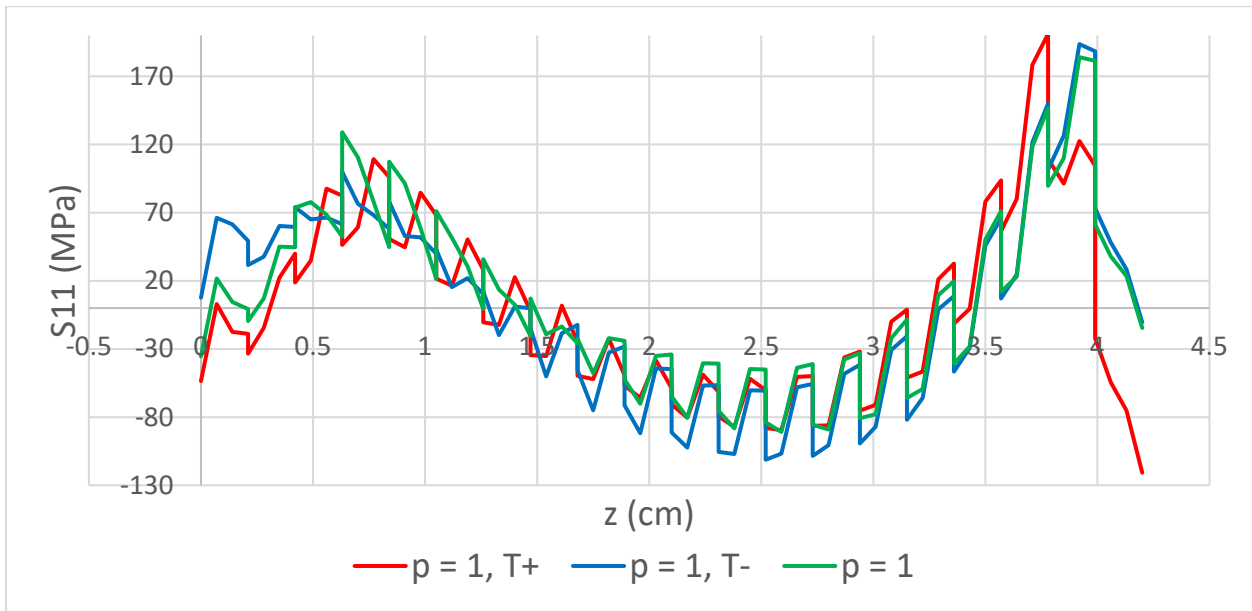
Figure 4-16: Residual stresses sensitivity on initial temperatures for p = 1 (substrate removed)

Table 4-3: Summary of residual stress sensitivity on initial temperatures for p = 1

Substrate	Std. Deviation T- (MPa)	Std. Deviation T+ (MPa)	Max Difference T- (MPa)	Max Difference T+ (MPa)	Max Diff. z > 3.5cm T- (MPa)	Max Diff. z > 3.5cm T+ (MPa)
With	35	35	90	105	45	105
Without	20	35	60	105	20	105

Chapter 5 : Conclusion and future work

The deposition of functionally graded materials with PTA-AM was simulated on Abaqus to predict the residual stress trends resulting from the process. It was assumed that higher compressive residual stresses near the surface of a WC-graded Ni-WC coating would result in increased wear and abrasion resistance.

Trends were obtained in the residual stress profile developed near the surface of a graded wall of such a material deposited on a steel substrate, as a function of the material gradient selected. The different gradations in WC that were considered were associated with a coefficient p that was the exponent in the power law function describing the gradation. It was concluded that the WC gradation should occur near the top/last layers (p > 1) and that a p-value of about 10 appeared to give a near optimal residual stress profile.

In order to obtain these results, preliminary work was done to estimate the initial temperature of each deposited layer as a function of its material composition and the operating parameters of the PTA. The heat input from the plasma arc to the weld pool was also estimated theoretically. This preliminary work included an estimation of the average temperature and axial velocity profile of the arc, a study of its interaction with the injected powder, and a prediction of the evolution of the temperature and velocity of the powder particles inside the plasma.

Further improvements could be made in a future work by studying the impact of a different interpass temperature on the obtained residual stress profiles, by changing the cooling time between each layer or/and the total heat input delivered to each layer during deposition. The decrease of the residual stresses formed at the interface with the substrate by using a higher heat input is another topic of interest. It is possible to link this different heat input to a specific set of operating parameters using the modeling done in the preliminary work. For example, the model predicts that increasing the torch standoff distance from 7 mm to 9 mm and the current from 50 A to 63 A while keeping the same other parameters increases the final powder particle temperature by about 500 K and the heat input delivered to the weld pool by about 200 W. The use of these parameters may decrease the residual stresses that form at the contact with the substrate and improve the metallurgical bond.

References

Abid, M., Parvez, S. & Nash, D., 2013. Effect of different electrode tip angles with tilted torch in stationary gas tungsten arc welding: A 3D simulation. *International Journal of Pressure Vessels and Piping,* Volume 108-109, pp. 51-60.

Ahmed, A., 1968. *Forced Convective Heat Transfer to Cooled Cylinders at Low Reynolds Numbers and with Large Temperature Differences,* Montréal: McGill University.

Aithal, S. M., Subramaniam, V. V., Pagan, J. & Richardson, R. W., 1988. Numerical model of a transferred plasma arc. *Journal of Applied Physics,* 84(7), p. 3506.

Aithal, S. M., Subramaniam, V. V., Pagan, J. & Richardson, R. W., 1998. Numerical model of a transferred plasma arc. *Journal of Applied Physics 84,* 84(7), pp. 3506-3518.

Amakawa, T. & al, 1998. Anode-boundary-layer behaviour in a transferred high-intensity arc. *Journal of Physics D: Applied Physics,* Volume 31, p. 2826.

Anon., n.d. *azom.com.* [Online]
Available at: https://www.azom.com/properties.aspx?ArticleID=1203
[Accessed 2022].

Anon., n.d. *engineeringtoolbox.com.* [Online]
Available at: https://www.engineeringtoolbox.com/metals-poissons-ratio-d_1268.html
[Accessed 2022].

Anon., n.d. *material-properties.org.* [Online]
Available at: https://material-properties.org/what-are-properties-of-inconel-718-nickel-based-superalloy-definition/
[Accessed 2022].

Anon., n.d. *tungsten-carbide-density-strength-hardness-melting-point.* [Online]
Available at: https://material-properties.org/tungsten-carbide-density-strength-hardness-melting-point/
[Accessed 2021].

Badisch, E. & Kirchgaßner, M., 2008. Influence of welding parameters on microstructure and wear behaviour of a typical NiCrBSi hardfacing alloy reinforced with tungsten carbide. *Surface & Coatings Technology,* 202(24), pp. 6016-6022.

Bao, G. & Cai, H., 1997. Delamination cracking in functionally graded coating metal substrate systems. *Acta Metallurgica,* 45(3), pp. 1055-1066.

Bhatti, A. A., Barsoum, Z., Murakawa, H. & Barsoum, I., 2015. Influence of thermo-mechanical material properties of different steel grades on welding residual stresses and angular distortion. *Materials and Design,* Volume 65, pp. 878-889.

Bobzin, K. & Öte, M., 2017. Numerical Coupling of the Particulate Phase to the Plasma Phase in Modeling of Multi-Arc Plasma Spraying. *Journal of Physics: Conference Series,* Volume 825, p. 012003.

Bouchafa, A. et al., 2010. Analytical modelling of thermal residual stresses in exponential functionally graded material system. *Materials and Design,* Volume 31, pp. 560-563.

Boulos, M. I., Fauchais, P. & Pfender, E., 1994. *Thermal Plasmas Fundamentals and Applications. Volume 1.* s.l.:Plenum Press.

Boulos, M. I. & Gauvin, W. H., 1974. Powder Processing in a Plasma Jet, a Proposed Model. *The Canadian Journal of Chemical Engineering,* 52(3), pp. 355-363.

Bourdin, E., P.Fauchais & Boulos, M., 1983. Transient heat conduction under plasma condition. *International Journal of Heat and Mass Transfer,* 26(4), pp. 567-582.

Caron, P., Diologent, F. & Drawin, S., 2010. Influence of Chemistry on the Tensile Yield Strength of Nickel-Based Single Crystal Superalloys. *Advanced Materials Research,* Volume 278, pp. 345-350.

Chen, X., 1988. Particle heating in a thermal plasma. *Pure and Applied Chemistry,* 60(5), pp. 651-662.

Chen, X., 1999. Heat and momentum transfer between a thermal plasma and suspended particles for different Knudsen numbers. *Thin Solid Films 345,* pp. 140-145.

Chen, X., Chyou, Y. P., Lee, Y. C. & Pfender, E., 1985. Heat Transfer to a Particle under Plasma Conditions with Vapor Contamination from the Particle. *Plasma Chemistry and Plasma Processing,* 5(2), pp. 119-141.

Chen, X. & Pfender, E., 1983. Effect of the Knudsen Number on Heat Transfer to a Particle Immersed into a Thermal Plasma. *Plasma Chemistry and Plasma Processing, Volume 3 No. 1,* pp. 97-113.

Chen, X., Qiu, J.-Y. & Yang, J., 1991. An Experimental Study of the Drag Force on a Sphere Exposed to an Argon Thermal Plasma Flow. *Plasma Chemistry and Plasma Processing,* 11(1), pp. 151-168.

Choi, H. K. & Gauvin, W. H., 1982. Operating Characteristics and Energy Distribution in Transferred Plasma Arc Systems. *Plasma Chemistry and Plasma Processing,* 2(4), pp. 361-386.

Choo, R., Szekely, J. & Westhoff, R., 1990. Modeling of High Current Arcs with Emphasis on Free Surface Phenomena in the Weld Pool. *Welding Journal,* Volume 69, pp. 346-361.

Choo, R., Szekely, J. & Westhoff, R., 1992. On the Calculation of the Free Surface Temperature of Gas-Tungsten-Arc Weld Pools from First Principles: Part I. Modeling the Welding Arc. *Metallurgical Transactions B,* Volume 23B, pp. 357-369.

Chyou, Y. P. & Pfender, E., 1989. Behavior of Particulates in Thermal Plasma Flows. *Plasma Chemistry and Plasma Processing,* 9(1), pp. 45-71.

Cobine, J. & Burger, E., 1955. Analysis of electrode phenomena in the high current arc. *Journal of Applied Physics,* 26(7), pp. 895-900.

Coudert, J. et al., 1993. Modelling and Experimental study of a transferred arc stabilized with argon and flowing in a controlled atmosphere chamber filled with argon at atmospheric pressure. *Plasma Chemistry and Plasma Processing,* 13(3), pp. 399-432.

Cressault, Y., 2008. *Propriétés des plasmas thermiques dans des mélanges Argon-Hydrogène-Cuivre,* Toulouse: Université Paul Sabatier.

Cressault, Y., Rouffet, M. E., Gleizes, A. & Meillot, E., 2010. Net emission of Ar–H2–He thermal plasmas at atmospheric pressure. *Journal of Physics D: Applied Physics,* Volume 43, p. 335204.

Dancer, C. et al., 2014. Effect of residual compressive surface stress on severe wear of alumina–silicon carbide two-layered composites. *Tribology International,* Volume 74, pp. 87-92.

Dean Deng, H. M. W. L., 2008. Numerical and experimental investigations on welding residual stress in multi-pass butt-welded austenitic stainless steel pipe. *Computational Materials Science.*

Deenadayalan, K., Murali, V., Elayaperumal, A. & Arulvel, S., 2021. Effective role of short time furnace heat treatment and laser treatment on the residual stress and mechanical properties of NiCrBSi-WC weldments produced using plasma transferred arc welding process. *Journal of Materials Research and Technology,* Volume 15, pp. 3492-3513.

Delluc, G., Ageorges, H., Pateyron, B. & Fauchais, P., 2005. Modelling of plasma jet and particle behaviour in spraying conditions. *High Temperature Material Processes,* 9(2).

Delluc, G., Ageorges, H., Pateyron, B. & Fauchais, P., 2005. Modelling of plasma jet and particle behaviour in spraying conditions. *High Temperature Material Processes.*

Deng, D., Murakawa, H. & Liang, W., 2007. Numerical and experimental investigations on welding residual stress in multi-pass butt-welded austenitic stainless steel pipe. *Computational Materials Science,* 42(2), pp. 234-244.

Deng, W. et al., 2020. Prediction of yield strength in a polycrystalline nickel base superalloy during interrupt cooling. *Scripta Materialia,* Volume 183, pp. 139-143.

Deuis, R., Yellup, J. & Subramanian, C., 1998. Metal-matrix composite coatings by PTA surfacing. *Composites Science and Technology,* 58(2), pp. 299-309.

Dinulescu, H. A. & Pfender, E., 1980. Analysis of the anode boundary layer of high intensity arcs. *Journal of Applied Physics,* 51(6), pp. 3149-3157.

Djebali, R., Pateyron, B. & Ganaoui, M. E., 2015. Scrutiny of plasma spraying complexities with case study on the optimized conditions toward coating process control. *Case Studies in Thermal Engineering,* Volume 6, pp. 171-181.

Doucet, A. & Flour, I., 1996. *Étude numérique du comportement de particules métalliques injectées dans un plasma d'arc électrique,* s.l.: EDF-DER.

Dowden, J. & Kapadia, P., 1994. Plasma arc welding: a mathematical model of the arc. *Journal of Physics D: Applied Physics,* Volume 27, pp. 902-911.

Dresvin, S. & Amouroux, J., 2007. Heat and Mass Transfer in Plasma Jets. *Advances in Heat Transfer,* Volume 40, pp. 451-521.

Essoltani, A., Proulx, P., Boulos, M. I. & Gleizes, A., 1994. Effect of the Presence of Iron Vapors on the Volumetric Emission of Ar/Fe and Ar/Fe/H2 Plasmas. *Plasma Chemistry and Plasma Processing,* 14(3), pp. 301-315.

Ettouil, F. B., 2008. *Modélisation rapide du traitement de poudres en projection par plasma d'arc,* s.l.: Matériaux, Université de Limoges.

F.Fernandes, et al., 2011. Effect of arc current on microstructure and wear characteristics of a Ni-based coating deposited by PTA on gray cast iron. *Surface and Coatings Technology,* 205(16), pp. 4094-4106.

Farraro, R. & McLellan, R., 1977. Temperature Dependence of the Young's modulus and shear modulus of pure nickel, platinum, and molybdenum. *Metallurgical Transactions A,* Volume 8A, pp. 1563-1565.

Fiszdon, J. K., 1979. Melting of Powder Grains in a Plasma Flame. *Int. J. Heat Mass Transfer,* Volume 22, pp. 749-761.

Fudolig, A. M., Nogami, H., J. Yagi, K. M. & Isshiki, M., 1997. Prediction of Surtace Temperature on Metal Beads Subjected to Argon-Hydrogen Transferred Arc Plasma Impingement. *ISIJ International,* 37(6), pp. 623-629.

Gajbhiye, R. V., 2022. *Image processing-based techniques for process parameter characterization in Plasma Transferred Arc Additive Manufacturing (PTA-AM) process,* Edmonton: University of Alberta.

Gleizes, A., Gonzalez, J. J., Liani, B. & Rahmani, B., 1990. Calculation of net emission coefficient in ArCu and SF6Cu thermal plasmas. *Le Journal de Physique Colloques,* 51(C5), pp. 213-220.

Gleizes, A., Rouffet, M.-E. & Cressault, Y., 2009. *New Method of Temperature Measurement in Thermal Plasmas Theory and Experimental Validation.* s.l., s.n.

Goodarzi, M. & al., 1997. The effect of the cathode tip angle on the GTAW arc and weld pool: I. Mathematical model of the arc. *J. Phys. D: Appl. Phys.,* Volume 30, p. 2744.

Gowtham, A. et al., 2020. Experimental investigations on laser cladding of NiCrBSi +WC coating on SS410. *Materials Today: Proceeding,* 27(3), pp. 1984-1989.

Hartmann, R. M. & Heberlein, J. V., 2001. Quantitative investigations on arc-anode attachments in transferred arcs. *Journal of Physics D: Applied Physics,* Volume 34, p. 2972.

Jenista, J., Heberlein, J. & Pfender, E., 1997. *Model for Anode Heat Transfer from an Electric Arc.* Athens, s.n.

Katsich, C. & Badisch, E., 2011. Effect of carbide degradation in a Ni-based hardfacing under abrasive and combined impact/abrasive conditions. *Surface & Coatings Technology,* 206(6), pp. 1062-1068.

Kim, C. S., 1975. *Thermophysical Properties of Stainless Steels,* s.l.: s.n.

Kou, X., Parks, G. & Tan, S., 2012. Optimal design of functionally graded materials using a procedural model and particle swarm optimization. *Computer-Aided Design,* 44(4), pp. 300-310.

Kuroda, S. & Clyne, T., 1991. Thin Solid Films. *The quenching stress in thermally sprayed coatings,* 200(1), pp. 49-66.

Lee, S. & Na, S., 1976. A numerical analysis of a stationary gas tungsten welding arc considering various electrode angles. *Welding Journal,* Volume 75, pp. 269-279.

Lee, S.-Y. & Na, S.-J., 1996. A Numerical Analysis of a Stationary Gas Tungsten Welding Arc Considering Various Electrode Angles. *Welding Research Supplement,* pp. 269-279.

Lee, Y. C., Chyou, Y. P. & Pfender, E., 1985. Particle Dynamics and Particle Heat and Mass Transfer in Thermal Plasmas. Part II. Particle Heat and Mass Transfer in Thermal Plasmas. *Plasma Chemistry and Plasma Processing, Vol. 5, No. 4,* pp. 391-414.

Lee, Y. C., Hsu, K. & Pfender, E., 1981. *Modeling of Particles Injected into a d.c. Plasma Jet.* Edinburgh, Scotland, s.n.

Leung, C. L. A. et al., 2019. The effect of powder oxidation on defect formation in laser additive manufacturing. *Acta Materialia,* Volume 166, pp. 294-305.

Lewis, J. A. & Gauvin, W. H., 1973. Motion of particles Entrained in a Plasma Jet. *AlChE,* 19(5), pp. 982-990.

Liu, H. et al., 2009. Simulation of thermal stresses in SiC–Al2O3 composite tritium penetration barrier by finite-element analysis. *Materials and Design,* 30(8), pp. 2785-2790.

Liu, J., Bolot, R. & Costil, S., 2014. Residual stresses and final deformation of an alumina coating: Modeling and measurement. *Surface & Coatings Technology,* Volume 268, pp. 241-246.

Li, W. et al., 2017. Fabrication and characterization of a functionally graded material from Ti-6Al-4V to SS316 by laser metal deposition. *Additive Manufacturing,* Volume 14, pp. 95-104.

Li, W. et al., 2019. Temperature-dependent elastic modulus model for metallic bulk materials. *Mechanics of Materials,* Volume 139, p. 103194.

Liyanage, T., Fisher, G. & Gerlich, A., 2012. Microstructures and abrasive wear performance of PTAW deposited Ni–WC overlays using different Ni-alloy chemistries. *Wear,* Volume 274-275, pp. 345-354.

Li, Y., Feng, Y.-H., Zhang, X.-X. & Wu, C.-S., 2013. An improved simulation of heat transfer and fluid flow in plasma arc welding with modified heat source model. *International Journal of Thermal Sciences,* Volume 64, pp. 93-104.

Li, Y., Su, C., Zhou, X. & Wu, C., 2020. A more precise unified model to describe comprehensive multiphysics and multiphase phenomena in plasma arc welding. *Journal of Manufacturing Processes,* Volume 59, p. 668–678.

Lowke, J. J., 1979. Simple theory of free-burning arcs. *J. Phys. D: Appl. Phys.,* Volume 12, p. 1873.

Lu, S.-P., Kwon, O.-Y. & Guo, Y., 2003. Wear behavior of brazed WC/NiCrBSi(Co) composite coatings. *Wear,* 254(5-6), pp. 421-428.

M.H. Yu, B. Z. D. B. D. S., 2010. Preparation of graded multilayer materials and evaluation of residual stresses. *Materials and Design.*

McKelliget, J. & Szekely, J., 1986. Heat Transfer and Fluid Flow in the Welding Arc. *Metallurgical Transactions A,* Volume 17A, pp. 1139-1148.

Menart, J. & Malik, S., 2002. Net emission coefficients for argon-iron thermal plasmas. *Journal of Physics D: Applied Physics,* Volume 35, pp. 867-874.

Metcalfe, J. & Quigley, M., 1975. Heat Transfer in Plasma-Arc Welding. *Welding Journal,* Volume 54, pp. 99-103.

Mirkoohi, E., Sievers, D. E., Garmestani, H. & Liang, S. Y., 2020. Thermo-mechanical modeling of thermal stress in metal additive manufacturing considering elastoplastic hardening. *CIRP Journal of Manufacturing Science and Technology,* Volume 28, pp. 52-67.

Moghazi, S. N. E., Wolfe, T., Ivey, D. G. & Henein, H., 2020. Plasma transfer arc additive manufacturing of 17-4 PH: assessment of defects. *The International Journal of Advanced Manufacturing Technology,* 108(7-8), pp. 2301-2313.

Mulkey, J. R., 1971. *Strain Hardening Exponent for 17-4 PH Stainless Steel,* s.l.: AEC Research and Development.

Nestor, O. H., 1962. Heat Intensity and Current Density Distributions at the Anode of High Current, Inert Gas Arcs. *Journal of Applied Physics,* Volume 33, p. 1638.

Oliveira, J., Santos, T. & Miranda, R., 2020. Revisiting fundamental welding concepts to improve additive manufacturing: From theory to practice. *Progress in Materials Science,* Volume 107, p. 100590.

P. Wu, C. Z. X. T., 2003. Microstructural characterization and wear behavior of laser cladded nickel-based and tungsten carbide composite coatings. *Surface and Coatings Technology.*

Paik, S., Nguyen, H. D. & Chung, J. N., 1993. A study of argon thermal plasma flow over a solid sphere. *Journal of Fluid Mechanics,* Volume 252, pp. 543-564.

Pfender, E. & Lee, Y. C., 1985. Particle Dynamics and Particle Heat and Mass Transfer in Thermal Plasmas. Part I. The Motion of a Single Particle without Thermal Effects. *Plasma Chemistry and Plasma Processing,* 5(3), pp. 211-237.

Pierson, H. O., 1996. *Handbook of Refractory Carbides and Nitrides. Chapter VI,* s.l.: William Andrew.

Quigley, M., Richards, P., Swift-Hook, D. & Gick, A., 1973. Heat flow to the workpiece from a TIG welding arc. *Journal of Physics D: Applied Physics,* Volume 6, pp. 2250-2259.

Ravichandran, K. S., 1994. Elastic Properties of Two-Phase Composites. *Journal of the American Ceramic Society,* 77(5), pp. 1178-1184.

Ravichandran, K. S., 1995. Thermal residual stresses in a Functionally Graded Material System. *Materials Science and Engineering,* 201(1-2), pp. 269-276.

Rojas, J. G. M., 2021. *Design and system identification for a plasma transferred arc additive manufacturing technology,* Edmonton: University of Alberta.

Rojas, J. M., Wolfe, T., Fleck, B. & Qureshi, A. J., 2018. Plasma transferred arc additive manufacturing of Nickel metal matrix composites. *Manufacturing Letters,* Volume 18, pp. 31-34.

Rosenhow, W., Hartnett, J. & Cho, Y. I., 1973. *Handbook of Heat Transfer, Chapter 6 p. 37.* New York: McGraw-Hill.

Sames, W. J. et al., 2016. The metallurgy and processing science of metal additive manufacturing. *International Materials Reviews,* 61(5), pp. 315-360.

Sanders, N. A. & Pfender, E., 1984. Measurement of anode falls and anode heat transfer in atmospheric pressure high intensity arcs. *Journal of Applied Physics,* Volume 55, pp. 714-722.

Sanders, N., Etemadi, K., Hsu, K. C. & al., 1982. Studies of the anode region of a high-intensity argon arc. *Journal of Applied Physics,* Volume 53, p. 4136.

Schnick, M., Füssel, U. & Spille-Kohoff, A., 2010. Numerical Investigations of Design Parameters, Gas Composition and Electric Current in Plasma Arc Welding (PAW). *Welding in the World,* 54(3/4), pp. R87-R96.

Serres, N. et al., 2011. Microstructures and mechanical properties of metallic NiCrBSi and composite NiCrBSi–WC layers manufactured via hybrid plasma/laser process. *Applied Surface Science,* Volume 257, pp. 5132-5137.

Shi, Y., Li, Y., Liu, J. & Yuan, Z., 2017. Investigation on the parameter optimization and performance of laser cladding a gradient composite coating by a mixed powder of Co50 and Ni/WC on 20CrMnTi low carbon alloy steel. *Optics and Laser Technology,* Volume 99, pp. 256-270.

Song, B. et al., 2020. The relationship between convection mechanism and solidification structure of the iron-based molten pool in metal laser direct deposition. *International Journal of Mechanical Sciences,* Volume 165, p. 105207.

Song, X. et al., 2017. A new model for predicting drag coefficient and settling velocity of spherical and non-spherical particle in Newtonian fluid. *Powder Technology,* Volume 321, pp. 242-250.

Sudha, C. et al., 2008. Microchemical and microstructural studies in a PTA weld overlay of Ni–Cr–Si–B alloy on AISI 304L stainless steel. *Surface and Coatings Technology,* 202(10), pp. 2103-2112.

Tabernero, I., Paskual, A., Álvarez, P. & Suárez, A., 2018. Study on Arc Welding Processes for High Deposition Rate Additive Manufacturing. *Procedia CIRP,* Volume 58, pp. 358-362.

Touloukian, Y. S., 1967. *Thermophysical Properties of High Temperatures Solid Materials,* New York: Macmillan.

Touloukian, Y. S. & Buyco, E. H., 1971. *Thermophysical Properties of Matter - The TRPC Data Series. Volume 4. Specific heat - Metallic Elements and Alloys,* s.l.: s.n.

Touloukian, Y. S. & Ho, C. Y., 1975. *Thermophysical Properties of Matter - The TPRC Data Series. Volume 12. Thermal Expansion Metallic Elements and Alloys,* s.l.: s.n.

Touloukian, Y. S. & Makita, T., 1970. *Thermophysical Properties of Matter - The TPRC data series. Volume 6. Specific Heat - Nonmetallic Liquids and Gases,* s.l.: s.n.

Touloukian, Y. S., Powell, R. W., Ho, C. Y. & Klemens, P. G., 1970. *Thermophysical Properties of Matter - The TPRC Data Series. Volume 1. Thermal Conductivity - Metallic Elements and Alloys,* s.l.: s.n.

Trelles, J., Chazelas, C., Vardelle, A. & Heberlein, J., 2009. Arc Plasma Torch Modeling. *Journal of Thermal Spray Technology,* 18(5-6), pp. 728-752.

Valarezo, A. et al., 2010. Damage tolerant functionally graded WC–Co/Stainless Steel HVOF coatings. *Surface & Coatings Technology,* 205(7), pp. 2197-2208.

Vardelle, M., Vardelle, A., Fauchais, P. & Boulos, M. I., 1983. Plasma-Particle Momentum and Heat Transfer: Modeling and Measurement. *AIChE Journal,* 29(2), pp. 236-243.

Wan, Y. P. et al., 1999. Model and Powder Particle Heating, Melting, Resolidification, and Evaporation in Plasma Spraying Processes. *Journal of Heat Transfer, Volume 121,* pp. 691-699.

Weisbrook, C. & Krawitz, A., 1996. Thermal residual stress distribution in WC-Ni composites. *Materials Science and Engineering,* Volume A209, pp. 318-328.

Wolf, B., 1995. *Handbook of ion sources p.28.* s.l.:CRC Press.

Wolfe, T., 2010. *Homogeneity of metal matrix composites deposited by plasma transferred arc welding.* Edmonton: University of Alberta.

Xibao, W. & Hua, L., 1998. Metal powder thermal behaviour during the plasma transferred-arc surfacing process. *Surface and Coatings Technology 106,* p. 156–161.

Xu, C. & Todd, R. I., 2015. Functionally graded ceramics by a new in situ processing route: Residual stress and wear resistance. *Journal of the European Ceramic Society,* 35(9), pp. 2693-2698.

Yoshida, T. & Akashi, K., 1977. Particule heating in a-radiofrequency plasma torch. *Journal of Applied Physics,* Volume 48, pp. 2252-2261.

Zhang, R., Jiang, F. & Chen, S., 2016. Comparison of energy acted on workpiece among Twin-body Plasma Arc Welding, Non-transferred Plasma Arc Welding and Plasma Arc Welding. *Journal of Manufacturing Processes,* 24(1), pp. 152-160.

Zhang, X. et al., 2017. A novel temperature dependent yield strength model for metals considering precipitation strengthening and strain rate. *Computational Materials Science,* Volume 129, pp. 147-155.

Zhou, X. & Heberlein, J., 1998. An experimental investigation of factors affecting arc-cathode erosion. *Journal of Physics D: Applied Physics,* Volume 31, p. 2577.

Zhu, T. & al, 2019. Numerical simulation of constricted and diffusive arc–anode attachments in wall-stabilized transferred argon arcs. *Plasma Science and Technology,* Volume 21, p. 125406.

Zhu, X. & Chao, Y., 2002. Effects of temperature-dependent material properties on welding simulation. *Computers and Structures,* Volume 80, pp. 967-976.

Appendix A - Temperature dependent properties of the MMC

This appendix provides details about the temperature dependent properties used for the nickel-based alloy and for the tungsten carbide respectively, and explicits how the compositional properties were computed. Trendlines were fitted to the collected data using Excel and their corresponding equations are reported in this section for temperatures up to 3000K.

A.1 Thermal Properties

This subsection provides information about the MMC thermal properties used in this work.

A.1.A Nickel alloy or pure nickel

The NiCrBSi used in the work of (Wolfe, 2010) was found to have a latent heat of 79410 J/kg, a solidus temperature of 1012°C (1285K) and a liquidus temperature of 1036°C (1309K). Although a NiBSi alloy was considered in the present work instead, the same latent heat and solidus/liquidus temperatures were used. Pure nickel density at room temperature is 8900kg/m^3.

Conductivity

Only data concerning the conductivity of pure nickel up to melting temperature was found, in (Touloukian, et al., 1970). The conductivity in liquid state is not known, however based on an observation that thermal conductivities of many metals are divided by two upon melting (Kim, 1975), it was decided to apply that rule for the nickel. The equations that were derived for the temperature dependence of the nickel conductivity is summarized in Table A-1.

Table A-1: Conductivity of nickel

Temperature range (K)	Conductivity (W.m^{-1}.K^{-1})
300 – 630	9.2561E-05*T^2 - 1.6634E-01*T + 1.3197E+02
630 – 1285	2.1552E-02*T + 5.0203E+01
1285 – 1309	78 - (T-1285)/(1309-1285)*39
1309 – 3000	39

Heat Capacity

The heat capacity of the NiBSi alloy used in this work was predicted using Thermocalc. The equations that were derived for the temperature dependence of the nickel heat capacity is summarized in Table A-2.

Table A-2: Heat capacity of the nickel alloy

Temperature range (K)	Heat capacity (J.kg^{-1}.K^{-1})
300 – 590	9.1297E-04*T^2 - 2.0726E-01*T + 4.6867E+02
590 – 800	9.6458E-04*T^2 - 1.2214E+00*T + 9.8892E+02
800 – 1700	1.3506E-04*T^2 - 1.0858E-01*T + 5.6609E+02
1700 – 3000	780

A.1.B Tungsten carbide

The tungsten carbide melting temperature is 2870°C (3143K) (Pierson, 1996) with a latent heat of at least 330 J/g (Anon., n.d.). At room temperature, it has a density of 15 700 kg/m^3.

Conductivity

The temperature dependent conductivity of tungsten carbide was extracted from (Touloukian, 1967). The equations that were derived for the temperature dependence of the tungsten carbide conductivity is summarized in Table A-3.

Table A-3: Conductivity of tungsten carbide

Temperature range (K)	Conductivity (W.m^{-1}.K^{-1})
300 – 3000	0.0081*T + 35.084

Heat Capacity

The temperature dependent heat capacity of tungsten carbide up to 2800K was extracted from (Touloukian, 1967). The heat capacity above 2800K was simply extrapolated at a constant value. The equations that were derived for the temperature dependence of the tungsten carbide heat capacity is summarized in Table A-4.

Table A-4: Heat capacity of tungsten carbide

Temperature range (K)	Heat capacity (J.kg^{-1}.K^{-1})
300 – 2800	-1.02253651E-17*T^6 + 1.10400943E-13*T^5 - 4.75984126E-10*T^4 + 1.04543043E-06*T^3 - 1.23866966E-03*T^2 + 7.92096454E-01*T + 3.20027793E+01
2800 – 3000	304

A.1.C Compositional properties

A rule of mixture was applied for intermediate compositions, using the volume fraction of WC for the conductivity and the mass fraction of WC for the heat capacity.

A.2 Mechanical Properties

This subsection provides information about the MMC mechanical properties used in this work.

Since the purpose of this work is to show trends in residual stresses derived from different material gradients, it is not necessary to seek great precision in the results. Therefore, for simplicity, an elastic - perfectly plastic model has been adopted.

Only three mechanical properties are then required to perform the simulations, namely the modulus of elasticity, the yield strength and the coefficient of thermal expansion (CTE). Again, for simplicity, the materials were systematically approximated as isotropic.

A.2.A Nickel alloy or pure nickel

The temperature dependence of the Young Modulus and Yield Strength up to the melting temperature of the nickel alloy studied is not well known and few data are available in the literature, especially for high temperatures. According to (Bhatti, et al., 2015) and (Zhu & Chao, 2002), specifying the temperature dependence of the yield strength is important for the residual stresses results while taking the elastic modulus as constant is acceptable.

Elastic Modulus and Poisson Coefficient

The Poisson coefficient of nickel is 0.31 (Anon., n.d.) and is considered constant for all temperatures.

A model for the temperature dependence of the elastic modulus with temperature for superalloys was also developed in (Li, et al., 2019). The following relation was proposed (A-1):

$$E(T) = \frac{(1 + \int_0^{T_0} \alpha(t)dt)^3}{(1 + \int_0^{T} \alpha(t)dt)^3} \times \left\{ 1 - \frac{T - T_0}{T_1 - T_0}[1 - (\frac{E(T_1)}{E(T_0)} \times \frac{(1 + \int_0^{T_1} \alpha(t)dt)^3}{(1 + \int_0^{T_0} \alpha(t)dt)^3})^2] \right\}^{1/2} E(T_0) \quad (A-1)$$

In this relation, T_0 and T_1 are two arbitrary reference temperatures and α is the linear coefficient of thermal expansion. In their model, the authors incorporated the macroscopic laws governing the effects of temperature on the elastic modulus but did not account for any potential micro-

mechanisms such as phase transformation or grain boundary slip. The authors verified that this formula yielded good agreement with experimental data for different Ni-based superalloys. The Young modulus at room temperature for these alloys was about 220 GPa.

Alternatively, (Farraro & McLellan, 1977) proposed a linear dependency of the elastic moduli of nickel with temperature up to 1000°C to approximately follow the following relation (T in °C):

$$E(T) = 242 - 0.0933 * T \ (GPa) \tag{A-2}$$

These two correlations are compared in Figure A-1. In (Serres, et al., 2011), a NiCrBSi superalloy with similar properties to the one considered in this work was reported to have an elastic modulus of 230 GPa at room temperature. Therefore, in Li's correlation, T_0 was selected at 25°C and $E(T_0)$ at 230 GPa. Based on the data for the nickel superalloys studied in (Li, et al., 2019), T_1 was selected at 500°C and $E(T_1)$ at 200 GPa.
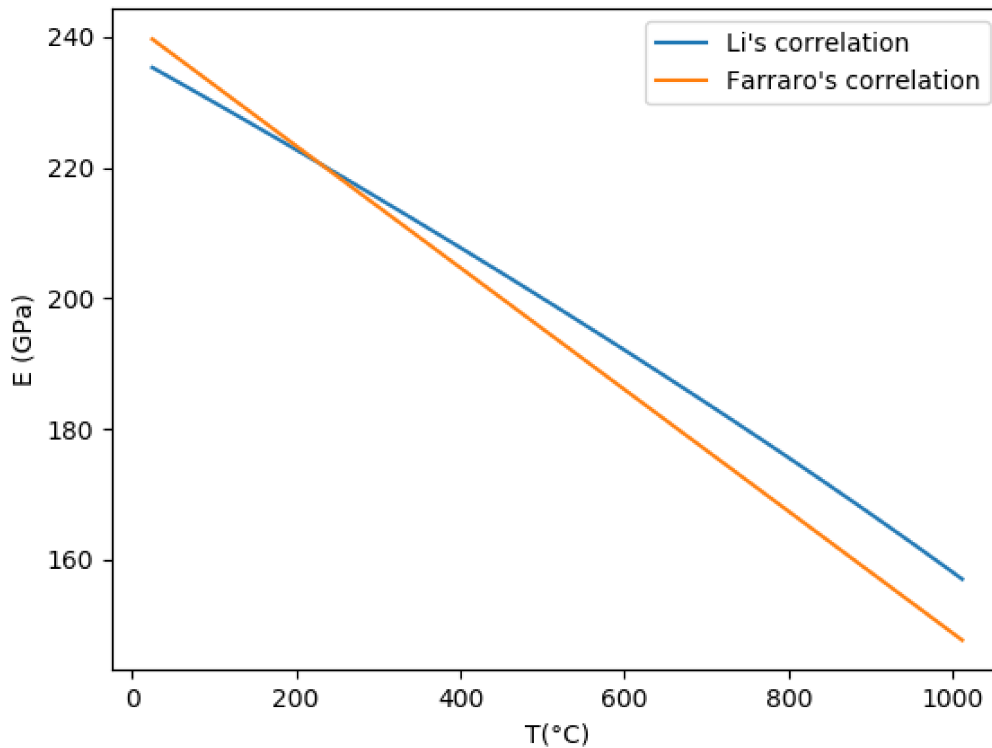

Figure A-1: Estimations of the nickel superalloy elastic modulus dependency on temperature

In Figure A-1, it can be seen that Farraro's correlation for pure nickel is close to Li's correlation for nickel-based superalloys. This improves the confidence in these correlations. In this work, Li's correlation will be used. While taking a constant elastic modulus is still acceptable for residual stresses predictions, these correlations should improve the accuracy of the results to some extent.

Yield Strength

Due to the scarcity of available data regarding this property at high temperatures, (Zhu & Chao, 2002) proposed an engineering approximation which is the following piece-wise linear function:

$$\sigma_y(T) = \begin{cases} \sigma_y(T_0) & 25°C \leq T \leq 100°C \\ 5\%\sigma_y(T_0) + \frac{T_1-T}{T_1-100} * 95\%\sigma_y(T_0) & 100°C \leq T \leq T_1 \\ 5\%\sigma_y(T_0) & T \geq T_1 \end{cases} \tag{A-3}$$

The threshold T_1 was at about two third of the melting temperature. They found that the exact value of T_1 had little influence on the residual stress results. The value of 5% of room temperature yield strength near the melting temperature was selected arbitrarily instead of 0 to avoid numerical difficulties.

Alternatively, in the work of (Zhang, et al., 2017) was proposed a model to predict the yield strength of a metallic alloy at arbitrary temperatures based on its elastic modulus and poisson's ratio at that temperature, and its room temperature mechanical properties. The following relation was proposed:

$$\sigma_y(T) = \sigma_y(T_0)(\frac{T_m-T}{T_m-T_0} \cdot \frac{E_T}{E_{T_0}} \cdot \frac{1+v_{T_0}}{1+v_T})^{1/2} \tag{A-4}$$

It is known that the inter-metallic compound based on the formula $Ni_3(Al,Ti)$ is responsible for maintaining constant yield strength up to relatively high temperatures, but the chemical composition of the alloy used in this work does not include Al or Ti. The yield strength of nickel-based superalloys at room temperature is variable but generally hovers around 1000 MPa (Anon., n.d.) (Deng, et al., 2020) (Caron, et al., 2010). Although the exact yield strength of the superalloy used in this work is not known even at room temperature, the approximate value of 1000 MPa is nonetheless chosen because the goal is only to evaluate the residual stresses trends as a function of the material gradient chosen, rather than predicting their exact values.

Based on a 1 000 MPa yield strength at room temperature, the respective correlations of Zhu and Zhang are compared in Figure A-2. When using Zhang's correlation (Equation (A-4), the temperature dependent elastic modulus was evaluated with Li's correlation (Cf. Figure A-1).
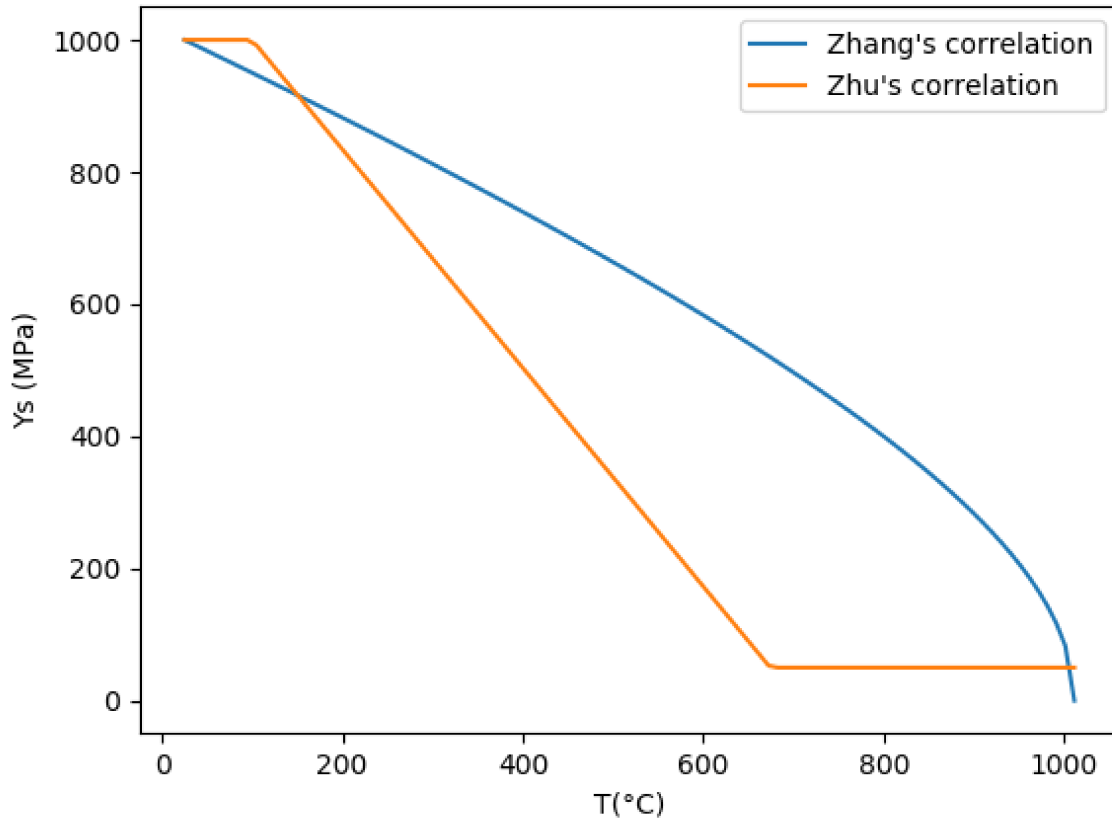

Figure A-2: Estimations of the nickel superalloy yield strength dependency on temperature

In what follows, the correlation of Zhang will be used but with a minimum yield strength of 50 MPa near melting temperature to avoid numerical difficulties (the Abaqus simulations would fail to converge otherwise).

Coefficient of Thermal Expansion

Finally, the temperature dependent CTE for pure nickel was extracted from (Touloukian & Ho, 1975). The equations that were derived for the temperature dependence of the tungsten carbide linear coefficient of thermal expansion up to melting temperature is summarized in Table A-5.

Table A-5: Coefficient of thermal expansion of nickel

Temperature range (K)	Coefficient of Thermal Expansion (W.m^{-1}.K^{-1})
300 – 1285	-1.1921E-06*T^2 + 5.0032E-03*T + 1.2500E+01

A.2.B Tungsten carbide

All mechanical properties for the tungsten carbide were taken constant with regard to temperature. These property data were taken from (Pierson, 1996), (Weisbrook & Krawitz, 1996) and (Anon., n.d.). They are summarized in Table A-6.

Table A-6: Tungsten carbide mechanical properties

Elastic Modulus (GPa)	Yield Strength (MPa)	CTE (µm/m/K)	Poisson coefficient
670 (620 – 720)	330	5	0.25

A.2.C Compositional properties

In the work of (Ravichandran, 1994) were derived analytical expressions estimating the isotropic elastic properties in a two-phase system containing discontinuous reinforcements (Equations A-5 to A-7).

$$E_{comp} = \frac{E_{Ni}^2 + (E_{Ni}E_{WC} - E_{Ni}^2)V_{WC}^{2/3}}{E_{Ni} + (E_{WC} - E_{Ni})V_{WC}^{2/3}(1 - V_{WC}^{1/3})} \tag{A-5}$$

$$\nu_{comp} = \frac{\nu_{WC}E_{Ni} + c\nu_{Ni}E_{WC} + \nu_{Ni}E_{Ni}(2c + 3c^2 + c^3)}{cE_{WC} + E_{Ni}(1 + 2c + 3c^2 + c^3)} \tag{A-6}$$

$$c = (\frac{1}{V_{WC}})^{1/3} - 1 \tag{A-7}$$

These formulas are applied to the case where WC is reinforcing the nickel-based matrix to derive the temperature dependent Poisson coefficients and Elastic moduli at intermediate compositions. Results at room temperature are given as an example in Figure A-3 and Figure A-4. In Figure A-3, a comparison with the experimental results of (Serres, et al., 2011) for a WC-NiCrBSi alloy is included (with the min and max curves representing the experimental uncertainty range). The minimum value of 620 GPa was chosen for the WC modulus of elasticity because the correlation predictions were higher. It can be seen that Ravichandran's correlation is closer to Serre's

experimental results than the rule of mixture. Therefore, for the evaluation of the elastic properties of the composite, Ravichandran's correlation will be used in the present work and the Young's modulus of tungsten carbide will be considered as 620 GPa. For the evaluation of the yield strength of the composite and the coefficient of thermal expansion, however, a simple rule of mixture is used (using the volume fraction of tungsten carbide).
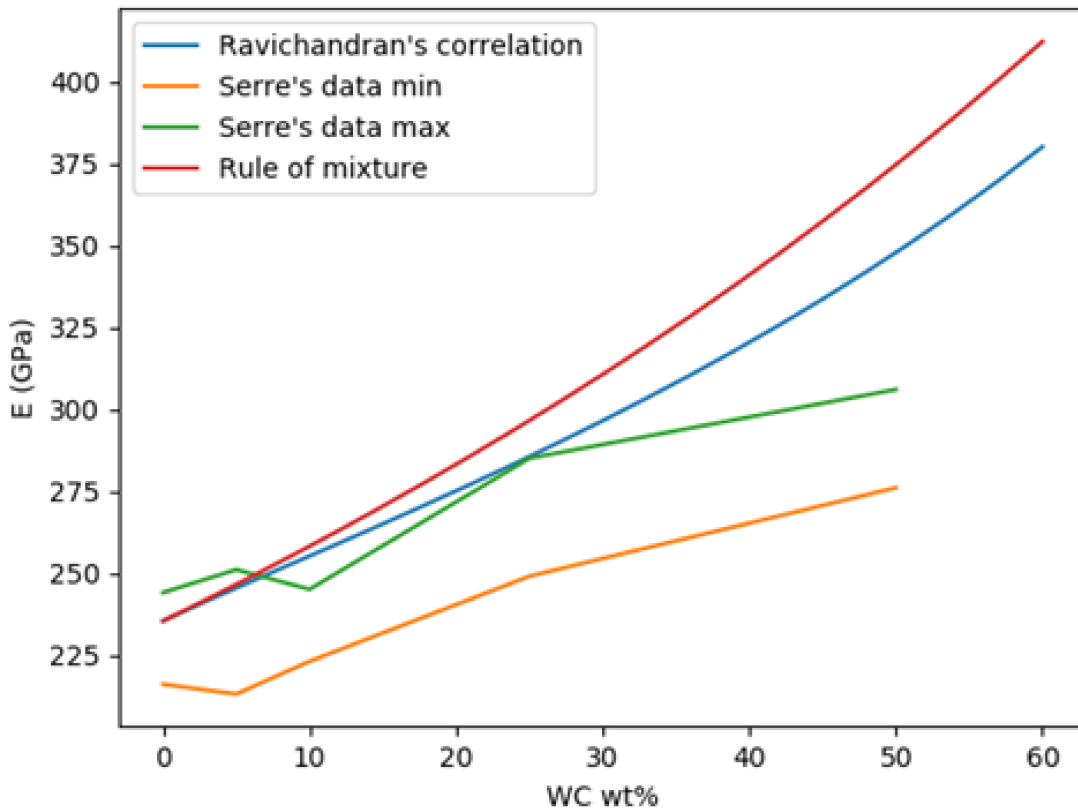

Figure A-3: Estimations of the MMC elastic modulus dependency on the WC weight content
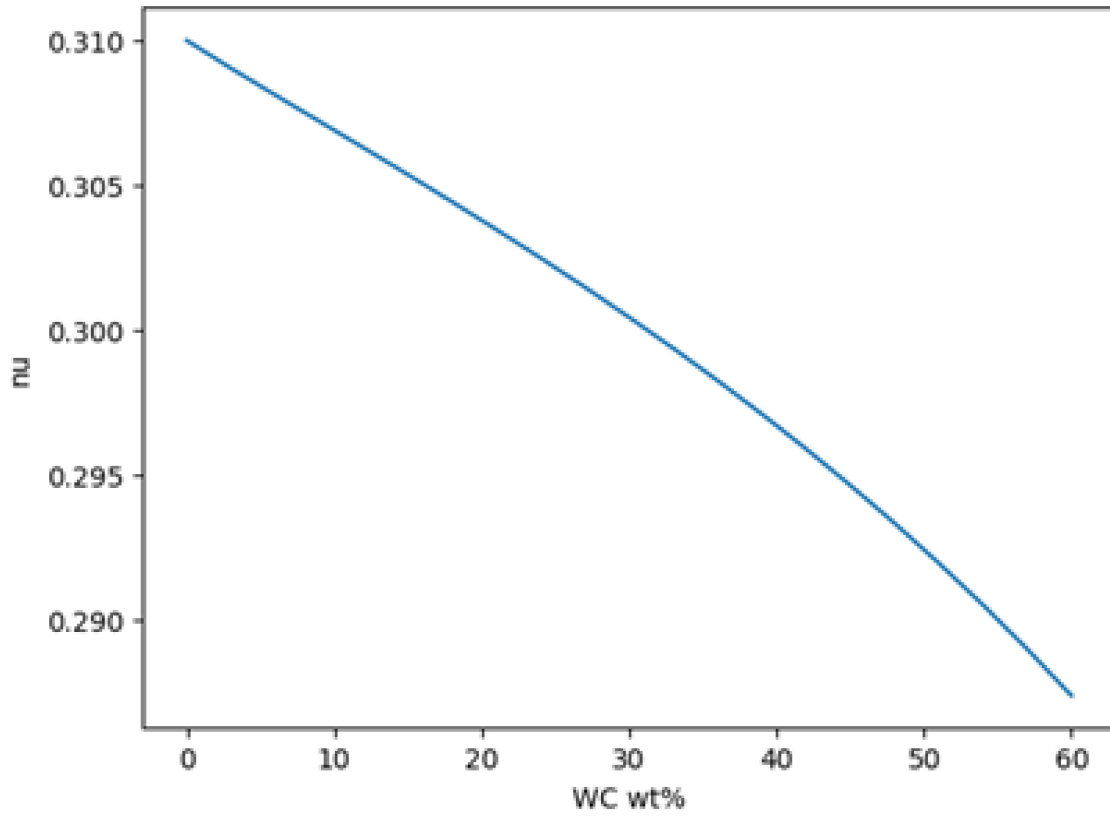
Figure A-4: Estimations of the MMC poisson coefficient dependency on the WC weight content

Appendix B - Temperature dependent properties of the plasma

This appendix provides details about the temperature dependent properties used for the argon and for the Ar/5%H_2 plasma gas. Trendlines were fitted to the literature data using Excel and their corresponding equations are reported in this section for temperatures up to 22 000K for the net emission coefficient and up to 24 000K for the other properties.

B.1 Argon plasma

The temperature dependent properties of argon plasma are summarized from Table B-1 to Table B-8. Except for the net emission coefficient, the data for all these properties was found in (Boulos, et al., 1994). The data for the net emission coefficient is taken from (Cressault, 2008), (Cressault, et al., 2010), (Menart & Malik, 2002), (Gleizes, et al., 1990). As explained in the section 2) a) i) of Chapter 2, the NEC at 2mm for a given temperature is not exactly known so a minimum and a maximum estimated value are provided in Table B-7 and Table B-8.

Table B-1: Argon density

Temperature range (K)	Density (kg.m^{-3})
500 – 3 000	4.8647E+02*T - 9.9992E-01
3 000 – 10 000	-1.13964688E-20*T^5 + 4.34956254E-16*T^4 - 6.74351189E-12*T^3 + 5.41768839E-08*T^2 - 2.37222835E-04*T + 5.35682248E-01
10 000 – 18 000	3.8156170977E-25*T^6 - 3.4224064024E-20*T^5 + 1.2571753319E-15*T^4 - 2.4177467503E-11*T^3 + 2.5679987207E-07*T^2 - 1.4353270677E-03*T + 3.3675813960E+00
18 000 – 24 000	-7.641509E-15*T^3 + 4.860462E-10*T^2 - 1.108048E-05*T + 1.006914E-01

Table B-2: Argon enthalpy

Temperature range (K)	Enthalpy (J.kg^{-1})
500 – 3 000	520.45*T - 155449
3 000 – 8 500	3.479406E-06*T^3 - 5.153626E-02*T^2 + 7.660631E+02*T - 5.306921E+05
8 500 – 15 000	-4.2485494750E-16*T^6 + 2.4468466982E-11*T^5 - 5.7095807468E-07*T^4 + 6.9621821945E-03*T^3 - 4.6832629517E+01*T^2 + 1.6481535092E+05*T - 2.3351403950E+08
15 000 – 24 000	-1.42515946E-09*T^4 + 2.48157915E-04*T^3 - 1.11579102E+01*T^2 + 1.96892784E+05*T - 1.17307276E+09

Table B-3: Argon specific heat

Temperature range (K)	Specific heat (J.kg^{-1}.K^{-1})
500 – 4 000	520
4 000 – 10 000	1.48981404E-16*T^5 - 2.97394294E-12*T^4 + 2.20500675E-08*T^3 - 7.02196412E-05*T^2 + 7.09744733E-02*T + 5.57924223E+02
10 000 – 13 000	-2.82185649E-11*T^4 + 1.27503916E-06*T^3 - 2.11742791E-02*T^2 + 1.54726765E+02*T - 4.21243826E+05
13 000 – 16 000	-1.2942701617E-17*T^6 + 1.1393700131E-12*T^5 - 4.1629375758E-08*T^4 + 8.0805889164E-04*T^3 - 8.7896389685E+00*T^2 + 5.0811929085E+04*T - 1.2199597792E+08
16 000 – 24 000	-2.65071301E-19*T^6 + 3.07960613E-14*T^5 - 1.48602562E-09*T^4 + 3.81146727E-05*T^3 - 5.47526461E-01*T^2 + 4.16936060E+03*T - 1.31100323E+07

Table B-4: Argon dynamic viscosity

Temperature range (K)	Viscosity (kg.m^{-1}.s^{-1})
500 – 3 000	3.4634351685E-25*T^6 - 2.4829097967E-21*T^5 + 2.7667339941E-18*T^4 + 1.9733594722E-14*T^3 - 6.9283954494E-11*T^2 + 1.1549266344E-07*T - 9.0390551996E-06
3 000 – 11 000	-1.3704827466E-27*T^6 + 4.8383943932E-23*T^5 - 7.0329560418E-19*T^4 + 5.4687394855E-15*T^3 - 2.5160972114E-11*T^2 + 9.1033715399E-08*T - 2.8296360319E-05
11 000 – 17 000	3.2449286046E-26*T^6 - 2.8114978843E-21*T^5 + 1.0059233236E-16*T^4 - 1.9002775883E-12*T^3 + 1.9970822504E-08*T^2 - 1.1065856486E-04*T + 2.5285559050E-01
17 000 – 24 000	-2.3108525934E-28*T^6 + 3.1401015649E-23*T^5 - 1.7077668650E-18*T^4 + 4.7629718197E-14*T^3 - 7.1738698636E-10*T^2 + 5.5053420537E-06*T - 1.6585541035E-02

Table B-5: Argon thermal conductivity

Temperature range (K)	Thermal conductivity (W.m^{-1}.K^{-1})
500 – 10 000	3.899492E-16*T^4 - 6.037160E-12*T^3 + 3.027093E-08*T^2 - 2.809659E-05*T + 4.439997E-02
10 000 – 15 000	2.80387597E-22*T^6 - 2.02062506E-17*T^5 + 6.01557305E-13*T^4 - 9.48647022E-09*T^3 + 8.37453071E-05*T^2 - 3.92824453E-01*T + 7.65492923E+02
15 000 – 20 000	-6.16984942E-23*T^6 + 7.24028056E-18*T^5 - 3.52197100E-13*T^4 + 9.08844319E-09*T^3 - 1.31155596E-04*T^2 + 1.00305167E+00*T - 3.17209792E+03
20 000 – 24 000	2.8428E-04*T - 2.7925E+00

Table B-6: Argon electrical conductivity

Temperature range (K)	Electrical conductivity (A.V^{-1}.m^{-1})
500 – 10 000	-6.49904188E-20*T^6 + 1.64679436E-15*T^5 - 1.43165855E-11*T^4 + 5.57978403E-08*T^3 - 1.01176462E-04*T^2 + 7.81145723E-02*T - 1.95125009E+01
10 000 – 24 000	1.4191365546E-21*T^6 - 1.6875200017E-16*T^5 + 7.8540321173E-12*T^4 - 1.8638884134E-07*T^3 + 2.3692310870E-03*T^2 - 1.4214582405E+01*T + 3.1504952850E+04

Table B-7: Argon net emission coefficient at 2 mm (minimum estimation)

Temperature range (K)	Net emission coefficient (minimum) (W.m^{-3}.sr^{-1})
10 000 – 14 000	1.21885522E-03*T^3 - 1.82510823E+01*T^2 + 2.41822992E+03*T + 5.90186869E+08
14 000 – 19 000	1.09557110E-02*T^3 - 5.04079254E+02*T^2 + 7.89778555E+06*T - 4.14387879E+10
19 000 – 20 500	1.33333333E-01*T^3 - 7.80000000E+03*T^2 + 1.52266667E+08*T - 9.90000000E+11
20 500 – 22 000	2.66666667E-01*T^3 - 1.74000000E+04*T^2 + 3.78633333E+08*T - 2.74480000E+12

Table B-8: Argon net emission coefficient at 2 mm (maximum estimation)

Temperature range (K)	Net emission coefficient (maximum) (W.m^{-3}.sr^{-1})
10 000 – 14 000	4.73659674E-06*T^4 - 2.08070448E-01*T^3 + 3.44867133E+03*T^2 - 2.55011292E+07*T + 7.08582199E+10
14 000 – 17 000	8.0000000016E-08*T^5 - 6.0848484861E-03*T^4 + 1.8489393943E+02*T^3 - 2.8056060612E+06*T^2 + 2.1260953338E+10*T - 6.4373107807E+13
17 000 – 20 000	-5.3333333352E-08*T^5 + 4.9939393957E-03*T^4 - 1.8681818188E+02*T^3 + 3.4901333345E+06*T^2 - 3.2562301223E+10*T + 1.2137800718E+14
20 000 – 22 000	1.00000000E-03*T^4 - 8.38000000E+01*T^3 + 2.63235000E+06*T^2 - 3.67343500E+10*T + 1.92150500E+14

B.2 Ar/5%H2 plasma

The same properties as those reported for pure argon are summarized for the case of a plasma mixture of argon with 5% of hydrogen from Table B-9 to Table B-17. The sources used to collect the data were the same as for pure argon.

Table B-9: Ar/5%H$_2$ density

Temperature range (K)	Density (kg.m^{-3})
500 – 2 500	464.393*T-1.00026
2 500 – 10 000	-1.75333229E-20*T^5 + 6.54682032E-16*T^4 - 9.81339974E-12*T^3 + 7.49284839E-08*T^2 - 3.03477459E-04*T + 6.05060320E-01
10 000 – 24 000	4.60789305E-22*T^5 - 4.13955100E-17*T^4 + 1.44260745E-12*T^3 - 2.40844435E-08*T^2 + 1.87620263E-04*T - 4.99373467E-01

Table B-10: Ar/5%H$_2$ enthalpy

Temperature range (K)	Enthalpy (J.kg^{-1})
500 – 3 000	8.56841430E-12*T^5 - 5.11158804E-08*T^4 + 1.17606877E-04*T^3 - 1.26554523E-01*T^2 + 6.23297742E+02*T - 1.79053476E+05
3 000 – 12 000	7.30491065E-13*T^5 - 2.33969332E-08*T^4 + 3.08611247E-04*T^3 - 2.07695132E+00*T^2 + 7.64091121E+03*T - 9.19915030E+06
12 000 – 16 000	1.40901638E-11*T^5 - 1.03478537E-06*T^4 + 2.99424058E-02*T^3 - 4.26597091E+02*T^2 + 2.99993813E+06*T - 8.34527181E+09
16 000 – 24 000	-4.24851780E-13*T^5 + 3.95362491E-08*T^4 - 1.31528349E-03*T^3 + 1.83149861E+01*T^2 - 7.65682032E+04*T - 1.73791379E+08

Table B-11: Ar/5%H$_2$ specific heat

Temperature range (K)	Specific heat (J.kg^{-1}.K^{-1})
500 – 1 500	1.39627040E-06*T^2 + 1.81836830E-03*T + 5.57953916E+02
1 500 – 2 500	1.52997280E-07*T^3 - 7.72549534E-04*T^2 + 1.31007953E+00*T - 1.79948485E+02
2 500 – 4 400	-5.6249160849E-16*T^6 + 1.1579152406E-11*T^5 - 9.7998719410E-08*T^4 + 4.3627651642E-04*T^3 - 1.0776023584E+00*T^2 + 1.4012382090E+03*T - 7.4961922189E+05
4 400 – 11 500	-2.49770289E-16*T^5 + 1.25997491E-11*T^4 - 2.16705368E-07*T^3 + 1.73060476E-03*T^2 - 6.62034136E+00*T + 1.04215221E+04
11 500 – 16 500	1.72044997E-14*T^5 - 1.15136839E-09*T^4 + 3.04951627E-05*T^3 - 3.99957595E-01*T^2 + 2.60199771E+03*T - 6.72714069E+06
16 500 – 24 000	-3.50469062E-12*T^4 + 2.68230731E-07*T^3 - 7.22205278E-03*T^2 + 7.97105675E+01*T - 2.87559870E+05

Table B-12: Ar/5%H₂ dynamic viscosity

Temperature range (K)	Viscosity (kg.m^{-1}.s^{-1})
500 – 3 000	1.12247733E-21*T^5 - 1.19850402E-17*T^4 + 4.97090771E-14*T^3 - 1.00632233E-10*T^2 + 1.31095739E-07*T - 1.23643503E-05
3 000 – 10 500	-3.58062855E-20*T^4 + 9.36382336E-16*T^3 - 9.59572249E-12*T^2 + 6.68836437E-08*T - 1.77782497E-05
10 500 – 14 000	9.56261993E-19*T^4 - 4.48917589E-14*T^3 + 7.74367126E-10*T^2 - 5.83666530E-06*T + 1.65298614E-02
14 000 – 24 000	3.8219559355E-30*T^6 - 4.7575261706E-25*T^5 + 6.8507131061E-20*T^4 - 4.4866182021E-15*T^3 + 1.3298820442E-10*T^2 - 1.8198631697E-06*T + 9.4646470520E-03

Table B-13: Ar/5%H₂ thermal conductivity

Temperature range (K)	Thermal conductivity (W.m^{-1}.K^{-1})
500 – 3 500	-3.18825730E-20*T^6 + 3.09704816E-16*T^5 - 1.14541082E-12*T^4 + 2.09196549E-09*T^3 - 2.00400850E-06*T^2 + 9.99900530E-04*T - 1.66599931E-01
3 500 – 15 000	1.77600475E-23*T^6 - 1.18120053E-18*T^5 + 3.03935072E-14*T^4 - 3.90358764E-10*T^3 + 2.68869313E-06*T^2 - 9.48869975E-03*T + 1.36764149E+01
15 000 – 24 000	-1.35703247E-16*T^4 + 7.66785536E-12*T^3 - 1.10235611E-07*T^2 - 2.35046541E-04*T + 1.22010104E+01

Table B-14: Ar/5%H₂ electrical conductivity

Temperature range (K)	Electrical conductivity (A.V^{-1}.m^{-1})
3 000 – 3 500	2.36772917E-11*T^3 - 2.19305357E-07*T^2 + 6.77709995E-04*T - 6.98635717E-01
3 500 – 4 200	5.00314268E-10*T^3 - 5.43716577E-06*T^2 + 1.97220438E-02*T - 2.38713882E+01
4 200 – 5 500	1.10799228E-08*T^3 - 1.47584734E-04*T^2 + 6.56657541E-01*T - 9.75467103E+02
5 500 – 6 500	8.43765152E-05*T^2 - 9.00237045E-01*T + 2.41508276E+03
6 500 – 24 000	1.5823139300E-21*T^6 - 1.9019549597E-16*T^5 + 8.9480923084E-12*T^4 - 2.1427259929E-07*T^3 + 2.7443612528E-03*T^2 - 1.6725552248E+01*T + 3.7884631845E+04

Table B-15: Ar/5%H₂ net emission coefficient at 2 mm (minimum estimation)

Temperature range (K)	Net emission coefficient (minimum) (W.m^{-3}.sr^{-1})
10 000 – 12 500	5.92361111E-06*T^4 - 2.57736883E-01*T^3 + 4.22200868E+03*T^2 - 3.08098255E+07*T + 8.44067473E+10
12 500 – 14 000	4.91954023E-02*T^3 - 1.80781609E+03*T^2 + 2.21821839E+07*T - 9.06908046E+10
14 000 – 22 000	-7.68189588E-04*T^3 + 6.28509630E+01*T^2 - 1.15895054E+06*T + 6.55414845E+09

Table B-16: Ar/5%H₂ net emission coefficient at 2 mm (maximum estimation)

Temperature range (K)	Net emission coefficient (maximum) (W.m^{-3}.sr^{-1})
10 000 – 13 500	-1.38484848E-05*T^4 + 6.54797980E-01*T^3 - 1.14873864E+04*T^2 + 8.88190927E+07*T - 2.55749869E+11
13 500 – 17 000	6.81818182E-06*T^4 - 4.57323232E-01*T^3 + 1.13142045E+04*T^2 - 1.21928148E+08*T + 4.83535579E+11
17 000 – 22 000	4.83294483E-02*T^3 - 2.72890443E+03*T^2 + 5.15003885E+07*T - 3.21058042E+11